Simulation of heat transfer and automatic optimization of multiple probes trajectories for pre-operative planning of percutaneous thermoablation interventions

Amir Jaberzadeh

UNIVERSITÉ DE STRASBOURG

THÈSE DE DOCTORAT présentée par :

Amir Jaberzadeh

soutenue le : **13 Février 2015**

pour obtenir le grade de : **Docteur de l'université de Strasbourg**

Mention : Informatique

Simulation de transfert de chaleur et l'optimisation automatique des probes trajectoires multiple de la planification pré-opératoire pour les interventions percutanées thermique

THÈSE dirigée par :
Mme. Essert Caroline HDR, Université de Strasbourg

RAPPORTEURS :
M. Warfield Simon Thorne Griscom Chair de Radiology,Ecole de médecine d'Harvard
M. Jannin Pierre Directeur de Recherche, Université de Rennes 1

AUTRES MEMBRES DU JURY :
M. Collet Pierre Professeur, Université de Strasbourg

École doctorale *N*□ 269 : mathématiques, sciences de l'information et de l'ingénieur.
UMR 7357 CNRS / Unistra : laboratoire des sciences de l'ingénieur, de l'informatique et de l'imagerie

Acknowledgements

I would like to express my special thanks to Dr. Caroline Essert for her support, encouragement and patience during my PhD pursuit. I would like to thank her for guiding my research and for allowing me to grow as a research scientist. Her advice and experience during my research as well as on my career have been priceless.

Besides my advisor, I would like to thank my jury members Dr. Simon Warfield and Dr. Pierre Jannin for their precious time reading my thesis. I should also appreciate other members of the jury Prof. Pierre Collet and Prof. Afshin Gangi for their time and constructive comments on my defense. This research work could not be performed without validation of patient data. Hence, I would like to thank Dr. Elena Kaye and all other people collaborating with this research in Memorial Sloan Kettering Cancer Center for the data collection and other medical consultations.

I would like to extend my appreciation to my friends in Computer Graphics and Geometry laboratory (IGG) who motivated me during tough times. Finally, I would like to thank my family who has always been supporting me throughout my life with their faith and love.

Abstract

Context

Today, several minimally invasive techniques allow surgeons to perform tumor ablation procedures without opening the patient. Cryosurgery (also called cryoablation or cryotherapy) is one of these techniques. It has been introduced to treat prostate cancers in the early 1960s and works by decompressing very rapidly a gas (usually argon) through a needle-like probe. As the argon flows through the needle, a ball of ice crystals forms around the tip of the probe, thus immediately leading to cellular death of the surrounding tissues. Depending on the tumor location and size, multiple cryoprobes with different types can be employed.

For the surgeons, estimating pre-operatively the final results and planning the surgery in advance in a complicated anatomical environment is very challenging. Over- or under-ablation may result in complications during the treatment. Therefore, an ablation planning system plays an important role in tumor ablation procedures, as it provides a dry run to guide the surgeons. In most planning applications, the ablation zones are typically described as simplified non-realistic ellipsoids around the cryoprobes tips and due to the presence of cooling blood vessels in the vicinity of the needles the necrosis volume size may be over-estimated and the tumor incompletely ablated. To overcome these issues, numerical simulations based on bioheat equation are proposed to allow for an accurate estimation of the ablation zone to incorporate heat-sink effects of large blood vessels.

Another big challenge is the feasibility of multiple needles placement satisfying some constraints like avoiding anatomical and vital organs, or the translation of some technical surgery rules like minimal trajectory length, tangency to organs while penetrating their surface and marginal tumor ablation volume. Given the lack of a planning tool addressing all these conditions and the crucial need for such a planner, in this thesis we focused on software-assisted cryosurgery planning aiming at supporting the physician by utilizing a more realistic prediction of the ablation zones, and proposing a needle placement setup with a risk close to minimum for the patient and an optimal coverage of the tumor by the iceball in an acceptable time for a use in the operation room.

Simulation

Among different proposed methods for the interpretation of thermal propagation in living tissues, one of the most widely used methods called Modified Penne's bio-heat transfer equation was selected. In order to keep the genericity of our planning tool for combined cryosurgery and hyperthermia, the effective heat capacity method was used to numerically solve the phase change problem with multiple moving boundaries.

Based on this solution which automatically satisfies phase change conditions, a unified equation,

which can be applied to frozen, partially frozen and unfrozen tissue regions, was created. In this equation, the tissues were treated for freezing or thawing with multiple needles over a temperature range, and the influence of blood perfusion and metabolic heat generation has been taken into account for the unfrozen and undamaged region. For the discretization purposes we have used an explicit backward differentiation method.

We used several visualization methods including 2D slices, 3D meshes and volume rendering to overlay the ablation zone onto the anatomical images. In order to estimate the accuracy of our approximation method, the computed ablation zone was overlaid on its corresponding segmented region of intra-operative images for cases of one and two needles. To show the heat sink effect of large vessels on the deformation of iceballs we compared the ablation zone with simplified ellipsoid iceballs proposed by the manufacturers in complex vascular situations, extracted from experimental data sets. Hausdorff distance, Dice coefficient and Boolean volume overlap were used for comparison purposes.

Our contribution for this part includes considering an estimation of large vessels heat sink effect in computation of ablation zone which has not previously been taken into account in cryosurgery planning. An interactive framework was developed to manually change several needles positions and orientations and visualize their computed ablation zone for surgical assistance or training purposes. Finally, since it is one of the long-term goals of our planning tool, the simulation of heat propagation was designed to be solved for different surgical thermo-ablation routines.

Multiple trajectory planning

The multi-objective nature of tumor ablation planning problem can be can be classified under Non-deterministic Polynomial (NP) problems in terms of computation. A simplified problem of optimizing full tumor coverage was translated into a problem of minimal coverage by several ellipsoids or simulated bioheat isotherms of multiple needles.

A number of constraints were applied to this problem. These constraints could be represented as solution space avoiding vital structures or tangency to the liver capsule. They were satisfied in a preprocessing step creating an approximately safe insertion zone over the skin. Other constraints such as needles crossing avoidance and full tumor coverage could be computed at each iteration of optimization process. These constraints are highly non-linear and therefore were resolved by developing appropriate optimization methods and penalty functions.

Next, several objective functions were introduced in our planning tool in order to minimize the volume of damaged healthy tissue, and maximize the distance of multiple needle trajectories to vessels and vital organs. For scalarization of this multiple objective function, a weighted sum criterion was applied and each objective function was normalized beforehand to a value between 0 and 1.

Different optimization methods suitable for this type of problem were experimented, from deterministic to stochastic and derivative free to model based. Speed, accuracy and robustness of some of these methods were compared in a search domain with different complexities. Other characteristics of methods like sensitivity to initial parameters were also analyzed. For validation purposes a comparison was done with a synthetic ground truth, and the results were compared with the results

obtained using a Monte-Carlo sampling method. Moreover they were compared with intra-operative images of a patient for the case of two needles.

Our contribution in this part includes the development of an automatic planning tool for cryosurgery, optimizing multiple needles with full degree of freedom for needle placements while avoiding obstructive and vital organs, a generic tool which accepts new surgical and anatomical constraints based on the organ being operated, integrating simulation and planning steps for tackling a real cryosurgery planning problem and two phase optimization approach to combine simplified ellipsoids and bioheat simulation for obtaining fast planning results.

Conclusion and future works

In this PhD thesis, a planning tool for multiple needle cryosurgery was developed integrating the bioheat simulations for defect region computation in the optimization process. Non-linear constraints were resolved using a one-time preprocessing step and introducing several penalty functions. A two-phase optimization process was used which shows more accurate result in acceptable computational time applicable in the operation room. The effect of vessels on deformation of iceballs demonstrated the important role of vessels in iceball formation and tumor recurrence if underestimated.

Using parallel processing algorithms could be proposed in the future for faster and finer computation of bioheat equation while keeping numerical solution more stable to the input parameters. Introducing deformable needles to our planning tool would also increase the range of applicability and produce more realistic results.

Keywords

Automatic surgical planning, bio-heat simulation, derivative free optimization, cryosurgery

Résumé

Contexte

Différentes techniques de chirurgie mini-invasive permettent aujourd'hui d'effectuer les procédures d'ablation de tumeurs. La cryochirurgie (également appelée cryoablation ou cryothérapie) est une de ces techniques. Elle a été mise en place au début des années 1960 pour traiter les cancers de la prostate. Elle fonctionne grâce à une technique de décompression très rapide du gaz (généralement de l'argon) à l'extrémité d'une sonde en forme d'aiguille. Lorsque l'argon s'écoule à travers l'aiguille, une boule de cristaux de glace se forme autour du bout de la sonde, ce qui conduit immédiatement à la mort cellulaire des tissus environnants. Selon l'emplacement de la tumeur et la taille de la tumeur, plusieurs aiguilles, éventuellement de types différents, peuvent être utilisées simultanément afin de couvrir la totalité de la tumeur.

La planification préopératoire de ce type d'intervention est très difficile pour le chirurgien, qui doit se représenter mentalement la disposition finale des aiguilles par rapport à la position des structures anatomiques environnantes, ainsi que la forme finale du glaçon formé autour des pointes des aiguilles, afin de choisir une stratégie de placement dans un environnement anatomique complexe. Une sur-ablation ou une sous-ablation peuvent entraîner des complications au cours du traitement. De même, un mauvais placement peut également entraîner des complications, notamment des hémorragies. Ainsi, le système de planification d'ablation joue un rôle important dans les procédures d'ablation de la tumeur car il fournit une simulation virtuelle pour guider les chirurgiens.

Dans la plupart des applications de planification existantes les zones d'ablation sont typiquement décrites comme des ellipsoïdes simples non réalistes autour des aiguilles. Pourtant, en raison de la présence de vaisseaux sanguins dans le voisinage des aiguilles pouvant provoquer un effet de réchauffement, le volume de nécrose peut être déformé, sa taille peut être diminuée, et la tumeur peut n'être que partiellement soumise à une ablation. Pour remédier à ces problèmes, des simulations numériques basées sur l'équation de transfert de chaleur ont été utilisées pour permettre une estimation précise de la zone d'ablation intégrant les effets de dissipation de chaleur des gros vaisseaux sanguins.

Un autre grand défi est l'automatisation du choix de placement tridimensionnel de plusieurs aiguilles simultanément, qui adoptent les contraintes habituelles sur des aiguilles individuelles (par exemple des règles de sécurité comme l'évitement des organes vitaux et les éléments anatomiques, des règles techniques comme la longueur maximale d'aiguille limitant la longueur de la trajectoire, ou encore des règles relatives à la cautérisation), ainsi que des contraintes supplémentaires liées à l'interaction entre les différentes aiguilles (non intersection, interaction des effets).

Ainsi, aucun outil ne permettant à l'heure actuelle d'aborder tous ces points, et devant le besoin

crucial d'une telle planification, dans cette thèse nous nous sommes concentrés sur la planification préopératoire automatisée de la cryochirurgie, avec deux objectifs principaux : 1) assister le chirurgien grâce à une prédiction plus réaliste des zones d'ablation et 2) proposer automatiquement un placement d'aiguille avec un risque minimal pour le patient et une couverture optimale de la tumeur par la boule de glace, dans un délai acceptable pour une utilisation en salle d'opération.

Simulation

Afin de modéliser la propagation thermique dans les tissus vivants, l'une des méthodes les plus couramment utilisées, l'équation de transfert de chaleur de Pennes, a été choisie. Afin de garder la généricité de notre outil de planification pour la cryochirurgie combinée et l'hyperthermie, la méthode efficace de la capacité thermique est utilisée pour résoudre numériquement le problème de changement de phase avec des frontières mobiles multiples. Sur la base de cette solution qui satisfait automatiquement les conditions de changement de phase, une équation unifiée, qui peut être appliquée aux régions de tissus gelées, partiellement gelées et non-gelées est crée. Dans cette équation les tissus sont traités pour le gel ou le dégel avec plusieurs aiguilles sur une gamme de température, et les influences de la perfusion sanguine et de la production de chaleur métabolique ont été prises en compte pour la région non-gelée. Pour la discrétisation nous avons utilisé une méthode de différenciation arrière explicite.

Nous avons utilisé plusieurs méthodes de visualisation, y compris les tranches 2D, les mailles 3D et le rendu volumique pour superposer la zone d'ablation sur les images anatomiques. Afin de valider la méthode d'approximation, la zone d'ablation calculée a été superposée sur sa région segmentée correspondante sur des images post-opératoires, dans des cas d'ablation à une et deux aiguilles. Afin de montrer l'effet de dissipation de chaleur des vaisseaux sur la déformation des boules de glace, nous avons comparé la zone d'ablation avec les boules de glace ellipsoïdales simplifiées indiquées par les fabricants, dans les situations vasculaires complexes extraites de 10 ensembles de données réelles. Distance de Hausdorff, coefficient de Dice et chevauchement de volume booléen ont été utilisés pour la comparaison.

Notre contribution pour cette partie comprend l'étude de l'effet dissipateur de chaleur des gros vaisseaux dans le calcul de la zone d'ablation qui n'a encore jamais été pris en compte dans un contexte de planification de cryochirurgie dans la littérature. Un cadre interactif a été conçu pour modifier manuellement les positions et les orientations de plusieurs aiguilles et pour visualiser la zone d'ablation calculée, à des fins d'assistance ou de formation chirurgicale. Enfin, de façon à prendre en compte la simulation de différents types de thermo-ablation et de conserver l'aspect générique de l'outil de planification, nous avons utilisé des approches gérant aussi bien les ablations par hypo- (cryoablation) que par hyperthermie (radiofréquence).

Planification de trajectoire multiple

Le problème de planification automatique d'ablation de tumeur est un problème multi-objectif, qui consiste à trouver le meilleur compromis satisfaisant au mieux les multiples contraintes qui s'appliquent. C'est un problème compliqué, dans lequel la nature multi-objectif du problème est

difficile à résoudre, mais également chaque contrainte séparément peut être complexe. En particulier, le recouvrement de la totalité de la tumeur par un volume de glace minimal est mathématiquement proche de problèmes classiques de couverture minimale d'un objet avec plusieurs autres formes géométriques, ici des ellipsoïdes (version simplifiée) ou des surfaces isothermes simulées par l'équation de transfert de chaleur depuis les aiguilles. Ce problème de recouvrement peut être classé dans les problèmes polynomiaux non-déterministes en termes de calcul.

Un certain nombre de contraintes a été appliqué à ce problème. Ces contraintes représentent : 1) la création d'une zone délimitant les points d'insertion possible, permettant par exemple d'éviter différents organes tels que les os et la moelle épinière, les gros vaisseaux, ou permettant de ne pas entrer de façon trop tangente par rapport à la surface du foie : ces contraintes sont satisfaites dans une étape de pré-traitement créant une "zone d'insertion", projection sur la peau des trajectoires faisables; 2) la minimisation de valeurs numériques représentant par exemple des règles de non intersection des aiguilles, ou la couverture complète de la tumeur : ces valeurs doivent être calculées à chaque itération d'un processus d'optimisation. Ces contraintes sont fortement non-linéaires, et ont donc été résolues par le développement de fonctions de pénalité appropriées.

Plusieurs fonctions objectif ont été introduites dans notre outil de planification afin de minimiser le volume de nécrose des tissus sains et de maximiser la distance des trajectoires multiples des aiguilles aux vaisseaux et aux organes vitaux. Pour transformer cette fonction multi-objectif en une unique fonction mono-objectif à minimiser, une somme pondérée est utilisée et chaque fonction objectif est normalisée à l'avance.

Différentes méthodes d'optimisation adaptées à ce type de problème ont été utilisées : déterministes ou stochastiques, basées gradient ou sans dérivée, heuristiques ou basées modèle. La vitesse, la précision et la robustesse de certains de ces procédés ont été comparées dans un domaine de recherche avec les différentes complexités. D'autres caractéristiques de ces méthodes, telles que la sensibilité et les paramètres d'entrée, ont également été analysées. À des fins de validation, des expérimentations ont été menées en définissant une configuration a priori de la zone d'ablation et les résultats ont été comparés avec les résultats obtenus en utilisant une méthode de recherche exhaustive. En outre, ils sont comparés aux images post-opératoires des patients pour le cas d'un et de deux aiguilles.

Notre contribution dans cette partie comprend l'élaboration d'un outil de planification automatique pour la cryochirurgie, pour l'optimisation 3D de plusieurs aiguilles à tous degrés de liberté tout en évitant les organes obstructifs et vitaux, un outil générique qui accepte des nouvelles contraintes chirurgicales et anatomiques basées sur l'organe opéré, en tenant compte de l'intégration des mesures de simulation et de planification, et un approche d'optimisation en deux phases pour combiner ellipsoïdes simplifiés et la simulation de transfert de chaleur afin d'obtenir les résultats rapides.

Conclusion et perspectives

Dans cette thèse, un outil de planification pour la cryochirurgie avec aiguilles multiples a été élaboré en tenant compte de l'intégration de simulations de transfert de chaleur dans le processus d'optimisation. Les contraintes non-linéaires ont été résolues en utilisant une étape unique de pré-

traitement et en introduisant plusieurs fonctions de pénalité. Un processus d'optimisation en deux phases a été utilisé, qui permet d'obtenir un résultat plus précis en un temps de calcul acceptable et applicable en salle d'opération. L'étude de l'influence des vaisseaux a démontré le rôle important des vaisseaux dans formation de la boule de glace, souvent surestimée par les méthodes habituelles, et donc dans les risques de récidive de la tumeur.

Dans de futur travaux, l'utilisation d'algorithmes de traitement parallèle pourra être proposée pour le calcul rapide et plus fin de l'équation de transfert de chaleur, en gardant la solution numérique plus stable pour les paramètres d'entrée. L'introduction de modèles d'aiguilles déformables dans notre outil de planification pourrait également augmenter l'éventail d'applications et produire des résultats plus réalistes.

Mots-clés

Planification chirurgicale automatique, simulation de chaleur de Pennes, optimisation sans dérivée, cryochirurgie

Contents

List of Figures

List of Tables

Chapter 1. Introduction

1.1 Overview

Cancer is one of the leading causes of death in most of the countries in the world. Among the predominant cancer types, liver cancer ranks fourth due to a high prevalence of hepatitis B. About 500.000 new cases are diagnosed every year in the world. In order to treat liver cancer several kinds of surgical interventions have emerged while treatments based on minimally invasive interventions showed to have long term benefits and fast recovery time. This chapter is organized as follows: for readers with no medical background Section 1.2 introduces the used terminology, the liver's anatomy and liver treatment options. Section 1.3 covers some minimally invasive interventions related to this thesis. Section 1.4 presents the objectives, challenges and contributions described in this manuscript and a short outline of this thesis will complete this chapter.

1.2 Medical background

The liver plays a major role in metabolism. It is responsible for detoxification, glycogen storage and plasma protein synthesis. It also produces bile, which is important for digestive functions.

The liver has two lobes and is supplied by two major blood vessels: the hepatic artery and the portal vein. The blood leaves the liver by using the hepatic vein. The blood from the artery carries oxygen while the portal vein carries nutrients from the intestine (see Figure 1-1).

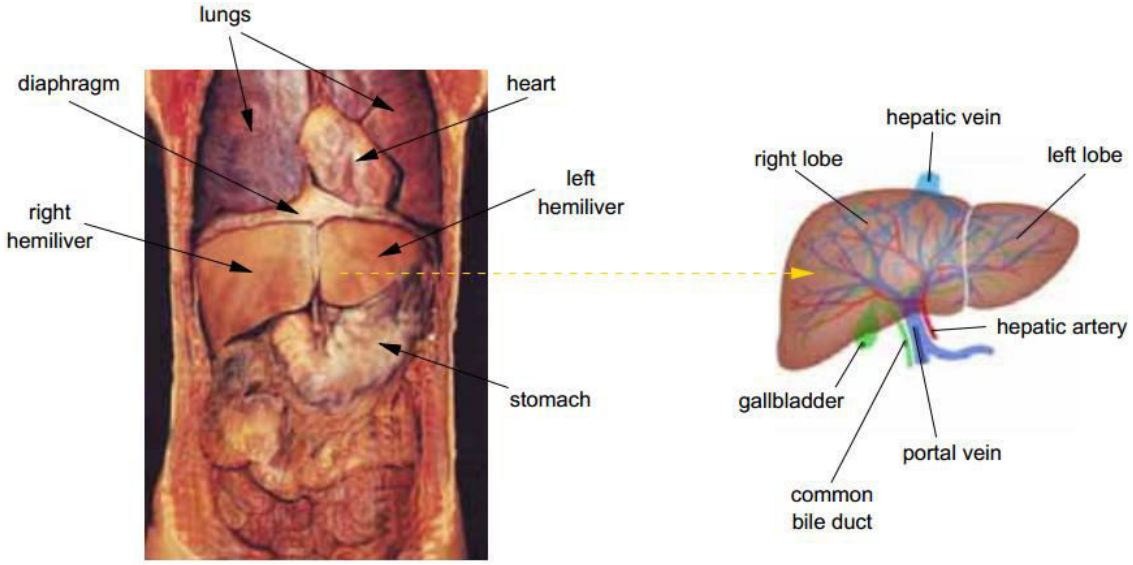

Figure 1-1 The left image shows the liver located in the human's body and the right image shows the blood flow in the liver [1]

The liver is an essential organ with a complex vascular anatomy. Probably because of its filtering functions, this organ is one of the most frequently affected by metastases.

In order to diagnose a liver tumor, imaging technologies for observing the patient's body structure are required like CT and MRI (see Figure 1-2). Contrast agents are used to highlight structures such as blood vessels that otherwise would be difficult to delineate from their surroundings. A violet fluid such as iodineis is often injected intravenously for highlighting the portal vein.

In order to treat such tumors, surgical interventions like surgical resection (tumor removal) and liver transplantation were used traditionally depending on the size and position of the tumor.

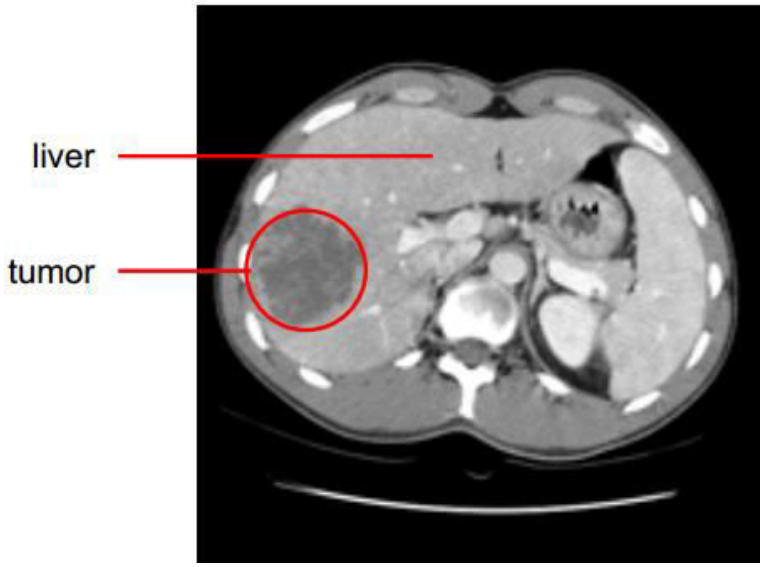

Figure 1-2: Axial view of the liver CT slice containing a tumor as a darker region indicated by red circle

Recently, the emergence of minimally invasive surgeries has enabled treatments aiming at destroying the tumor without opening the patient's tissue, with equally long-term benefits. Several minimally invasive techniques exist, such as microwaves, laser, High-Intensity Focused Ultrasound (HIFU), or percutaneous hyperthermia. In this manuscript we will focus more particularly on the latter, which is now the most frequently chosen by surgeons. It consists in destroying the tumor by extreme heat or cold, using methods such as radiofrequency ablation or cryotherapy.

1.3 Minimally invasive surgery

Minimally invasive surgery has gained an increasing interest in the past decades. By keeping benefits similar to conventional surgery, minimally invasive surgery decreases patient's discomfort and the recovery time due to the small size of incisions. Using pre-operative imaging, computer-assisted ablation planning strategies are elaborated to optimize operation plans. Toolkits currently used by surgeons for visualization of anatomical structures and navigation of real-time images include IGSTK [2] and 3D Slicer [3]. These softwares enable surgeons to visualize the three-dimensional structure of the tumor as well as to envision ablations and to assess the treatment by developing optimal treatment plans intra-operatively. Below we will briefly introduce three minimally invasive techniques used in our Trajectory Planning project. We will mainly focus on cryosurgery of liver tumors as it is the main topic of this thesis.

1.3.1 Cryosurgery

History of cryosurgery (also called cryoablation or cryotherapy) as a clinical method to treat prostate cancers dates back to the early 1960s. Cryoprobes are small needle-like devices with a diameter of around 1.5mm (see Figure 1-3). A decompression chamber is located at their tip and they are inserted into the tumor during laparoscopic surgery or percutaneously under image guidance. A gas is rapidly decompressed resulting in tissue injury based on the Thompson-Joule principle. Two basic mechanisms are believed to cause cryoablation: firstly the direct injury to the cells caused by the freeze-thaw cycle, and secondly the damage caused by freezing the blood vessels of the tumor that can cause an indirect injury to the cells [4].

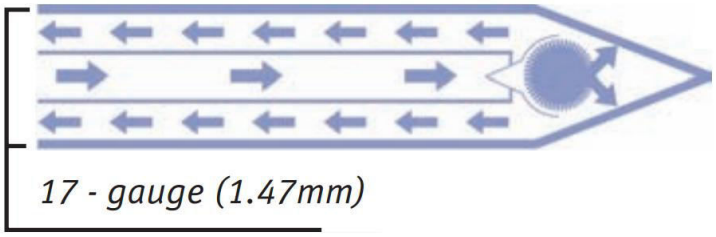

Figure 1-3: Needle tip inner structure (GalilMedical Co[1].)

As tissue freezes, ice crystals will form in the extracellular spaces. This creates a hyperosmotic environment by water withdrawal from the tissue, which causes the cells to loose water by diffusion. If the cooling process is sufficiently rapid, the cell will not lose water fast enough to maintain osmotic equilibrium between the cytoplasm and the extracellular space, and the cytoplasm will become extremely cooled. A supercooled cytoplasm leads to a lethal injury to the cell [5-8]

Clinical parameters that contribute to the result of cryotherapy include the cooling rate, tissue temperature, duration of freeze-thaw cycles, and the time between the cycles. This technique has been applied successfully to treat several kinds of tumors, including breast cancer, primary or metastatic liver neoplasms, renal, lung, pancreas, and prostate cancer.

In percutaneous cryoablation, the cancerous tissue is frozen using one or multiple needles. During this procedure, tissue temperature drops to -40°C around needle tip, which is lethal for the cells inside the iceball volume. The final goal of cryotherapy is the necrosis of cancerous cells while preserving surrounding healthy tissue and avoiding damages to vital anatomical structures. For this purpose, an accurate surgical planning needs to be done by surgeons before the operation.

Since only a limited set of active lengths and diameters are available for the manufactured cryoprobes (see Figure 1-4), and a fixed freezing protocol is usually used, other cryosurgical parameters that affect the shape of the iceball such as the number of cryoprobes and the cryoprobe placement are good candidates for optimization and planning. Usual planning is done on slice-based reformations of the 3D volume. In these conditions, determining optimal and safe penetration angles of the instruments as well as imagining the size and shape of the resulting iceball are very difficult, especially when several cryoprobes are necessary and produce a combined effect. This is typi-

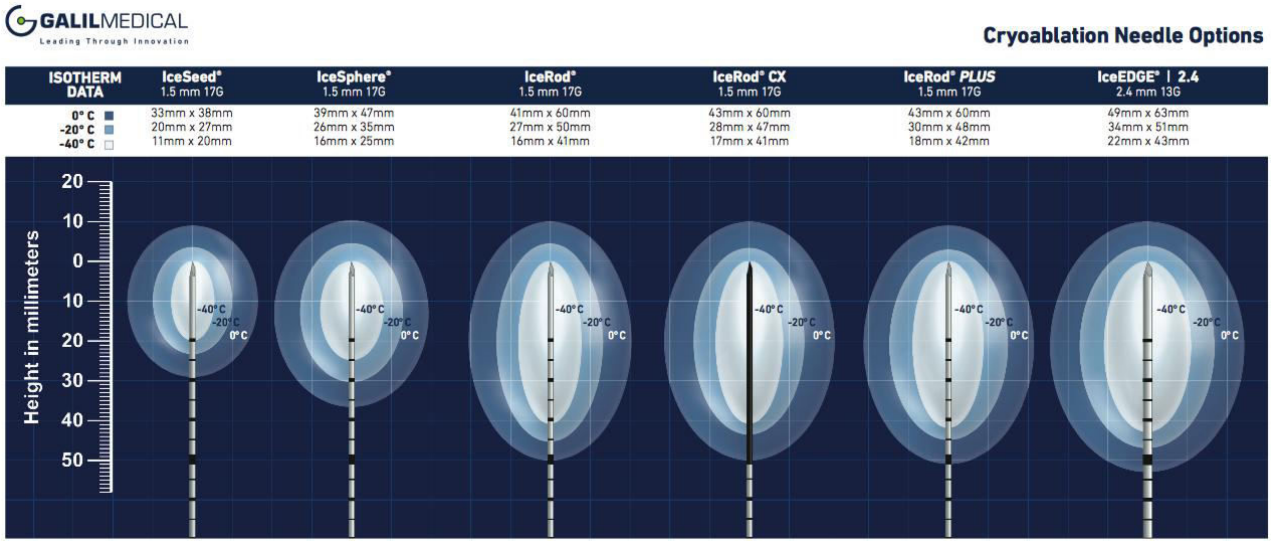

Figure 1-4: Different types of needles with their respective iceball shape (GalilMedical Co.)

cally done in a trial-and-error task to find the best configuration.

Finding an optimal and safe trajectory consists in: 1) solving mentally many surgical rules relative to the placement of one or several cryoprobes, these rules being sometimes contradictory, and 2) estimate mentally the shape and size of the produced iceball.

Thanks to the abundant literature about cryosurgery planning and intervention procedure, we can establish a summary of the main rules used by the surgeons when selecting an optimal path. A complete set of the chosen rules in this thesis is listed below in which some of them are similar to other related works in the field like the work of Sietel et al. [9]

1. **Placement in the target**. The tip of the needle must be located in the tumor.
2. **Position of the insertion point**. The patient can not be on the side, and rarely on the stomach due to anesthesia equipment. We provide our solver with an initial insertion zone corresponding to the nearest point on the side skin.
3. **Maximal path length**. This rule concerns the maximal length of the path, which obviously has to be shorter than the size of the cryoprobe (see Figure 1-6 (b)) .
4. **Risky structures avoidance**. It is necessary to find a needle placement that avoids crossing vital, risky, or impassable structures. For liver cryosurgery, the identified “obstacle” structures include the ribs, spine, vessels (see Figure 1-5), and any other organ likely to obstruct the path depending

on the location of the tumor. Images acquired with contrast agent or angiography are required to identify vessels.

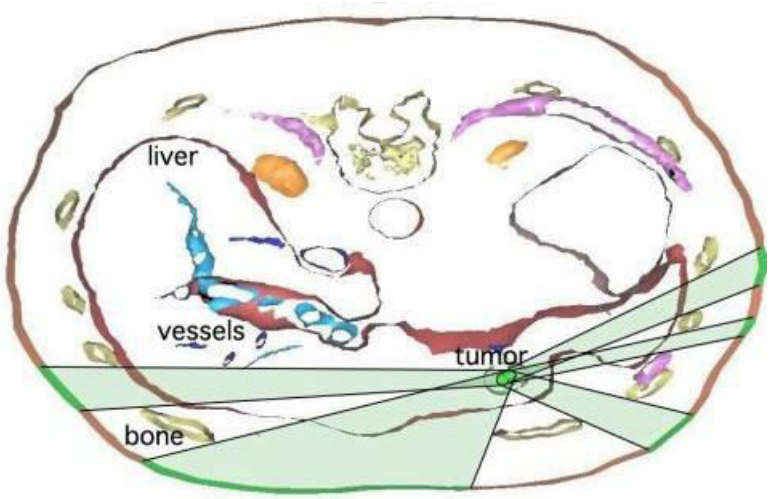

Figure 1-5 Avoiding risky regions is shown for cryosurgery planning. Ribs, vessels and spine are avoided taken from [10]

5. **Needle crossing**. In practice it is not recommended to have very close trajectories when multiple needles are used, so a minimum distance between the needles is fixed.
6. **Tangency to the liver surface**. Inserting needles with angles less than 20 degrees to the surface of the liver will cause slippery conflicts in penetration phase. Therefore, such insertion angles are avoided (see Figure 1-6 (a)).
7. **Distance to risky structures**. Even if we already specified a rule avoiding a needle to meet any risky structure, trajectories passing as far as possible from those structures are considered safer.
8. **Tumor coverage**. This crucial rule states that the tumor must be fully covered by the iceball to avoid tumor reccurrence.
9. **Cauterization**. Due to a possible displacement of cancerous cells during needle removal, a portion of healthy tissue along the needle path should be necrosed for security reasons during removal. This must be anticipated by planning that a minimal fixed amount of healthy tissue lies between the tumor and the border of the liver.

Besides the optimization of this needle placement rules, another important challenge of the pre-operative surgical planning is to define the real shape of iceballs for one needle or synergistic effect of multiple needles [11].

As shown in Figure 1-4, cryoprobe manufacturers provide several types of needles for different applications. In this figure, theoretical necrosis volumes are shown for the case of homogenous tissues, in the usual conditions of thermal protocol: two cycles of 10 minute freezing with 5 minute thawing in between. However, in practice tissues are more complex and highly inhomogeneous, and the use of these predefined shapes is inaccurate. In particular, the presence of large vessels in the vicinity of the iceballs can influence the shape of the iceball due to the heat-sink effect [12]. This effect is illustrated for RFA in Figure 1-7.

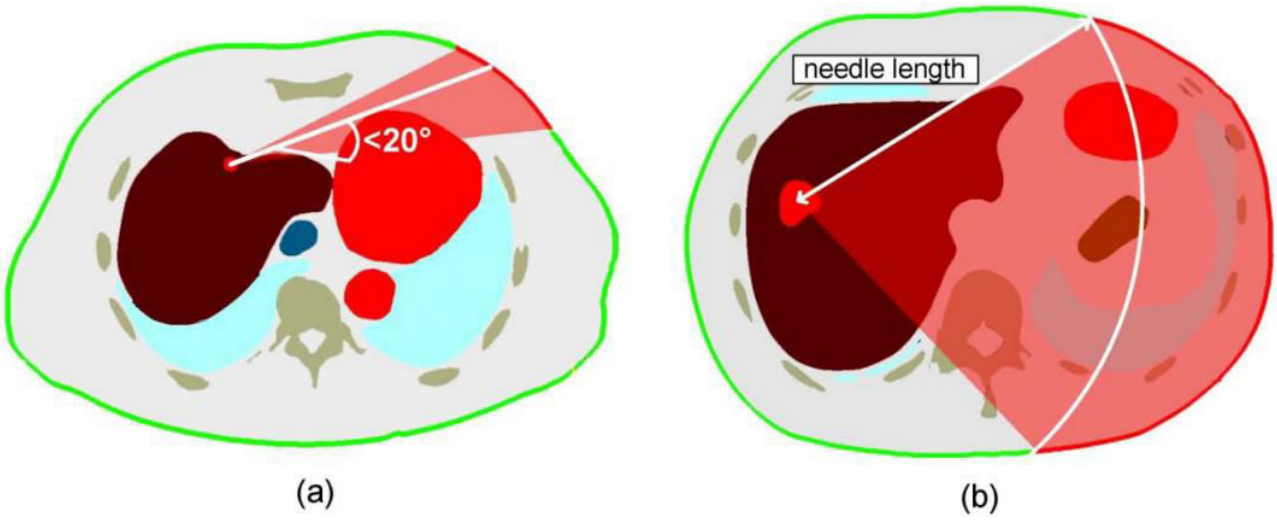

Figure 1-6 (a) Schematic illustration of the tangency constraint, which ensures that the angle in which the trajectory intersects the liver surface is bigger than 20° (b) The needle length constraint excludes all insertion trajectories from the insertion zone that are longer than the needle length [9]

A non-invasive, real-time monitoring of three-dimensional isotherm surface of freezing temperatures within the tissue remains a big issue for the surgeons because the temperature can't be measured or only measured at discrete points in the target region. Therefore, simulation of heat transfer is a useful tool to estimate the real shape of the iceball for a candidate probe placement. A number of models have been proposed to solve the bioheat propagation equation in two and three dimensions which will be covered in the next chapter.

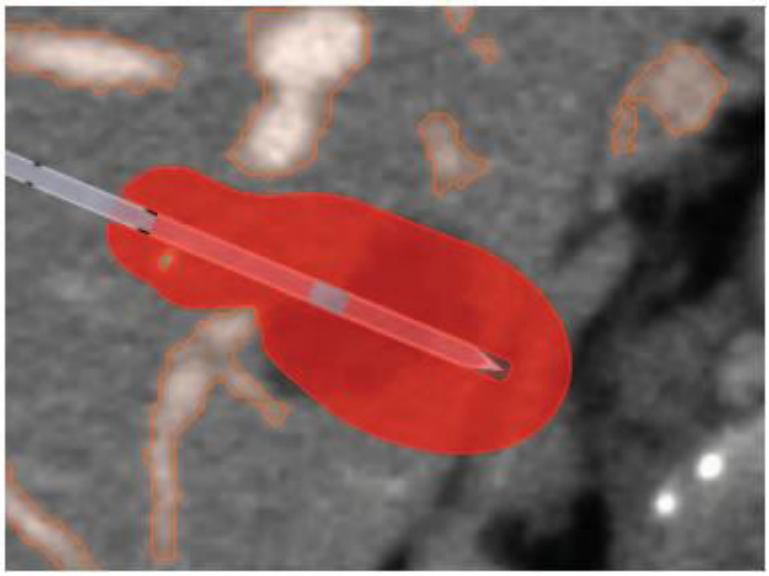

Figure 1-7 Approximated deformation of ablation region in RFA [13]

1.3.2 Radiofrequency ablation (RFA)

The principle of cancer treatment by RadioFrequency Ablation (RFA) is the destruction of cancerous tissue by insertion of radiofrequency applicators through the skin into the target tissue and use of an alternating electric field with high frequency oscillations (200 - 1.200 kHz) to induce lesion by thermal necrosis. Cytotxic effects of high temperature (50-100 °C) from irreversible protein denaturation can lead to thermal necrosis and coagulative necrosis when target volume is heated for

at least 4-6 minutes and results in cell destruction (see Figure 1-8).

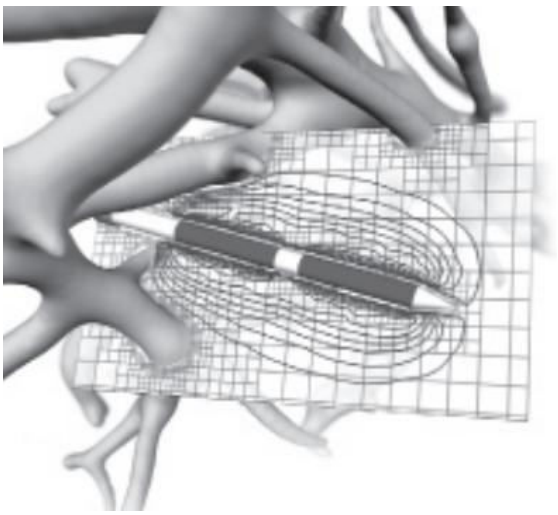

Figure 1-8 Bipolar RFA needle in the vicinity of blood vessels. Temperature isosurfaces are shown [14]

To handle uncertainties and microscopic clusters of cancer cells around the visible tumor tissue, the target volume is increased by a safety margin of at least 5 mm. The type of applicator, ablation time, as well as the induced energy, can alter the size of the coagulation region. Moreover, similarly to cryosurgery, the vascular structure around the applicator can contribute to cooling of the heat distribution with a heat-sink effect.

Similarly to cryosurgery, the pre-operative planning of liver RFA consists in acquiring pre-interventional images and uses them to plan an optimal and safe trajectory for the needle that enables full ablation of the tumor. Critical anatomical structures are also similar.

During the intervention, the RF applicator is monitored by intra-operative image guidance to support placement of the needle into the planned target area and to control the ablation progress (as well as parameters such as the induced energy). MR thermometry is sometimes applied to monitor the resulting heat distribution. After surgery, pre- and post-operative images are compared to assess the success of the treatment procedure.

During typical planning procedures in clinical routine, the surgeon uses just visualization of slices, or sometimes measurement tools on imaging workstations, to determine an optimal probe placement inside the target volume and mentally estimates the resulting ablation zone. In most planning prototypes, the ablation zones are typically expressed as ellipsoids around the RF applicator probes [15-17] which are specified for homogeneous tissue by the applicator manufacturers. However, this estimation of the ablation zone is not accurate if patient-specific planning of the intervention is desired. With the presence of cooling blood vessels in the vicinity of the RF applicator, the coagulation size may be decreased and the tumor incompletely ablated [18].

1.3.3 Deep brain stimulation

Pre-operative planning of surgical tool placement is also necessary and has also been studied in other types of interventions. As an example, Deep Brain Stimulation (DBS) consists in inserting stimulation electrodes in deep nuclei of the brain in a way to reduce motor symptoms of various

diseases, such as Parkinson's disease, dystonia or essential tumors (see Figure 1-9). Stimulation of the SubThalamic Nucleus (STN) or Globus Pallidus (Gpi) has proven to be successful treatment strategies when the treatment by other methods was unsuccessful [19]. The electrodes are inserted by minimally invasive methods using precise image guidance from a neuro-navigation platform. Prior to the intervention, the neurosurgeon examines the patient's images to determine precisely the location of a target of only a few millimeters where the DBS electrodes should be inserted. Then he searches for a safe linear trajectory from the skin to the target to avoid hemorrhages, loss of function and other injuries.

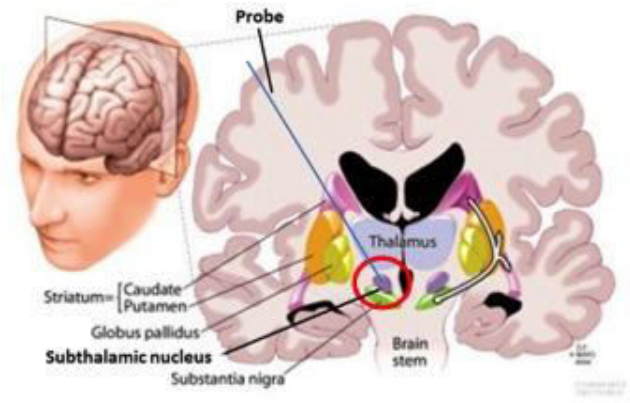

Figure 1-9 Cross section of probe placement for the DBS [19]

The trajectory planning usually starts with the inspection of anatomical MRI datasets using visualization tools proposed by commercial neuro-navigation platforms. The surgeon experimentally searches for a safe trajectory path to avoid critical structures like ventricles, sulci, large blood vessels, and critical motor and sensory cortex. However, only few trajectories can be thoroughly analyzed in a reasonable amount of time resulting in subjective and possibly sub-optimal planning. Recently, the design of automatic planning algorithms has grown rapidly to allow the speedy analysis of larger number of trajectories across multi-modal imaging datasets. In this kind of surgery as well, mimicking the decision-making process of neurosurgeons is an important challenge.

1.4 Challenges and research contributions

This thesis is part of the Trajectory Planning project developed at ICube laboratory, which has the goal of supporting radiologists and surgeons through computer-aided methods in several trajectory based minimally invasive surgeries. In the past few years, works have been done to automatize the planning process of single needle placement planning using theoretical models of the necrosis volume. This thesis focuses more particularly on the automatic planning of percutaneous cryoablation for liver tumors, which involves the placement of multiple interacting needles and the computation of precise iceball formation. In the following, the main contributions of this thesis towards computer-aided liver cryosurgery planning will be discussed.

Our contributions can be classified into three categories. The first category includes contributions in simulation and visualization of the iceball. The second category is dedicated to the planning system and optimization phase. The third category includes contributions benefiting from the combination of simulation and planning phases.

Contributions in simulation include:

- Considering convective large vessels heat-sink effect in computation of ablation zone which has not previously been taken into account in cryosurgery planning.
- An interactive framework developed to manually change multiple needles positions and orientations and visualize their computed ablation zone for surgical assistance or training purposes.
- A general case design of the simulation of heat propagation to be used for different surgical thermo-ablation routines.

Contributions in planning part include:

- Planning of multiple cryoprobes with full degree of freedom, allowing for any kind of cryoprobes rotation and translation
- Construction of a generic tool which accepts new surgical and anatomical constraints based on the organ being operated thanks to its heuristic search methods
- Introduction of new surgical rules for avoiding needle crossing and coverage of the tumor by the iceball besides other constraints for avoiding obstructive and vital organs
- Definition of a specific objective function and for constraint handling of our non-linear optimization problem
- Development of an automatic clinical software assistant for cryosurgery planning
- Proposing several distinct solutions to the surgeon in order to be selected by his own skills and concerns

Contributions in the third group include:

- Integration of simulated iceballs in the optimization phase
- Fast two-phase optimization approach combining ellipsoids rough optimization and fine optimization of the simulated ablations in order to obtain short planning time applicable in clinical routine

The flowchart of our workflow in Figure 1-10 shows the preprocessing steps required for the planning, followed by four different pipelines which can be used by the surgeon based on his personal requirements and the desired level of interactivity or automation. The preprocessing step consists of data preparation and computation of an insertion zone. Data preparation step is subdivided into segmentation, registration and smoothing of the pre- and intra- operative images. In the next preprocessing phase, feasible zones for passing trajectories are computed, and then the surgeon chooses whether to plan the surgery automatically or manually. In the manual planning labeled (1) our software assists the surgeon by showing a realistic ablation volume computed after the simulation phase, leaving the surgeon to choose only the placement of the cryoprobes.

If the automatic planning is selected, we offer different types of planning routines based on the required time or accuracy. One can perform the planning using simple multiple ellipsoids (2) which

is fast for realtime applications but less accurate in special conditions or choose to plan the surgery using the simulated ablation zones (3) which requires more time but it is more precise. Option (4) consists of our two-phase optimization method which can benefit from both speed and accuracy. Finally the results are visualized both in 3D and over the 2D slices and depending on the surgeons opinion it can be accepted or reconfigured.

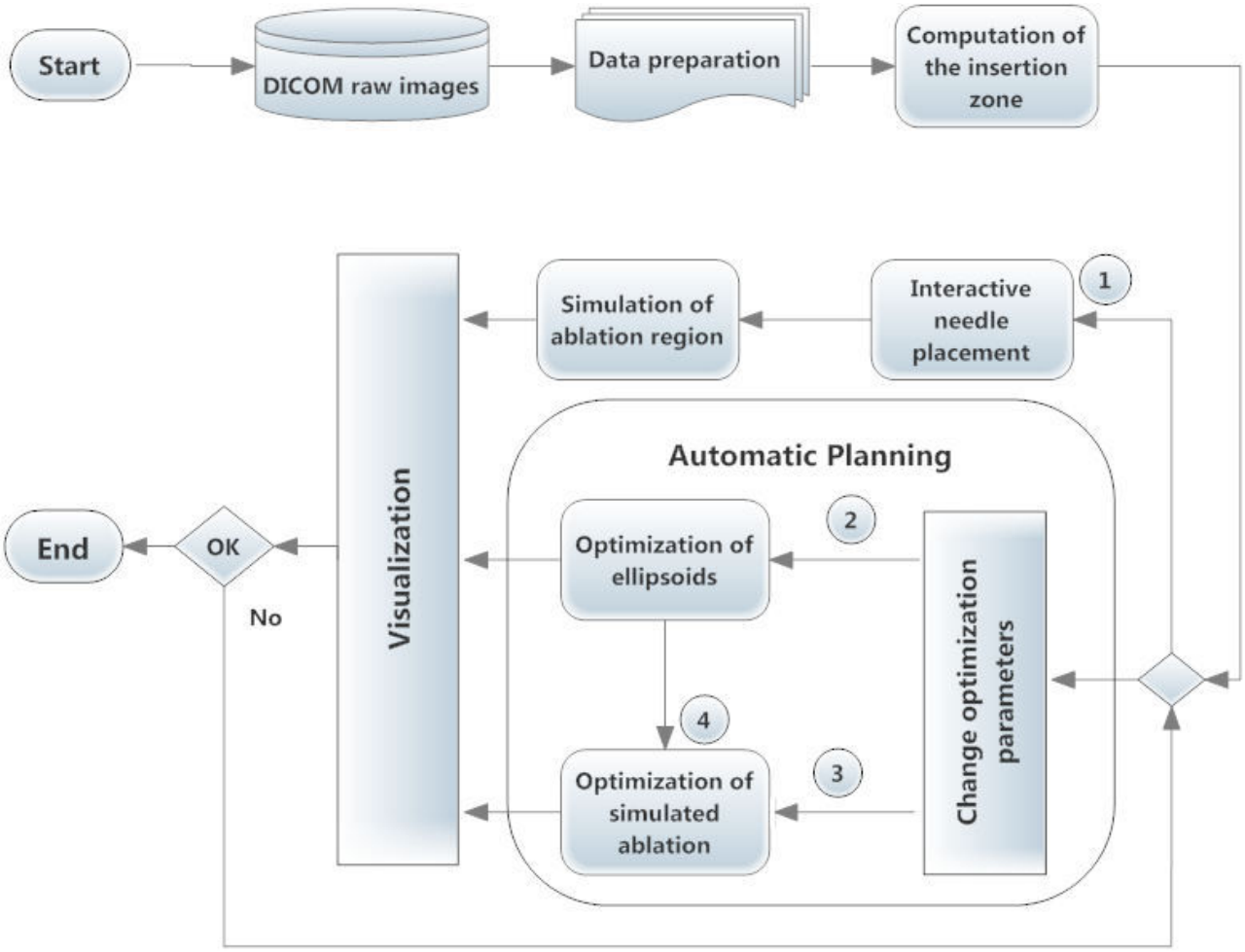

Figure 1-10: Flowchart of the proposed workflow. It supports four different surgical-assistive pipelines chosen by the surgeon based on his requirements

Several challenges existed in our work:

- Demonstrating several solutions found for multiple needles in a simple and informative way.
- Validation of the simulation and planning results with patient data was a hard and lengthy path due to administrative and practical issues in obtaining good images.

1.5 Thesis outline

This thesis is structured as follows:

Chapter 2 looks into the state of the art for cryosurgery simulation and planning of different related minimally invasive surgeries and reviews fundamental methods used for this purpose. In the

end, it states the problem pursued in this manuscript and differentiates our proposed pipeline with the work of others.

Chapter 3 details the sets of data used in this thesis for experiments and explains the required data preparation and pre-processing steps for our multi-modal images. These datasets will be used throughout the thesis for computations, planning and validation purposes.

Chapter 4 presents methods and parameters used in iceball computation then illustrates deformation of iceballs due to the heat-sink effect of large vessels. Furthermore, it quantitatively compares the ablation zone using simple ellipsoids, simulated iceballs and segmented intra-operative images.

Chapter 5 covers methodological issues like definition and implementation of geometric constraints in our planning tool. It also describes different algorithms and numerical methods implemented for the computation of proposed geometric constraints. It also includes a comparison of the accuracy and speed for some of the proposed methods.

Chapter 6 represents a specific formulation of our optimization problem then discusses several methods used to solve this problem. Multiple tests are considered to verify the results of these methods on the planning problem based on speed, accuracy and robustness. Then three methods are proposed for validation of the planned trajectories.

Chapter 7 concludes this thesis followed by a discussion on important topics and challenges and then proposes some ideas in continuation of this work.

Chapter 2. Related works

2.1 Overview

This chapter reports the state of the art regarding the topics closely related to this thesis. Section 2.2 discusses recent studies in the simulation of cryosurgery. In section 2.3, different planning systems reported before and during the period of preparation of this thesis are discussed and section 0 summarizes the motivation and ideas behind this thesis.

2.2 Cryosurgery simulation

Among the possible bio-heat transfer equations proposed for modeling of thermal data in living tissues, Penne's bio-heat transfer equation is the most commonly used model. Other models include the ones developed by Weinbaum and Jiji [20], and Nakayama and Kuwahara [21].

In computer simulation, the first prediction of ice ball formation around a single cryosurgical probe was published by Bischof, Smith et al. in 1997 [22]. They used a one-dimensional radial cylindrical model to predict the temperature profile and the interface location. In numerical mathematics, the problem of solving bioheat equation can be defined as predicting the time-evolving position of freezing or thawing fronts where phase change happens. This is commonly called the Stefan problem and requires solving the heat conduction equation for the temperature in a domain that consists of frozen and unfrozen parts which are separated by a moving interface (the freezing or thawing front). The precise location and form of the interface is critical and is determined by the fusion temperature at which phase change occurs and the Stefan condition is often imposed as the heat balance condition. Since the positions of the ice front depend on several unknown factors, such a problem is usually highly nonlinear and precise solution for such a complex problem is extremely difficult, and sometimes even impossible to compute if no substantial simplification can be introduced.

Several groups have proposed numerical models to solve the phase-change problems in biological tissues [23-27]. Two general families of numerical techniques for the computation of free surfaces were studied: tracking and capturing methods. In tracking methods, the position of the fronts is explicitly computed making them very difficult to implement due to reconfiguration of the mesh to fit the precise position of moving fronts. Capturing methods do not require the exact position of the free surface. These methods use enthalpy formulations. The effective heat capacity method is included in this family and it has been shown that the Stefan condition is automatically satisfied [28]. Although this approach has several advantages, it still requires the mesh to be refined close to the interface. To date, the majority of these numerical efforts have mainly focused on one- or two-dimensional heat transfer models. A few three-dimensional models have been developed by other

groups, [26] and [29]. However, these methods have not considered the effect of blood perfusion of tissues.

Rabin and Shitzer [25] considered the effect of blood perfusion, but their model still did not deal with the case of multiple cryoprobes. Phase-change problems of biological tissues subject to the combined cryosurgery and hyperthermia system are much more complex than when only a single cryoprobe is applied, because many more phase-change interfaces will be produced during the alternation of freezing and heating. Previously, Deng and Liu proposed in [30] a numerical solution for combined cryosurgery and hyperthermia that included multiple probes and different states of the tissue like frozen and unfrozen. However, the method was not validated with any biological tissue.

In addition to the impact of blood perfusion and metabolic heat on the formation of iceball, convective effect of large vessels on temperature distribution in ablation sites has been reported. A few studies involving blood flow were done, but most of them for hyperthermic ablation techniques [31, 32]. 3D visualization of simulated iceball is another important aspect of computer assistive tools which is presented in a recent study by Talbot et al. [33] and computed Hausdorff distance between the simulated and segmented isosurfaces from patient data is overlaid on the iceball as seen in Figure 2-1 but still the effect of large vessels was not discussed.

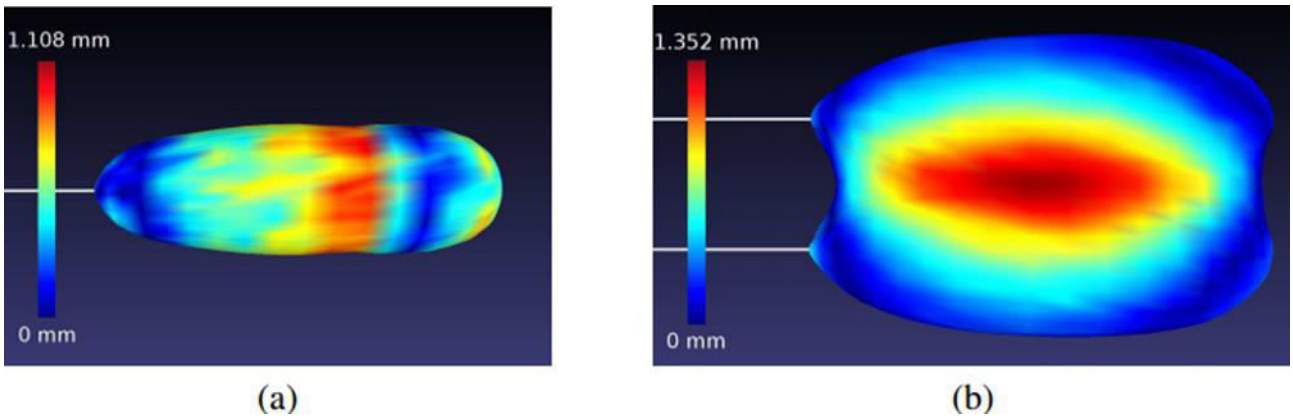

Figure 2-1 Hausdorff distance computed between the segmented and simulation based iso-surfaces a) one needle b) two needles [33]

In this thesis, we studied and developed a method of simulation of temperature propagation that considers the effect of large vessels on iceball formation. Since major blood vessels are remarkably resistant to cold injury, we considered large blood vessels without vessel occlusion. It can be particularly difficult to freeze large blood vessels if the blood flow through them is continued throughout cryosurgery. Only the outer layers are likely to be frozen and major blood vessels remain unfrozen [34]. This issue will be presented and discussed in Chapter 4.

2.3 Surgical planning

Let us recall that our objective is to have a multiple trajectory planning algorithm able to compute an optimal solution in a reasonable time, compatible with clinical routine. To achieve this, the surgical planning should be formulated as an optimization problem requiring to loop over parameters including a call to a function to optimize. This function also requires computing the simulation of the iceball in the case of cryosurgery planning. It is necessary to have both a fast evaluation of

the function and an optimization method converging quickly. In this section, we study the different optimization algorithms that have been proposed in the literature for applications related to the trajectory planning.

2.3.1 Cryosurgery

The surgical rules used to plan preoperatively a cryosurgery intervention are not well-studied and most of the studies on this topic have focused on optimizing the frozen area. One of the earliest examples of optimization method for the application of cryosurgery planning was done by Keanini and Rubinsky who solved the heat transfer equation for a 3D domain and applied the simplex method to optimize the number of cryoprobes and their geometrical dimensions (diameter and active length) [35]. However the optimization of other parameters, such as cryoprobe placement in the anatomy and the thermal protocol is more practical. Although the simplex method was appropriate for the particular examples in their study [35], it is an ineffective method when dealing with the problem of finding the best position of the probes due to the intrinsic non-linearity of the problem .

Their approach uses a very simplistic optimization model compared to the complexity of the whole problem due to the unconstrained and local nature of this optimization method, and other mathematically sophisticated approaches are more suitable for the problem. When applying traditional optimization techniques, the first big challenge is to build a suitable cost function to minimize. In fact, in general, we do not have an explicit formula for the distribution of the temperature field of the region which should be optimized with given boundary and initial conditions and moreover these conditions can also change depending on the case (e.g. where the cryoprobes are placed).

In a few studies, the gradient descent technique is applied to minimize objective functions defined by the behavior of the temperature field around the cryoprobes. [36] and [37]. Baissalov et al., studied simultaneous optimization of cryoprobe placement and bioheat simulation of ablation zone and described a 3D solution based on the cumulative 2D transverse planes, but the shown results were only for 2D state in a prostate model where the problem is simplified as all trajectories are parallel. A disadvantage of using gradient based methods for cryosurgical planning is the requirement of computing the heat equation several times (depending on the number of variables) in each iteration of the optimization.

In a study by Butz et al., [15] a software tool is presented based on 3DSlicer for preoperative planning of cryosurgery which can be extended to laser and radiofrequency ablation. Moreover, arbitrary virtual ablation devices can be added to the 3D scene and can be visualized using surface models. Ablation zones are modeled using a theoretical geometry. For cryoablation, the frozen volumes at the tip of each cryoprobe are approximated by ellipsoids. Geometric parameters of ellipsoids are calculated from previous patient cryoablations. The utilized optimization algorithm is based on the Powell method and in order to avoid dangerous trajectory placements they used a nonlinear term inside the objective function. However, the authors do not describe how the insertion zone is computed and which organs are considered for this region (see Figure 2-2).

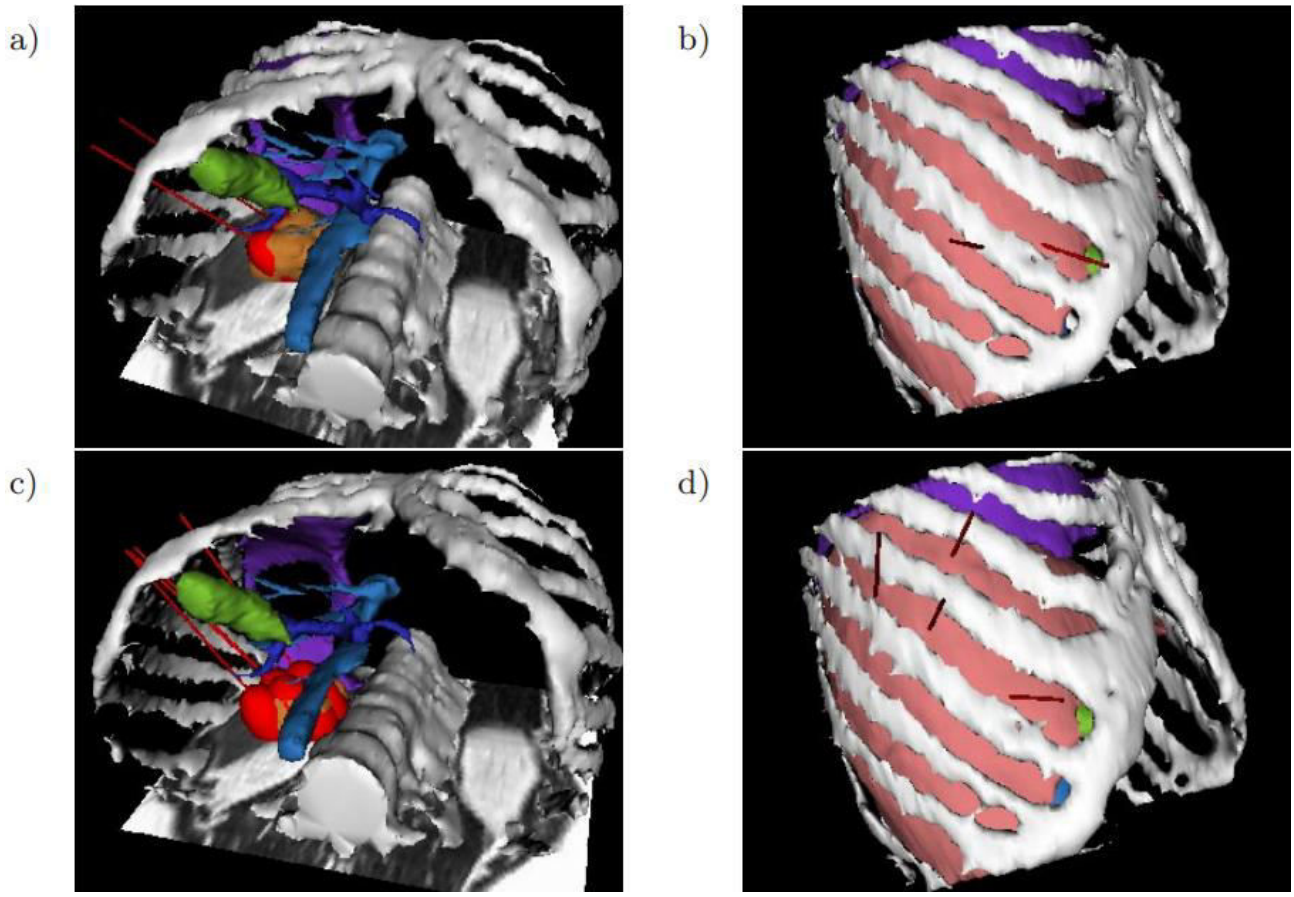

Figure 2-2 The virtual cryo-probes shown in red which simulate the needles and the frozen tissue, can be set into the patient's segmented anatomy. The tumor and its additional 0.5cm safety margin, is shown in brown. The large vessels are in blue, the gallbladder in green and the bones in white. a) and b) show the radiologists setup chosen for this specific case, while they can have a better setup which would have decreased significantly the danger of undertreating the cancer in images c) and d) [15]

The force field analogy method is a physically-based optimization method different from the previous techniques [38]. This method computes the defective areas, after the computation of the distribution of the temperature in the tissue at each iteration. In fact, for each pixel that did not reach a proper temperature (i.e. defective pixel), the method calculates a displacement vector for each cryoprobe and the result specifies the displacement of that particular cryoprobe at that given iteration. Unlike gradient descent techniques and simplex techniques, force field analogy requires a large amount of internal calculations except the computation of temperature field, so the computational time required converging a good solution is far from real-time applications. In studies [[39], [40]] using this approach, authors also focused on the 3D planning of prostate surgery in which all the cryoprobes are parallel and complexity of the problem is much lower than a free rotating cryoprobe problem.

One way to decrease the computation time of the optimization method in cryosurgery could be achieved by avoiding the computation of the temperature distribution at each iteration. For example, to plan placement of the cryoprobes one can focus on geometrical considerations and define methods converging to a configuration in which cryoprobes are evenly distributed in the tissue and are far apart from each other and distant from the boundary of the tumor. In the bubble-packing method described by Tanaka et al. [41], first ellipsoidal elements (or bubbles) are generated inside planning domain. Then, van der Waals'-like forces are simulated to move the bubbles until a minimum-force configuration is found (see Figure 2-3).

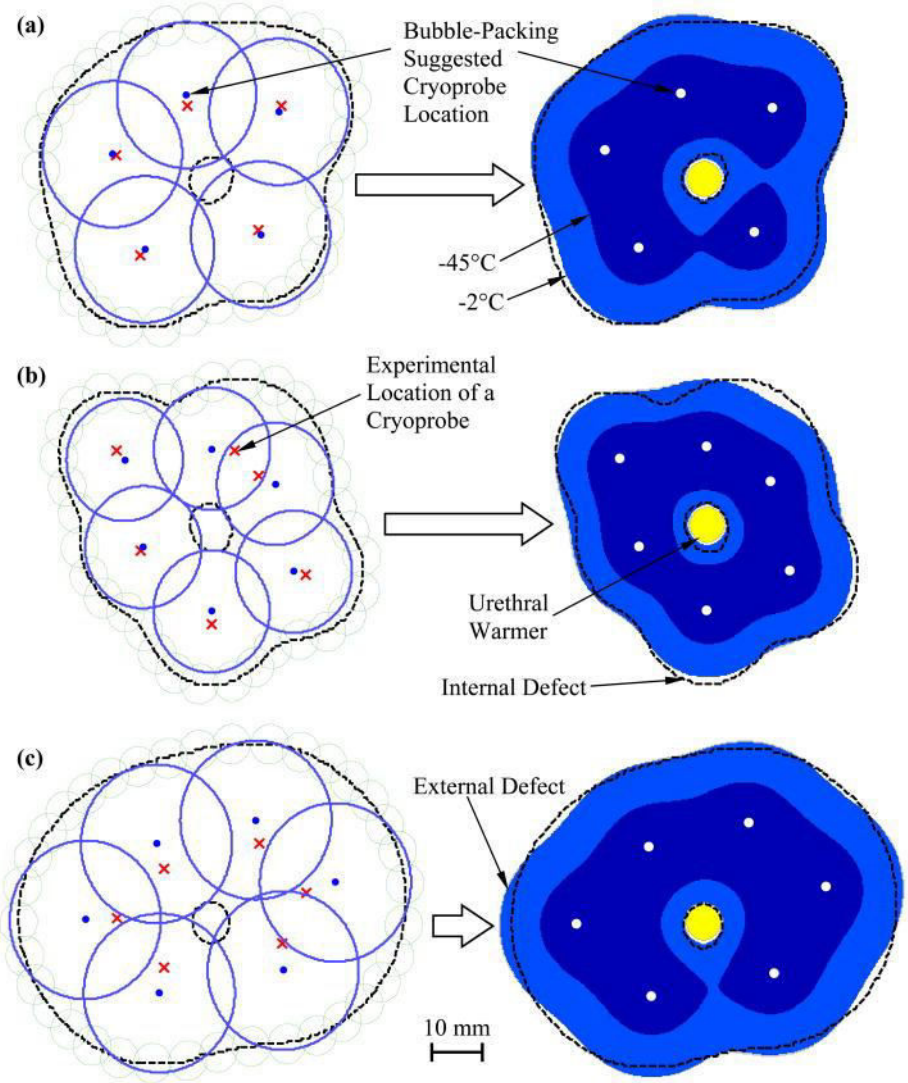

Figure 2-3 2D bubble-packing results and the corresponding simulated temperature field for three cases [42]

The method was first applied with the force field analogy method in 2D as an initialization tool [40] as well as a planning algorithm used to study 2D prostate planning [42] .

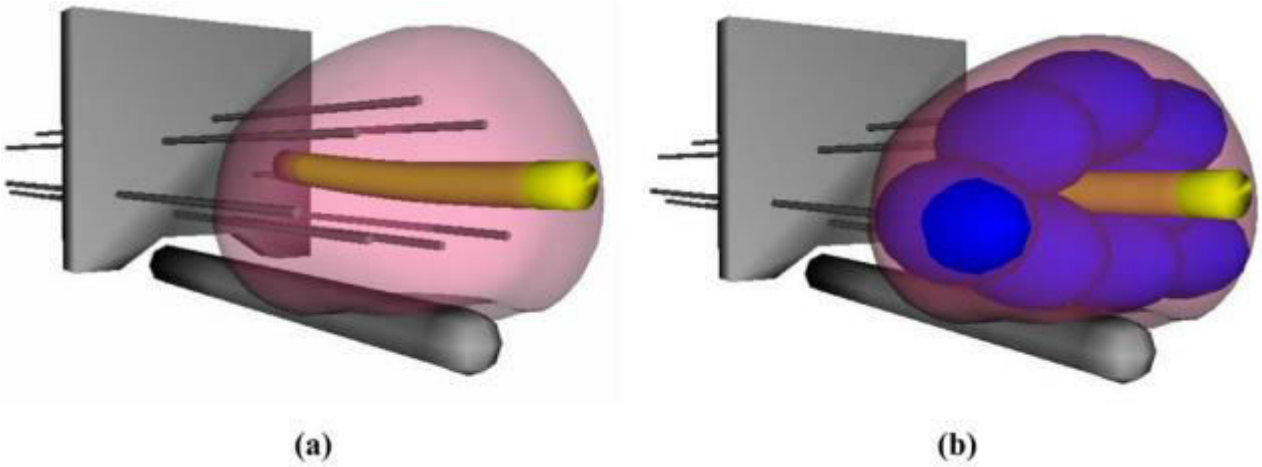

Figure 2-4 Schematic illustration of cryosurgery planning: (a) the prostate and urethral warmer are modeled based on ultrasound images, (b) bubble packing generates a recommended cryoprobe layout [41]

They compared planning results with experimental results and reported a small error factor in the location of inserted needles (see Figure 2-3). In a separate study this method was successfully used to optimize the insertion depth in 3D [43] (see Figure 2-4).

In 2011, Giorgi et al. [44] reported the application of a particular method among genetic algorithms called ant colony optimization (ACO) inspired by [45] to cryosurgery planning. Such an approach has the advantage to be completely general and allows for the setting of different types of experimental parameters without changing the optimization technique. Computation of the cost function is based on the numerical solution of several direct Stefan problems solved by an Euler-Galerkin approach. However, similar to the force field analogy method, this method is not able to provide real-time results either and was done on a 2D standard prostate phantom (see Figure 2-5).

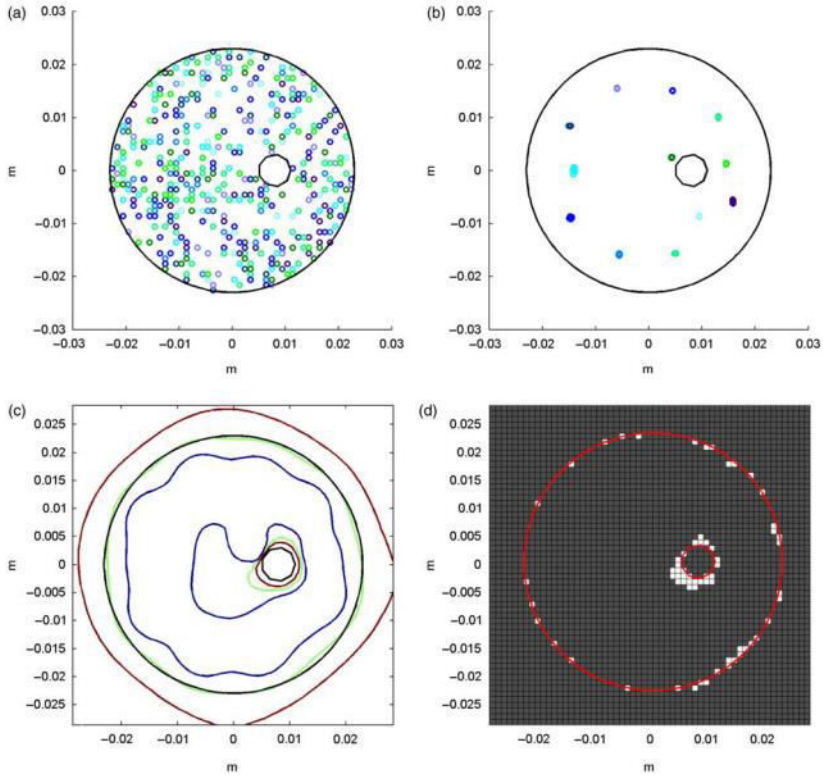

Figure 2-5 Case of 12 cryoprobes (a) Initial position of configurations (where each small circle represents a cryoprobe, cryoprobes of different colours belong to different configurations, and the tumor is represented by the large black circle). (b) Final position of the configurations collapsed into one after ACO. (c) Temperature distribution for the optimal solution (i.e. the one characterized by the minimum value of the cost function): 0°C isotherm contour is red, -22°C isotherm contour is light green, and -45°C isotherm contour is blue. (d) Plot of the defected pixels (white) [44]

2.3.2 Other types of hyperthermia

As explained in Chapter 1, many other types of ablations by hyperthermia can also be chosen by surgeons, and their pre-operative planning presents similar issues. Littmann [46] introduced a software for in-situ laser induced thermotherapy (LITT) ablations in oncologic liver surgery. LITT applicators are represented as surface models and can be visualized in 2D slice views as well as in a 3D surface rendering. Moreover, the ablation zone can be simulated after segmenting the intrahepatic structures. The heat transport which incorporates heat-sink effects of the nearby vessels within the liver tissue is calculated using a finite difference method. In the planning step, the applicators are automatically arranged in the form of a regular polygon around the corresponding tumor's

center of gravity and are aligned to the tumor's longest main axis. This method is a fast but not optimal way of planning because it can't guaranty the full tumor coverage and minimum damage to the healthy tissue. However, it is required to check whether any bone structures or main vascular branches lie within any applicator's path which should be done manually and interactively using combination of surface rendered 3D scene with volume rendering of the original data set. Illustration of this method is shown in Figure 2-6.

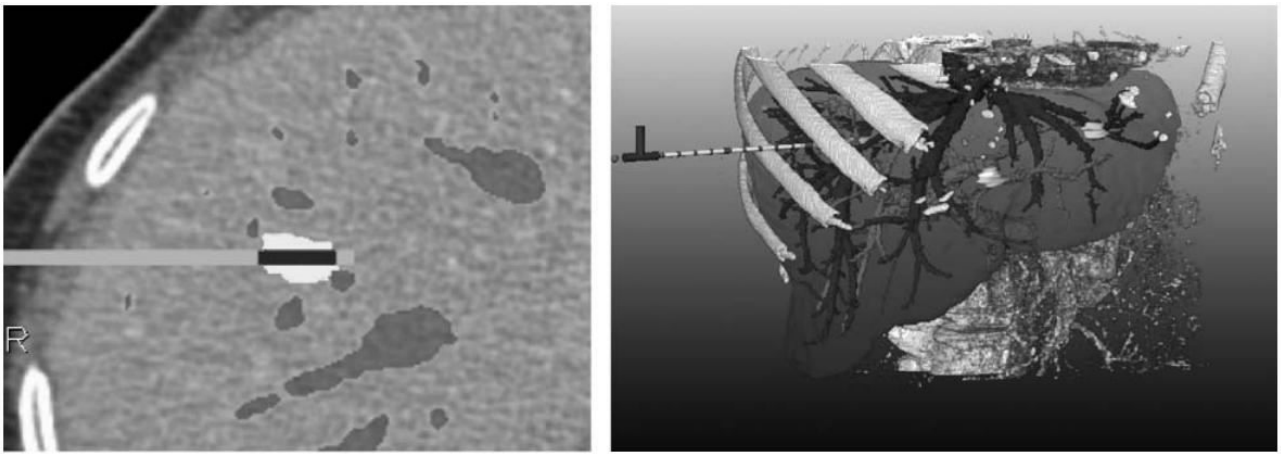

Figure 2-6 Synchronous 2D and 3D views enable the user to quickly check if either bony structures or important vessels lie on an applicator's path [46]

Preoperative planning of RFA treatment for the ablation of hepatic tumors was described by [16]. In this work, liver, blood vessels, pathologies, and the surrounding organs are segmented and visualized using surface rendering. Also, virtual RF applicator models with idealized ellipsoidal ablation zones are available. To model the heat-sink effect, the ablation zone models are deformed in real-time by moving their vertices according to the proximity of large surrounding liver vessels [47]. In a technical point of view, a morphological erosion operation is applied to mask of the vessel to eliminate small vessels (< 2-3 mm) in a preprocessing step. By further dilations, a deformation zone is computed to define the amount of vertex translation. Besides the restriction of the possible vertex deformation of the ellipsoid, this approach is completely heuristic; therefore it is not clear how an applied deformation influence the biophysical heat-sink effect of the blood vessels while performing RFA (see Figure 2-7).

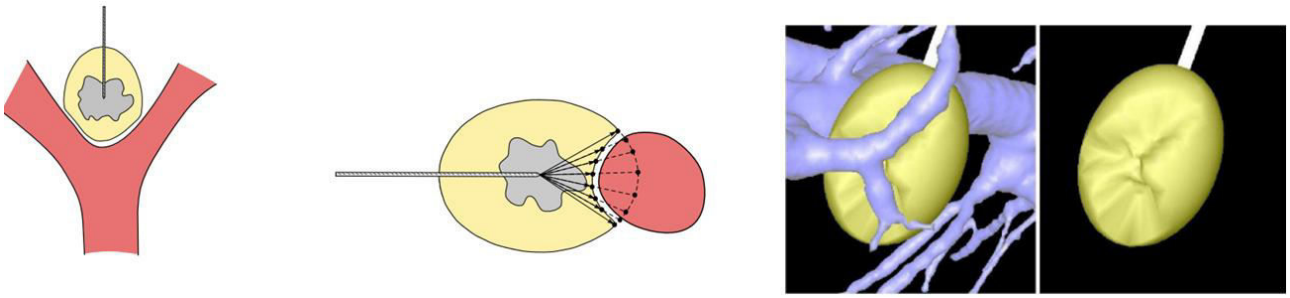

Figure 2-7 Ablation zone models are deformed in real-time by moving their vertices according to the proximity of large surrounding liver vessels [47]

Villard and Baegert proposed a method based on geometric constraints solving for automatically computing insertion trajectories for single-needle [10, 48-51]. In this study, the target point and an insertion point on the skin are connected by an insertion trajectory. Hard constraints are formulated to compute insertion zones on the skin. Insertion zones represent regions in which trajectories can pass safely to the target and do not violate any restriction on the insertion path such as anatomical

structures collision or exceeding the needle length. Then the quality of the allowed trajectories is scored by the so-called soft constraints. These constraints represent some numerical parameters such as the distance to critical structures, or the volume of the ellipsoids. These soft constraints are combined using a weighted sum to obtain an overall rating of candidate trajectories, which are displayed as a color map on the insertion zone (Figure 2-8). Optimizing the weighted sum allows to propose an optimal trajectory.

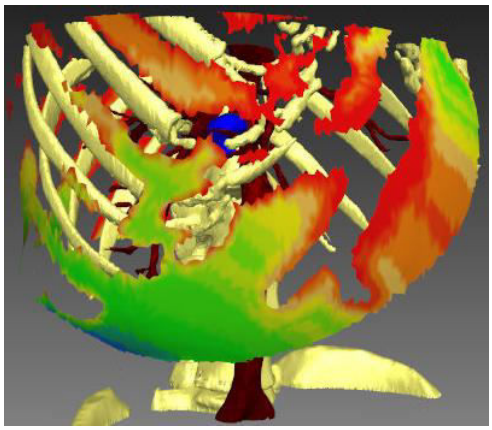

Figure 2-8 Color map is overlaid on a pre-computed insertion zone using a weighted sum of soft constraints. Red represents high risk regions while green shows the safe ones.

In another very similar work, Seitel in collaboration with Villard displayed sequentially hard and soft constraints as color maps (Figure 2-10) but they tried to compute the corresponding Pareto front instead of one optimal solution from the final weighted objective functions [9]. They still used only one single needle for their computations and planning. In both cases, the components of the workflows have been developed within the Medical Imaging Interaction Toolkit (MITK) [52].

In a similar way, Schumann et al. [53] used a set of constraints to determine the suitable insertion trajectories, but with a method independent of the mesh representation of the critical structures. They generated constraint maps for each surgical rule by computing a cylindrical projection from the center of the target. Each constraint map is rated by a constraint-specific rating function and merged to a weighted combination of all constraints. The maximum value in this combined map corresponds to the possible insertion trajectory. However the coefficient of each constraint still needs to be set manually and an evaluation showing the clinical applicability of this proposed planning system has not yet been performed (Figure 2-9).

In a different way from the previous works, Kröger et al. [54] presented an approximation of the numerical forward simulation. In this approach, the ablation zone for each patient is parameterized by several reference configurations, which are pre-computed and saved in a lookup table. During applicator probe placement, the patient-specific ablation zone is reconstructed from the lookup table under consideration of the Euclidean distance metric from the probe to the blood vessels and its radius, allowing for interactive frame rates. The major disadvantages of this method are that the basic shape of the ablation zone consists of several spheres along the points of the probe and the important assumption of an independent cooling effect for each vessel segment. This approach is then integrated into a medical application, for slice-based rendering of the ablation zone in [55] which permitted the surgeon to plan interactively by looking into visualized ablation zone.

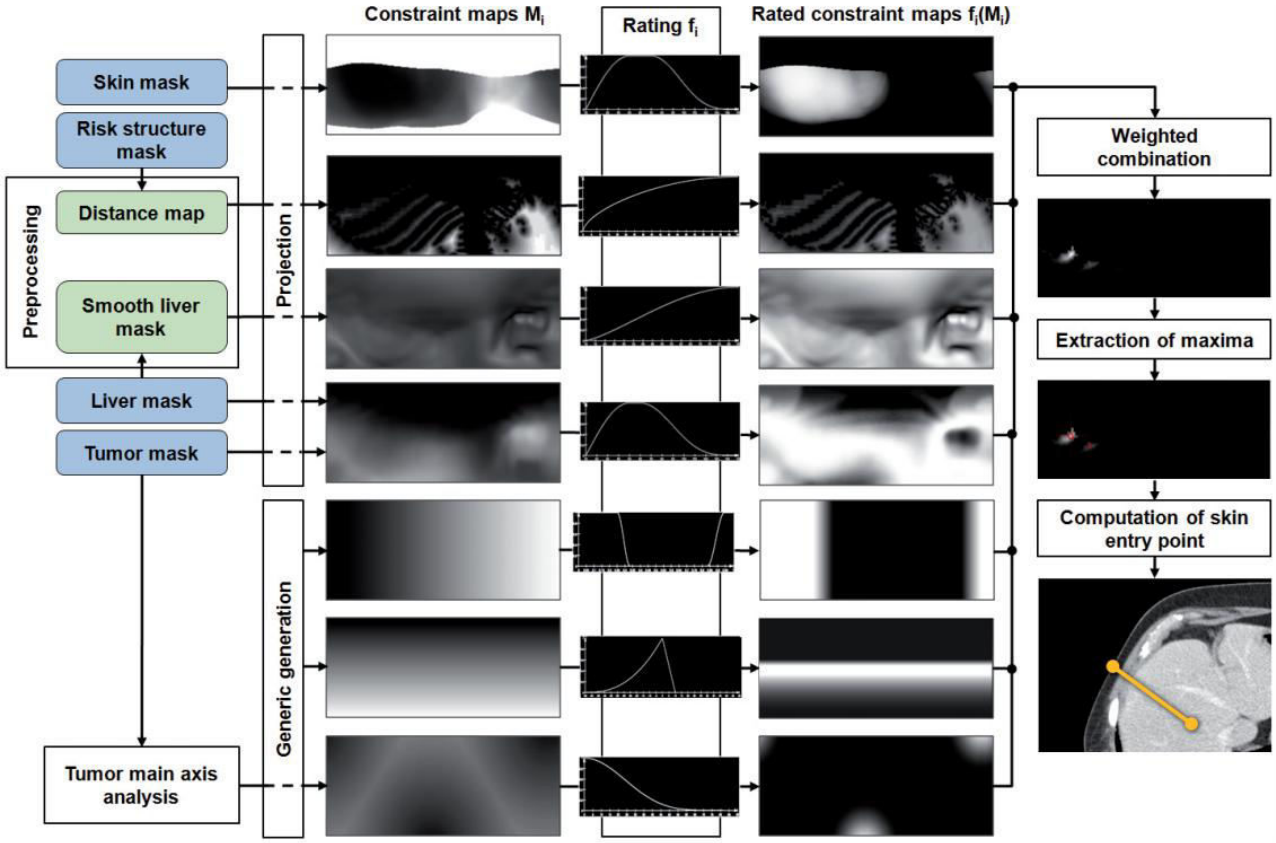

Figure 2-9 Outline of the algorithm: Input masks (blue) are used to generate constraints maps and preprocessing results (green) (in vertical order: penetration depth, distances to risk structures, liver capsule penetration angle, portion of healthy liver tissue, circumference, angulation, tumor coverage). They are rated and combined into one image from which maxima are computed [53].

Trovato et al., [56] also used an approximation of combined multiple ablation zones alongside their semi-automatic RFA planning system. Their planning suffers from the lack of a visualization method and consideration of heat-sink effects.

Rieder et al., [13] modeled an approximation of the ablation zone. They sampled the applicator's probes and a weighted distance field was calculated, then the ablation zone was fitted to the resulting necrosis mask of a complex numerical simulation. Heat-sink effects are estimated by solving the thermal equilibrium of the vasculature and the combination with the weighted distance field (see Figure 2-11).

However, the drawback of this method is that only the minimal distance from a sample to the nearest vessel is encoded. That is, combined cooling effects of two nearby vessels cannot be described by this method. If multiple vessels are located close together, the coagulation zone suffers from spurious sharp edges, as can be seen in Figure 2-12.

In a recent study, Ren et al. [57] presented a planning system for tumor ablation to achieve full tumor coverage and also to minimize the number of ablations, number of needle trajectories and over-ablation of healthy tissue. These objectives are taken into account using a genetic algorithm mechanism. A concept of sphere covering was used in this study and an exponential weight-criterion fitness function has been designed incorporating constraints that were reflective of different objectives. In this study, authors did not consider rotation of the trajectories, they did not search all possible solutions on the skin, and one region satisfying anatomical obstacles was preselected

(see Figure 2-13).

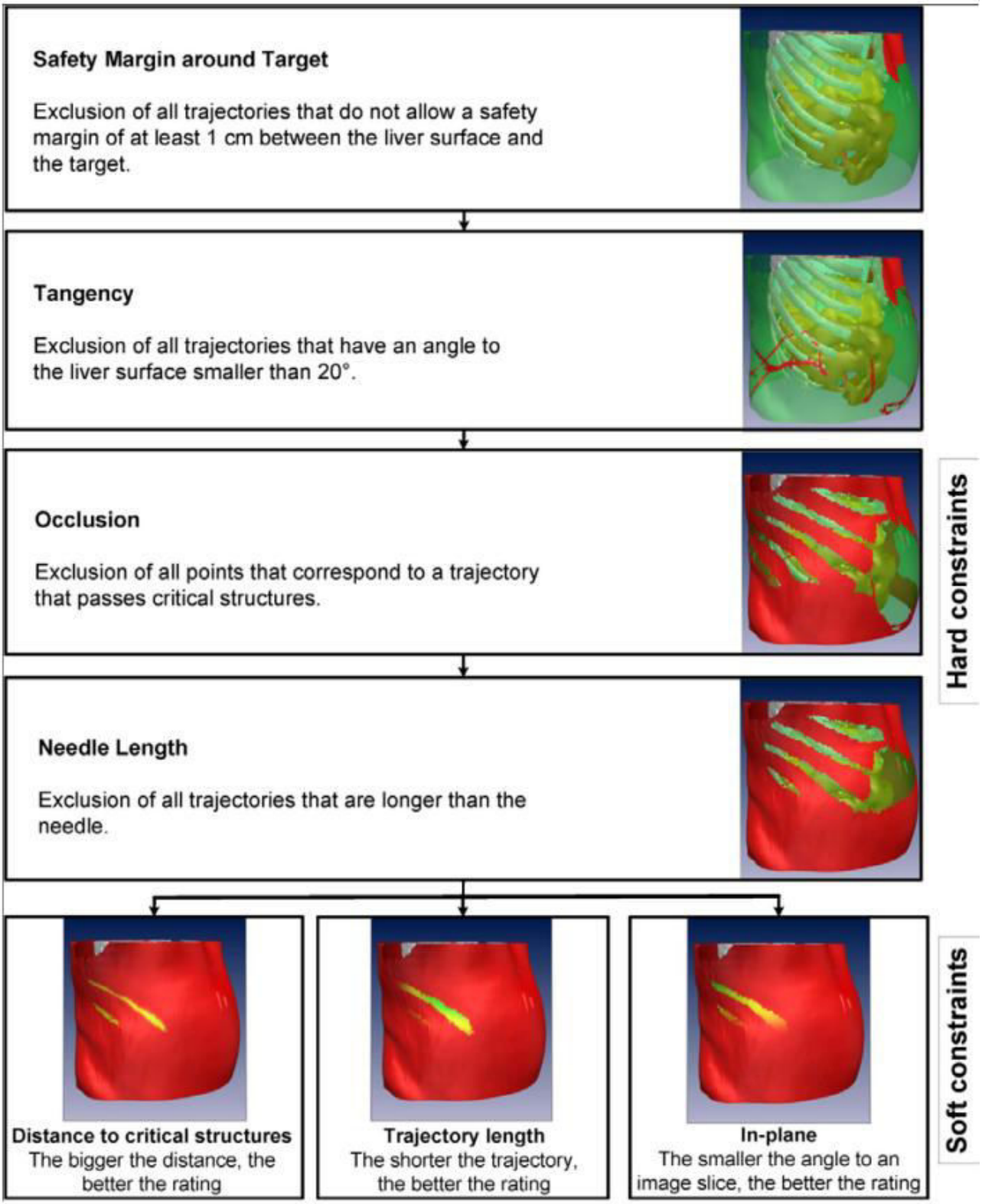

Figure 2-10 Trajectory planning workflow and resulting surfaces. For the hard constraints, the insertion zone is shown transparently green. The result of the soft constraints is visualized with a color gradient ranging from red (poor rating) to green (good rating) [9]

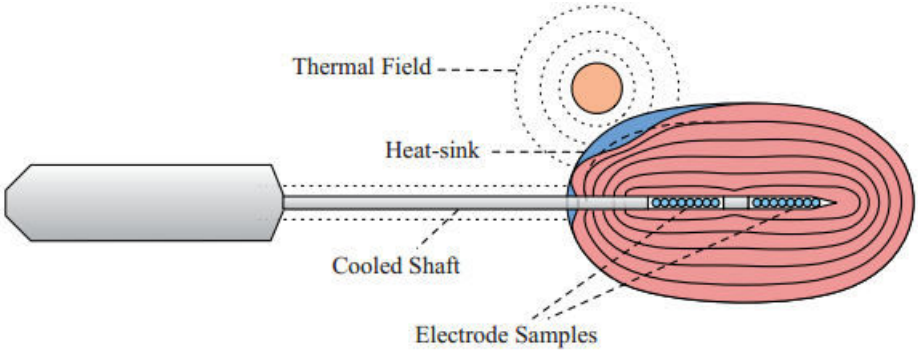

Figure 2-11 Both probes of an internally cooled bipolar RF applicator are sampled. The corresponding weighted distance field is illustrated by isoline contours. The thermal fields of the blood vessels and the cooled applicator shaft decrease the ablation zone (blue regions) [13]

2.3.3 Deep brain stimulation DBS

Computer assisting tools for deep brain stimulation procedures are classified into automatic localization of target, placement of surgical tools and simulating the effect of treatment. Automatic placement of surgical tools will be discussed in this section as opposed to traditional trial and error searches performed by surgeons. In a first work for automatic DBS trajectory placement by Brunenberg et al. [58] a number of insertion points on the skull is randomly selected from the predefined frontal lobe gyri. A straight line from the insertion point to the target is drawn and multiple cost functions based on the Euclidian distance to vital regions like vessels and ventricles are computed. For this purpose the distance of each point on the trajectory to the vessels and ventricles is computed using a trilinear interpolation which makes the computations heavy. As the authors restricted search domain to a set of entry points, there would be good solutions which are not possibly discovered (see Figure 2-14).

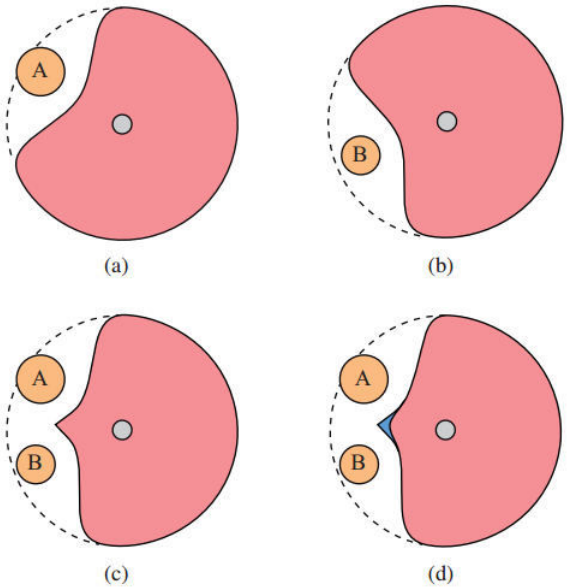

Figure 2-12 In (a), The vessel A presence leads to a deformation of the ablation zone in accordance with the heat-sink effect. A similar situation is illustrated in (b). If an independent cooling effect is assumed, the final ablation zone is achieved by the intersection of both ablation zones (c). In contrast, if both vessels jointly cool the heat field, the heat-sink appears more smoothly (cf. blue peak), similar to the results of numerical simulations (d) [13]

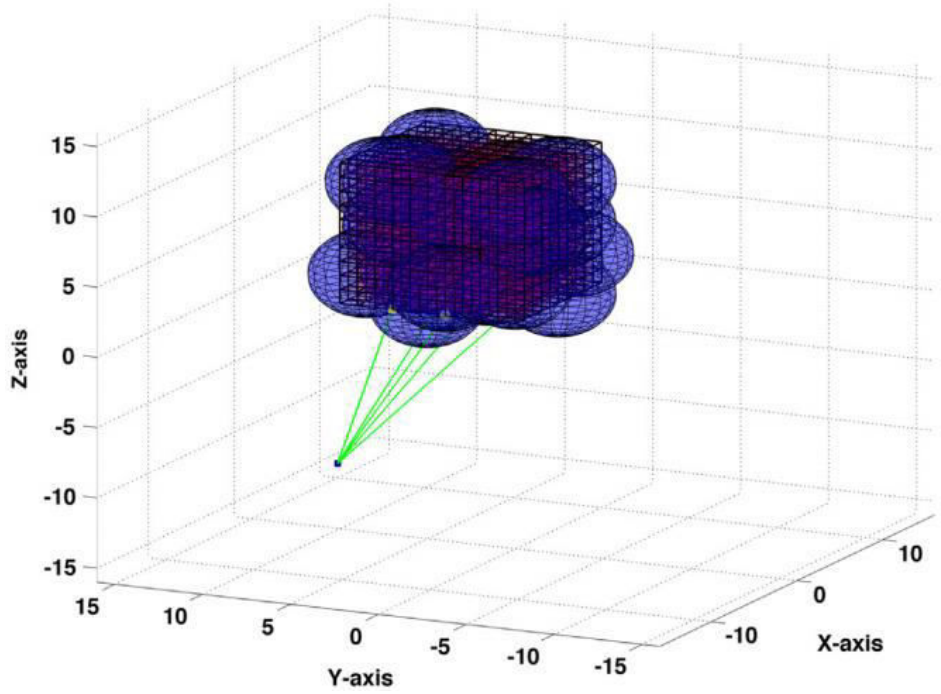

Figure 2-13 An example of ablation spheres and trajectories; blue spheres indicate the ablation spheres and green lines indicate possible needle trajectories [57]

In another survey, Essert et al. [59] tried to test all possible solutions by letting the software to decide which points to choose as long as they satisfy the intervention rules. This work was based on resolution of some geometric constraints which was inspired by their previous works on RFA [50]. Not feasible regions which pass through cortical sulci and ventricles were removed within a short time in a preliminary stage. Then, multiple colored maps are generated by translating surgical rules called soft constraints into the quantitative scores. The color maps represent the risk due to distance to sulci, length of the path and orientation of the trajectory.

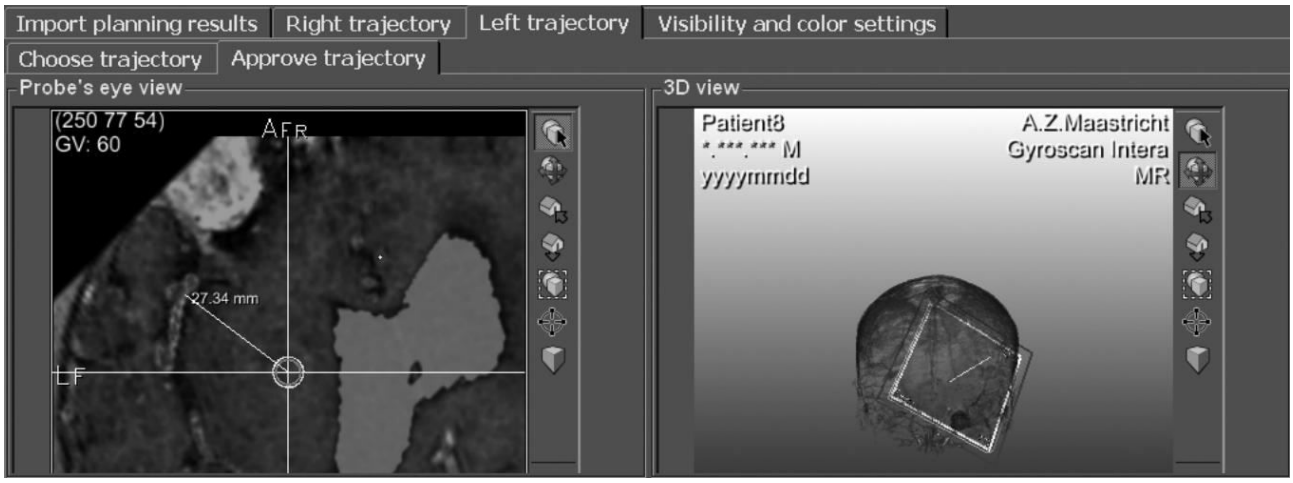

Figure 2-14 An automatic planning tool for DBS presenting approved trajectory to the neurosurgeon [58]

Finally the surgeon can decide the best solution based on each of the mentioned maps or an aggregated color map generated from these maps with pre-defined weights (see Figure 2-15).

2.4 Problem statement

The overall objective of this thesis is to provide the surgeon an automatic pre-operative path planning tool able to propose a setup for placement of multiple needles in 3D, taking into account several surgical constraints as mentioned in section 1.3.1, as well as a precise computation of the frozen area. This package provides all required tools for the visualization and interaction of standard medical imaging data plus a generic framework for a fast extension of new applications or surgical rules.

As discussed in this chapter there exist several tools for different minimally invasive surgical planning procedures in the literature but each one with its own advantages and drawbacks. The following list states the main differences and goals in current work comparing to others:

All previously mentioned studies in cryosurgery planning were mostly done for prostate in which needles are placed in parallel to each other. This approach is too restrictive for liver cryosurgery because it is possible to locate the needles with different directions and origins to obtain an optimal ablation. So in order to apply our method to liver tumors, we considered needles to have 5 degrees of freedom: 3 translations for position and 2 rotations for orientation.

An automatic planning is introduced considering surrounding obstructive or vital organs like ribs and vessels. This is done only once for each patient and pre-operatively then results will be used for the real-time intra-operative planning purposes. This is different with some of the discussed methods which let the operator to consider these obstacles manually and interactively or with a high computational cost in their planning phase. Moreover, adding new constraints to our tool is easy with no requirement to modify the code or make a lot of configurations, thanks to its generic structure and XML parsing system for the constraints definition.

The effect of large vessels is not considered in any of other cryosurgical planning tools besides an accurate simulation of the heat propagation. This effect was studied by several works in RFA planning like [47] [13] which is inspiring to consider an estimation of the large vessels effect in the computations.

This work proposes several solutions to the surgeon based on his needs and requirements. It can be as simple as visualizing the simulated ablation zone generated by multiple needles and interactively modifying their placements or automatically plan the surgery using simplified ellipsoids or simulated iceballs. Due to high computational cost of the last option a two-phase fast converging solution is also designed for intra-operative planning.

Finally, in each part the results are discussed and validated using different methods to demonstrate the accuracy and amount of expected improvement for each solution.

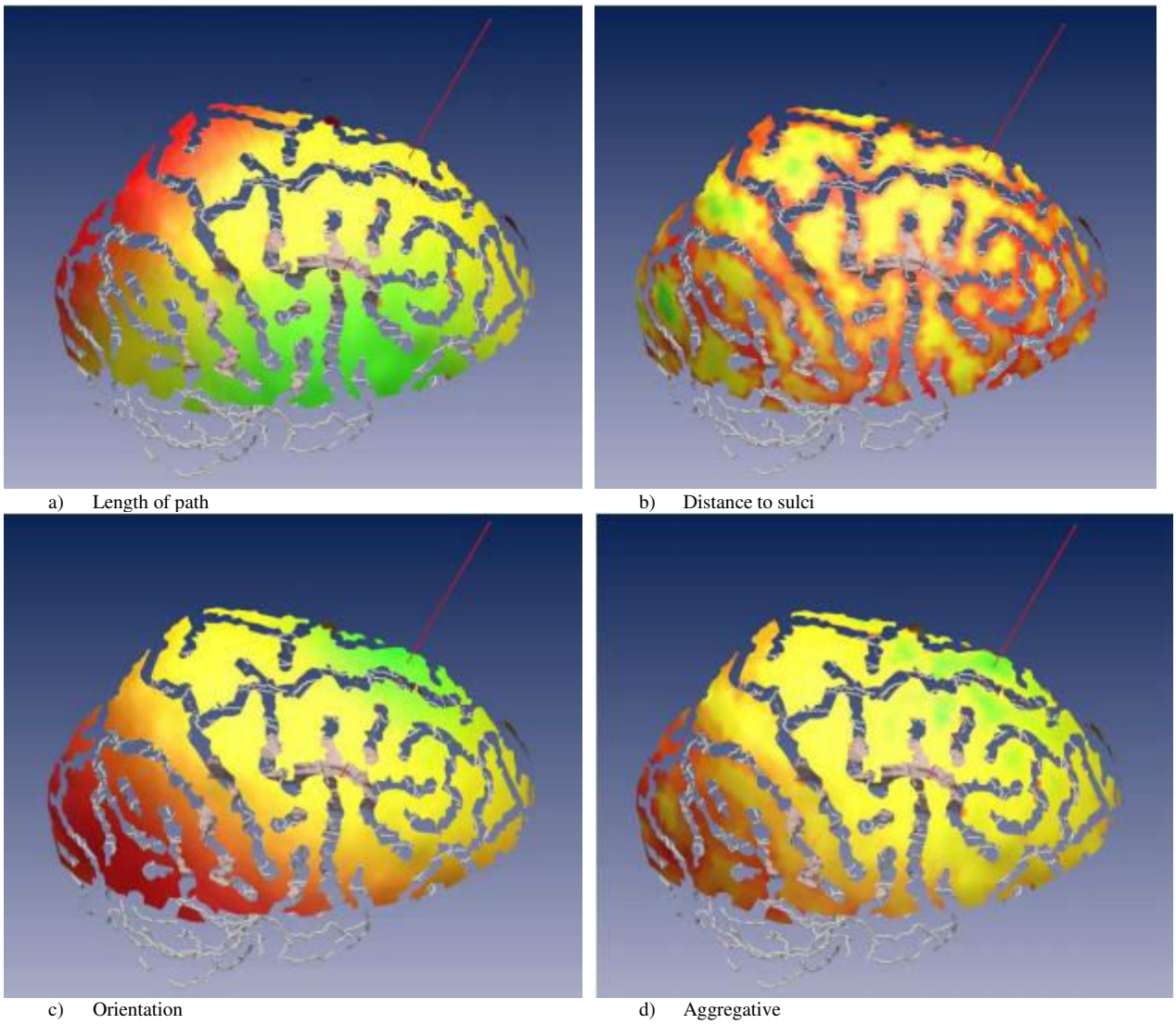

a) Length of path

b) Distance to sulci

c) Orientation

d) Aggregative

Figure 2-15 Color maps of the soft constraints obtained after phase 2 of the solving process: best zones are in green and worst are in red. The best trajectory is shown as a red line [59]

Chapter 3. Data preparation and preprocessing

3.1 Overview

As briefly discussed in chapter 1, several steps are required to compute the optimal trajectories. This chapter covers the primary steps in our proposed workflow, including the description of required dataset characteristics and their preprocessing that consists of data preparation and computation of the insertion zone. The simulation and optimization approaches we describe in Chapters 4, 5 and 6 receive as input data structures computed from pre-operative patient images and then, in order to evaluate accuracy of the obtained results, intra- operative patient images are used as a reference for comparisons. This input data should be carefully prepared according to several factors like software requirements, design of the experiments for problem complexity, and comparisons and validation purposes. Section 3.2 describes dataset properties and the data preparation steps which includes image registration between pre- and intra- operative images, segmentation of structures of interest, tumor dilation and generation of 3D meshes. The next phase in preprocessing is to compute a safe insertion zone on the skin usable for path planning, as described in Section 3.3.

3.2 Data preparation

Our planning tool requires as an input several anatomical structures. These input images are used for internal computations and also for evaluating the methods. We have used two sets of data throughout this manuscript. The first dataset is a retrospective dataset from a patient who underwent liver tumor cryosurgery, and includes pre- and intra- operative images. According to visibility of the iceballs and vessels in this dataset, it has been used for validation purposes in the following chapters. The second dataset provides us with a sample of preoperative images of the liver with several tumors. They were used for experimenting the algorithms of our workflow. Different experiments were designed based on the tumor size and location in relation to the other structures in order to test speed and accuracy of the proposed methods.

3.2.1 Retrospective dataset

The retrospective dataset used in this thesis was obtained thanks to collaboration with the Memorial Sloan Kettering Cancer Center[1]. It consists of multiple MRI scans of one patient with two

[1] http://www.mskcc.org/

tumors undertaking liver cryosurgery. One of the tumors was treated with one needle while the second one was ablated using two needles. Images were in the raw DICOM format. They were used to extract regions of interest. Due to the tissue displacements in different scans, an alignment was required as explained in the next sections.

3.2.1.1 Image characteristics

Pre-operative:

DWI images with contrast agent and 5mm of slice thickness were used for localization of the tumor. Non-isotropic T1 images with dimensions 1.6*0.5*0.5mm were used for segmenting all anatomical structures except the tumors because of low contrast. These images were also with contrast agent, which enabled segmentation of the portal vein.

Intra-operative:

During the intervention and after inserting the needles an image was taken showing location of the needles before starting the freezing step. Then progressively several images were taken while freezing for each tumor. Five slices were available in each step with 8mm of slice thickness in the location of the iceballs. These samples were very sparse and needed to be treated carefully while registering and segmenting the iceballs.

These scans were available during the iceball formation for both tumors in the tenth minute, after five minute of thawing and eighth minute in the second phase of freezing.

3.2.1.2 Registration

Due to the nature of our dataset, ribs and spine were not visible so a solution for this problem was moving and aligning CT images of another patient to the coordinates of our patient. This was

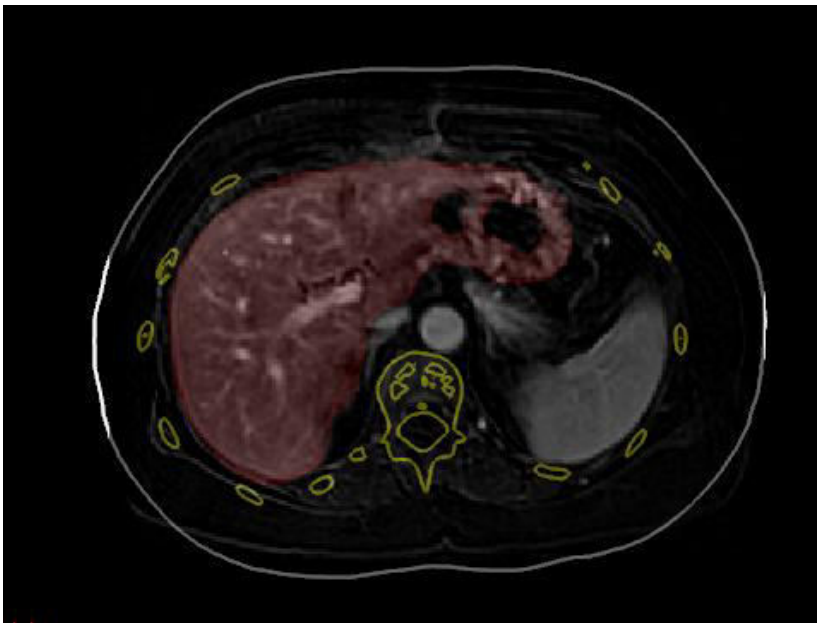

Figure 3-1: Ribs in yellow and skin in white registered on MRI image of the patient. A segmented part of the liver also can be seen in red.

done with a rigid registration method using MITK[2] registration plugin. This step was further validated visually with the few available CT scans of the same patient sent from the MSKCC (see Figure 3-1).

Due to the small field of view of the captured images, the skin was truncated in both sides close to the liver where the needles are most likely to be inserted, which was a problem for our planning approach. Therefore a similar method was used to align pre-segmented skin to our patient (See Figure 3-1).

Intra-operative images were also registered to preoperative T1 space using rigid and similarity registration methods in MITK (see Figure 3-2).

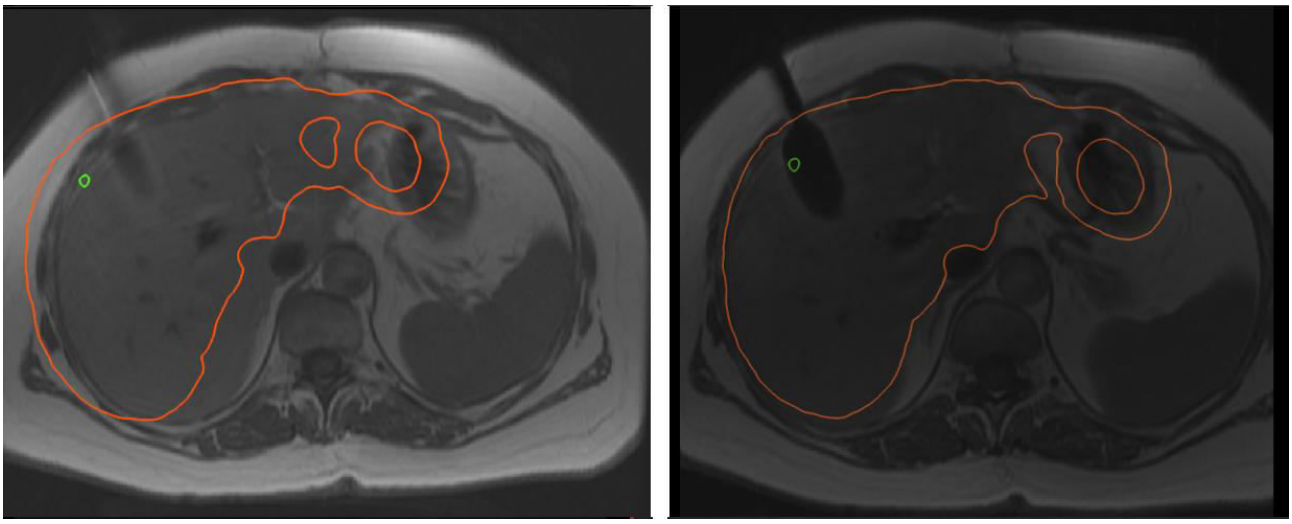

Figure 3-2: Intra-operative images are aligned to T1. Red contour shows liver from T1 high-resolution images, green represents tumor location while background image demonstrates intra-operative image

3.2.1.3 Segmentation

Liver and vessels segmentation was done semi-automatically based on a region growing method to reduce interaction time which helps segmenting the liver and vessels in 3D Slicer. Portal vein and arteries were segmented separately for future use.

Tumor, iceball and needle tip segmentation was done manually with Regions Of Interest (ROI) drawing in 3D Slicer. These 2D slices will be used in Chapter 4 for slice-based validation of ablation region. They were also used to generate surface meshes.

3.2.1.4 Mesh generation

Surface meshes of segmented ROIs were created using marching cubes algorithm included in MITK or 3D Slicer.

3.2.1.5 Tumor dilation

Segmented tumor was dilated with a 2mm dilation filter in 3D Slicer to satisfy safe margin condition (see Figure 3-3).

[2] Medical Imaging Toolkit

In the end we obtained all 3D meshes required by our planning workflow in the same coordinate system: tumor, portal vein, liver, ribs and skin. Iceballs were also generated for validation purposes (see Figure 3-4).

Figure 3-3: Tumor dilation to create the safe margin. Green patch represents 2mm dilated version of the tumor in red

3.2.2 Test dataset

Due to the difficulty to gather exploitable datasets of both pre- and intra- / post-operative images of patients who underwent cryoablation, as suggested in the previous section, we performed most of the experiments of our algorithms on six pre-segmented liver datasets from IRCAD[3] online database. They were used in this thesis for test and demonstration purposes. These were pre-operative images that only represented the anatomy and lesions, and no treatment had been performed. All

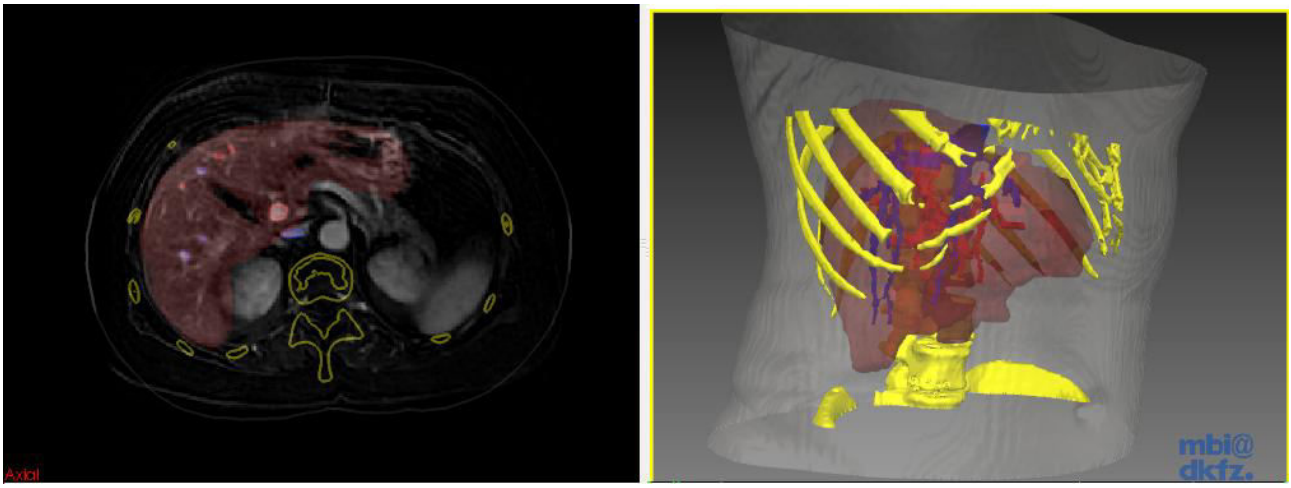

Figure 3-4: Left: 2D segmented organs; Right: surface meshes of the segmented organs

[3] http://www.ircad.fr/research/3d-ircadb-01/

organs required for the preprocessing step of our software were available by default in the format of 3D masks and meshes. As the complexity of the planning problem depends on the size of the tumor and its position in relation to the other structures, some of the tumors in these datasets were manually moved to produce problems with increasing complexity. These ordered cases were used to test our proposed workflow in different pre-defined complexity levels.

3.3 Computation of insertion zone

As listed in section 1.3.1 several constraints are considered in our planning tool. Some of them are Boolean and the trajectories violating these constraints are not feasible in the cryoablation procedure. These so-called hard constraints try to avoid trajectories which do not satisfy all of the feasibility criteria we used: 1) not passing through anatomical structures like ribs or vessels, 2) have a length lower than 120 mm, and 3) reach the liver with an angle higher than 20 degrees to its surface in order to avoid slipping on the capsule. In this section our planning tool delineates on the skin a feasible *insertion zone* (set of feasible *insertion points)* based on the hard constraints discussed above. Our planning tool needs to receive as an input several 3D triangular surface meshes of anatomical organs and lesions. The hard constraints are evaluated in a pipeline considering candidate trajectories as lines from a point on the skin (*entry point*) to the tumor. This entry point should be removed from the insertion zone if its corresponding trajectory does not fulfill the hard constraints.

Constraint 1) mentioned above can be seen as a visibility constraint. Therefore, to handle this specific constraint in a short computation time, a line of sight problem is solved by placing a virtual camera in the tumor position looking towards the skin, and removing from the set of insertion points the ones that are occluded by the anatomical structures (see Figure 1-5). For needle length constraint 2), all entry points which have a distance to the tumor higher than 120 mm are removed from the insertion zone (see Figure 1-6). For tangency constraint 3), candidate entry points are eliminated if their associated trajectory has an insertion angle of less than 20 degrees with the triangle of the liver mesh where it arrives. All this approach relies on previous works of our research group [9] for single needle placement, including a fast GPU based algorithm for constraint 1). This approach is independent from the number of needles and for multiple needle placements the results can be used for each needle separately, as each needle needs to be inserted in a feasible location. Figure 3-5 demonstrates a sample input for the algorithm and the computed insertion zone as an output. Using this pre-computed insertion zone highly reduces the amount of computations required in the planning phase.

In all the computations above trajectories are considered as a straight line from the barycenter of the tumor towards the skin. The boundaries of this insertion zone should be modified if one decides to place the needle tip in a position other than the barycenter but still inside the tumor. This change directly depends on the amount of displacement to the tumor barycenter and thus to the size of the tumor. In order to solve this issue, a compensating term added to the objective function which computes the distance to the ribs and vessels. Its formulation is described in Section 6.3.1 so the optimizer tries to avoid not feasible trajectories even on the boundary of the insertion zone.

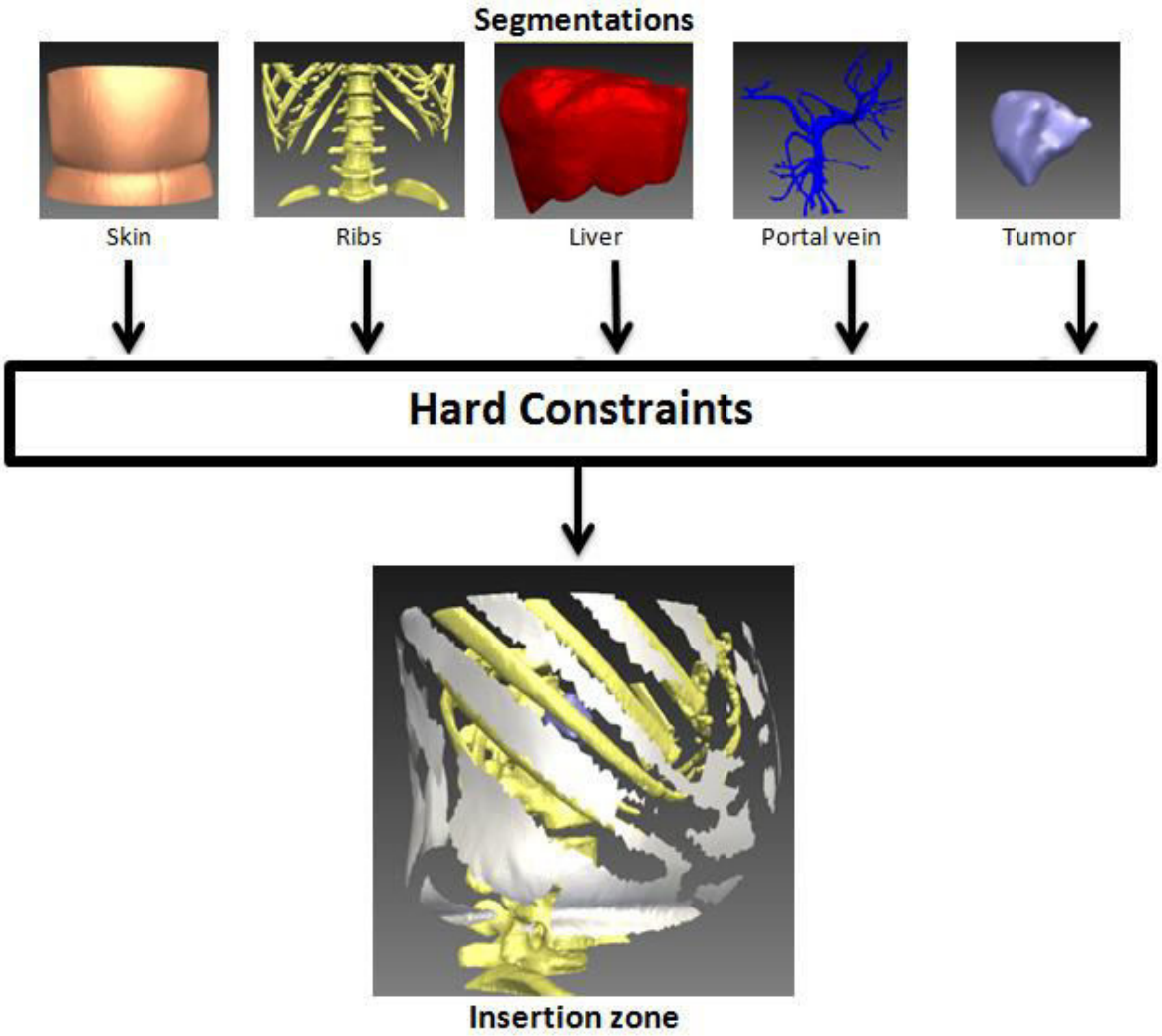

Figure 3-5 Constraint concept of the automatic trajectory planning. Surfaces of the skin, the liver, the tumor and other critical structures are created from corresponding segmentations. The insertion zone on the skin is determined after applying a combination of hard constraints

Chapter 4. Simulation of cryosurgery

4.1 Overview

In this chapter a typical multi-probe cryosurgery is simulated based on a heat capacity model and a finite difference method. Section 4.2 explains in detail the method we used, then in section 4.3 numerical values and conditions are discussed. The remaining sections show and discuss the results.

4.2 Numerical method of the heat propagation

In this section, we explain the approach we used to simulate multiple probe thermal propagation to predict the outcome of the cryosurgical procedure. The results of the simulations are quantified in terms of isotherm locations at any given time with respect to the anatomy. This provides a means for analyzing the effectiveness of the treatment. Our method consists of a time-dependent model of iceball formation based on Pennes bioheat transfer equation [60] around the needle tip, which includes the influence of blood perfusion and the metabolic heat on the temperature distribution of the tissue.

$$C_u \frac{\partial T_u(X,t)}{\partial t} = \nabla . k_u \nabla [T_u(X,t)] - \omega_b C_b T_u(X,t) + Q_m + C_b \omega_b T_a \qquad X \in \Omega_u(t) \tag{4-1}$$

Where C_u, C_b are, the heat capacity of unfrozen tissue and blood, respectively; X contains the Cartesian coordinates x,y and z; $T_u(X,t)$ is the temperature of unfrozen tissue; k_u is the thermal conductivity of unfrozen tissue; $\Omega_u(t)$ indicates the unfrozen domain at time t; ω_b is the blood perfusion; Q_m is the metabolic heat generation; and T_a is the arterial temperature;.

Since the frozen area lacks blood perfusion and metabolism, the heat balance can be expressed by:

$$C_f \frac{\partial T_f(X,t)}{\partial t} = \nabla . k_f \nabla \left[T_f(X,t)\right] \qquad X \in \Omega_f(t) \tag{4-2}$$

where C_f, k_f are the heat capacity and the thermal conductivity of the frozen tissue, respectively; $\Omega_f(t)$ denotes the frozen domain at time t; and $T_f(X,t)$ is the temperature of the frozen tissue.

Assuming that the density of tissue is the same and constant for both frozen and unfrozen phases, the temperature continuum and energy balance conditions on internal boundary of the moving interface for biological tissues, are as shown below:

$$T_f(X,t) = T_u(X,t) = T_m \qquad X \in \mathrm{T}_{m.i.} \tag{4-3}$$

$$k_f \frac{\partial T_f(X,t)}{\partial n} - k_u \frac{\partial T_u(X,t)}{\partial n} = Q_l V_n \qquad X \in \mathrm{T}_{m.i.} \tag{4-4}$$

where Q_l, T_m are the latent heat and freezing point of tissue, respectively ; n denotes the unit outward normal ; $T_{m.i.}$ is the moving boundary resulting from freezing or thawing and V_n is the normal velocity of the moving interface. Equations (4-3) , (4-4) are called the Stefan condition [61] and shows the discontinuity of the temperature gradient across the moving interface. The external boundary is divided into three sub-regions as shown in Figure 4-1 with different characteristics in which the temperature field is applied, i.e.

$$T(X,t) = const \quad \text{on } \Gamma_1 \text{ (Dirichlet type)} \tag{4-5}$$

$$k_i \frac{\partial T(X,t)}{\partial n} = 0 \quad \text{on } \Gamma_2 \text{ (Neumann type)} \tag{4-6}$$

$$k_i \frac{\partial T(X,t)}{\partial n} = -p_i T(X,t) + q_i \quad \text{on } \Gamma_3 \text{ (Cauchy type)} \tag{4-7}$$

where k_i is thermal conductivity of the i th phase, assuming $i = 1$ for the frozen and $i = 2$ for the unfrozen phase.

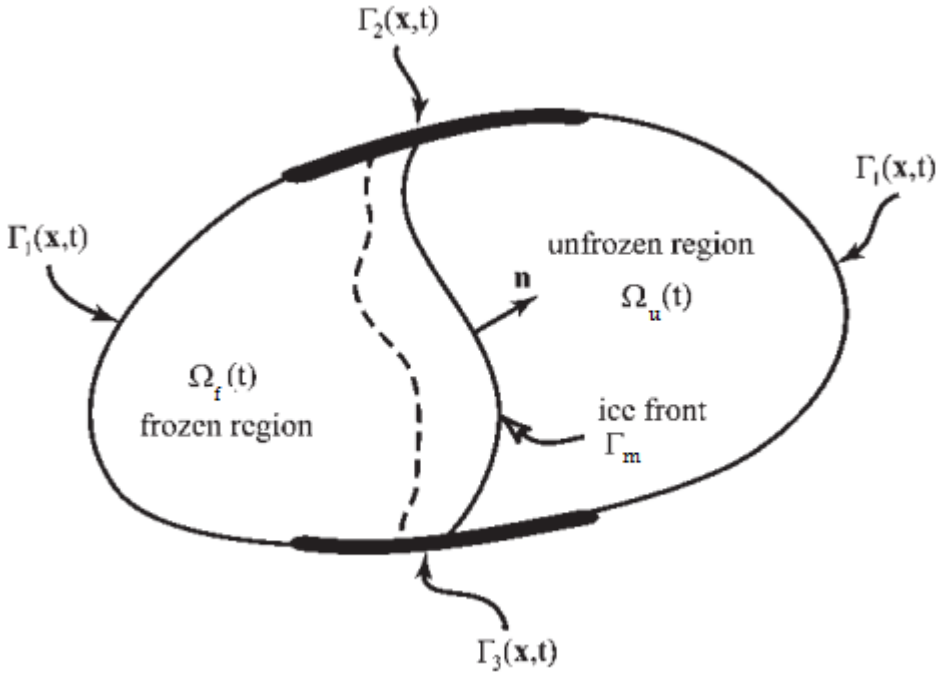

Figure 4-1 bioheat moving boundary and three different temperature fields generated [28]

Since Equations (4-1)-(4-4) are highly non-linear, the effective heat capacity method is applied to avoid complex iterations at discretizing the governing equations as proposed by [36]. The basics of this method lie in approximation of the latent heat over a small temperature range close to the freezing point. Using this strategy, the numerical solution can be carried out on a fixed grid throughout the calculation process, which is easy to implement.

Based on the above energy conservation model for a multicomponent phase-change system, a universal equation which can be applied to the frozen, partially frozen or unfrozen tissues can be derived [23]. So, the final uniform heat equation for biological tissue during freezing/thawing can be written as:

$$\widetilde{C}\,\frac{\partial T}{\partial t} = \nabla.\tilde{k}\nabla T - \widetilde{\omega}_b C_b T + \tilde{Q}_m + \widetilde{\omega}_b C_b T_a \qquad X \in \Omega \tag{4-8}$$

where $\widetilde{C}\,(T)$ is the effective heat capacity; $\tilde{k}(T)$ is the effective thermal conductivity; $\tilde{Q}_m$ is the effective metabolic heat generation; $\widetilde{\omega}_b(T)$ is the effective blood perfusion and they are formulated in different temperature bounds as follows:

$$\widetilde{C}\,(T) = \begin{cases} C_f & T < T_{ml} \\ \frac{Q_l}{(T_{mu}-T_{ml})} + \frac{C_f+C_u}{2} & T_{ml} \le T \le T_{mu} \\ C_u & T > T_{mu} \end{cases} \tag{4-9}$$

$$\widetilde{k}\,(T) = \begin{cases} k_f & T < T_{ml} \\ \frac{k_f+k_u}{2} & T_{ml} \le T \le T_{mu} \\ C_u & T > T_{mu} \end{cases} \tag{4-10}$$

$$\tilde{Q}_m(T) = \begin{cases} 0 & T < T_{ml} \\ 0 & T_{ml} \le T \le T_{mu} \\ Q_u & T > T_{mu} \end{cases} \tag{4-11}$$

$$\widetilde{\omega}_b(T) = \begin{cases} 0 & T < T_{ml} \\ 0 & T_{ml} \le T \le T_{mu} \\ \omega_b & T > T_{mu} \end{cases} \tag{4-12}$$

The value assigned to blood perfusion of tissue follows one of four possiblities described by [27] with the assumption that the frozen blood vessels can recover their functions immediately after thawing. Applying the explicit finite-difference formulation to Equation (4-8) and using Equation (4-13) to express the linear term $T(X,t)$ can discretize Equation (4-8) as presented in Equation (4-14).

$$T(X,t) = \beta T(X,t+\Delta t) + (1-\beta)T(X,t) \tag{4-13}$$

where β is a relaxation factor and $0 \le \beta \le 1$.

$$T(X,t+\Delta t) = \frac{1-W(1-\beta)\Delta t - m.Fo}{1+W\beta\Delta t}T(X,t) + \sum_{i=1}^{m/2}\frac{Fo}{1+W\beta\Delta t}T(X+\Delta X_i,t) + \sum_{i=1}^{m/2}\frac{Fo}{1+W\beta\Delta t}T(X-\Delta X_i,t) + \frac{(\tilde{Q}_m+\widetilde{\omega}_b C_b T_a)\Delta t}{1+W\beta\Delta t} \tag{4-14}$$

where Δt is the time increment, Fo $=\widetilde{k}\,.\Delta t/\widetilde{C}\,\Delta x^2$ is the Fourier number and W is defined as W$=\widetilde{\omega}_b C_b/\widetilde{C}$. Finally m can accept values 2, 4, or 6 corresponding to the cases of one, two and three dimensions respectively and ΔX is defined like this:

$$\Delta X_1 = (\Delta x, 0, 0) \quad \Delta X_2 = (0, \Delta y, 0) \quad \Delta X_3 = (0, 0, \Delta z)$$

4.3 Numerical values and discretization parameters

All the computations are done inside a large cube centered on the tumor as a pre-defined space for numeric computations in a 3D domain. This domain is prescribed in a cubic geometry with 7×7×7 cm in the x, y and z directions respectively, in which x denotes the anterior-posterior direction while y is along the lateral-medial direction and z is along the superior-inferior direction (see Figure 4-2). Only corresponding regions of organs located inside this cube are considered for heat

computation. Boundary conditions for this setup are described as follows:

$$-k\frac{\partial T}{\partial x} = h_f\left[T_f - T\right] \text{ at } x = 0 \qquad T = T_c \text{ at } x = 70\ mm \tag{4-15}$$

$$-k\frac{\partial T}{\partial y} = 0 \text{ at } y = 0 \qquad -k\frac{\partial T}{\partial y} = 0 \text{ at } y = 70mm \tag{4-16}$$

$$-k\frac{\partial T}{\partial z} = 0 \text{ at } z = 0 \qquad -k\frac{\partial T}{\partial z} = 0 \text{ at } z = 70mm \tag{4-17}$$

h_f is the convective heat transfer coefficient between the environment and the skin and T_c, T_f are respectively the temperatures of the body core and the surrounding air. Positions on the boundary directions y, z are not almost affected by the center domain as they are still inside the body but far from the needle tip and can be viewed as infinity for the heat or cold source.

In order to avoid any numerical instability, the space and time steps were limited by 1-W(1-β) Δt-m.Fo $\geq$ 0. In this thesis, the grid resolution is $\Delta x = \Delta y = \Delta z = 1$ mm and $\Delta t = 0.1$ s. Applying the boundary conditions at time $t+\Delta t$ and substituting the calculated results at the previous time t, the unknown T at time $t+\Delta t$ can be solved from Equation (4-14).

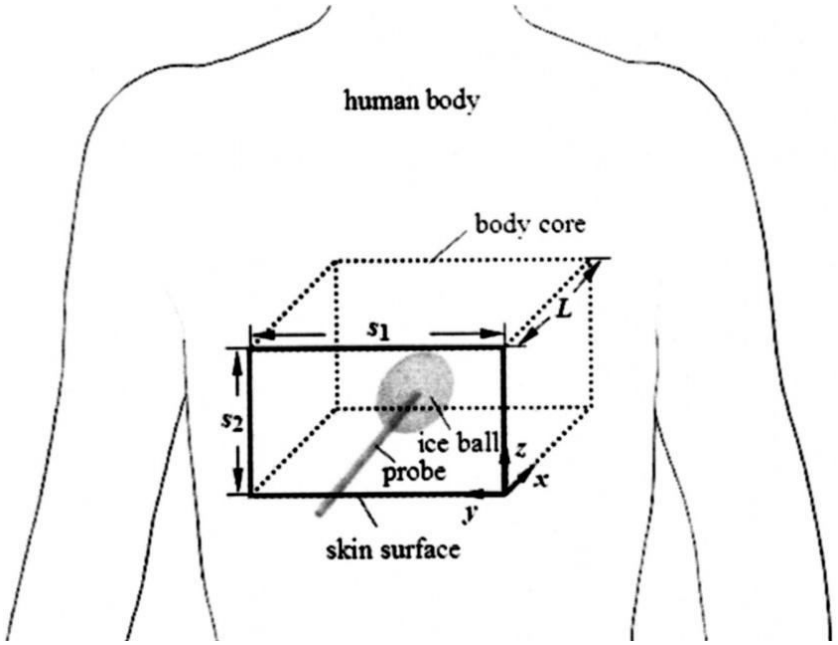

Figure 4-2 Schematic of 3D geometry for one probe case [30]

The boundary conditions at the probe surface are prescribed respectively according to probe tip and probe shank as: T=−196 °C at probe tip; $\partial T/\partial n$=0 at probe shank. The initial temperature in tissue is simplified as $T0$=37. Other values for the numerical computation were found in the literature and are shown in Table 1 [30].

In the first place a mask of all the structures involved in the heat propagation like tumor, liver, needle tip and vessels is required with a similar coordinate system and resolution. This is due to the nature of finite difference formation by browsing all pixels of large cube surrounding the tumor center of gravity to compute heat propagation. The mask of some of these structures is already available in the dataset like tumor, liver and vessels but voxelizing needle tip cylinder cause quantification error depending on the voxel size. This process is shown for the needle tip in Figure 4-3 (a).

A similar phenomenon will happen while converting voxels to meshes for other organs. This will cause an error by smoothing the edges of surface made by marching cubes method and illustrated in Figure 4-3 (b). This error does not affect the computations but leads to an imperfect visualization of the iceballs and organs.

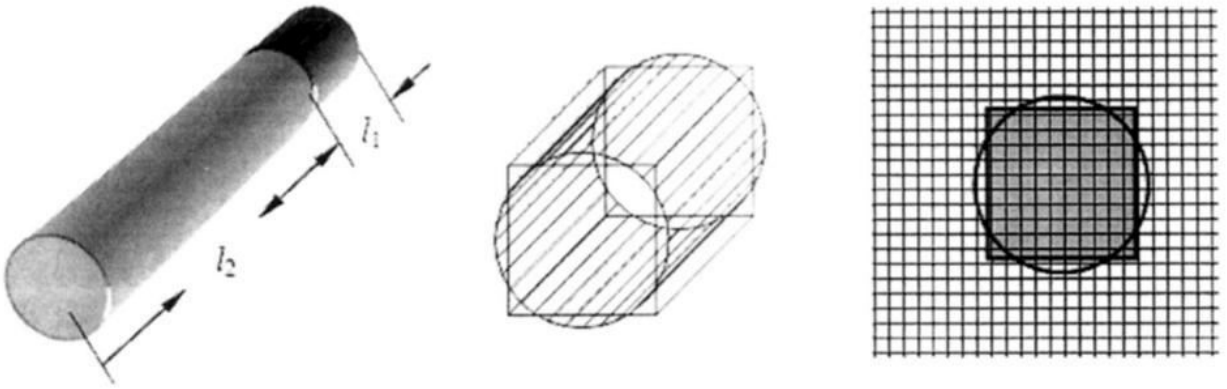

a)Needle shaft and needle tip are visible on the left then 3D and cross sectional view of the quantified version of the needle tip is shown on the right (Deng and Liu 2004)

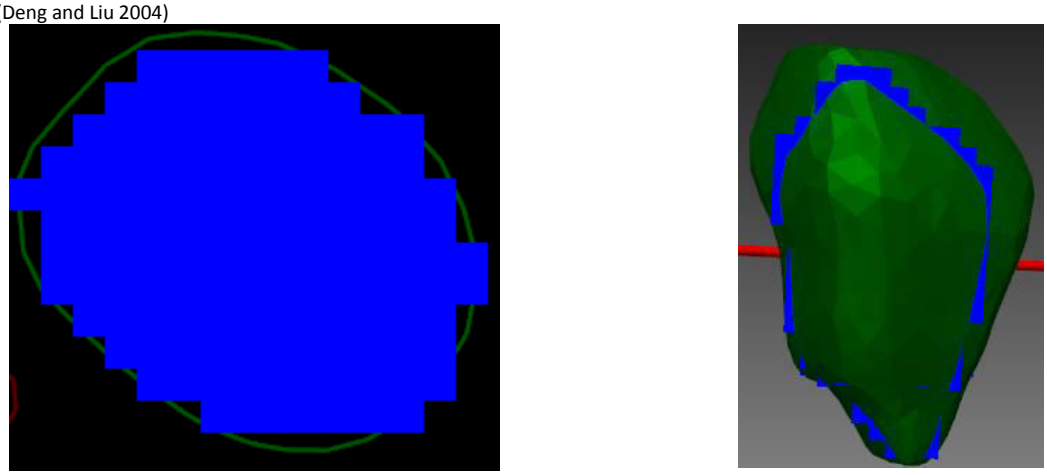

b)Left image shows an axial tumor mask and its reconstructed mesh. On the right a 3D image of the tumor mesh and a sagittal slice of its mask is visible

Figure 4-3 quantification error shown for the needle tip on the top and for the tumor mesh reconstruction on the bottom

Other parameters for our simulation setup are described below:

1. In order to consider the convective effect of vessels, they are considered as fixed sources of heat at 37°C.

2. The shape of needle tip has been designed to fit IceSeed cryoprobe from Galil Medical[4]. The length of the needle tip is modeled with precisely 20 mm, but for the diameter 2 mm is used instead of 1.5 mm in order to fit the resolution of our simulation cube which is 1 mm.

3. The simulation procedure imitates a standard cryoablation pattern that consists of two 10 minutes freezing intervals and one 5 minutes thawing step in between, which is used in clinical rou-

[4] www.galilmedical.com/cryoablation-products/needles/

tine and congruent with the needle manufacturer calibration data in a tissue-like gel.

Table 1 Typical thermophysical properties of soft biological tissues [30]

	Unit	Value
Heat capacity of the frozen tissue	$MJ/m^3\,°C$	1.8
Heat capacity of the unfrozen tissue	$MJ/m^3\,°C$	3.6
Heat capacity of the blood	$MJ/m^3\,°C$	3.6
Thermal conductivity of the frozen tissue	$W/m\,°C$	0.5
Thermal conductivity of the unfrozen tissue	$W/m\,°C$	2
Latent heat	MJ/m^3	250
Artery blood temperature	°C	37
Body core temperature	°C	37
Lower phase-transition temperature	°C	−8
Upper phase-transition temperature	°C	−1
Blood perfusion of normal tissue	ml/s/ml	0.0005
Blood perfusion of tumor tissue	ml/s/ml	0.002
Metabolic rate of normal tissue	W/m^3	4,200
Metabolic rate of tumor tissue	W/m^3	42,000

4.4 Results

In this section we demonstrate the results of our simulations in different contexts and conditions of surrounding structures. We compared the similarity between two kinds of meshes: the computed 3D isotherm surfaces and the segmented iceball as a reference mesh. For mesh comparison purposes we used two geometric methods called Hausdorff distance and Dice coefficient. Moreover, 3D meshes and their corresponding 2D axial, sagittal and coronal slices are shown for a better comparison.

The Hausdorff distance [62] is a method of geometric difference computation between two 3D models which is quite common in mesh processing and is defined as below:

$$d_H(X,Y) = max\{\sup_{x\in X}\inf_{y\in Y} d(x,y), \sup_{y\in Y}\inf_{x\in X} d(x,y)\} \tag{4-18}$$

In this equation X, Y represent two meshes and $d(x,y)$ is the distance between two corresponding points. Starting by a point from mesh X, the algorithm searches the closest point to mesh Y and continues this process for all points on mesh X then it returns the maximum distance computed so far. As this is not a symmetric operation, so Equation (4-18) considers both sides.

Another common criterion for comparing two meshes is the Dice coefficient [63]. It can be viewed as a similarity measure over two meshes which defined as:

$$s = \frac{2|X\cap Y|}{|X|+|Y|} \tag{4-19}$$

In order to obtain this coefficient, one needs to pre-compute several Boolean operations between the two meshes. Thus $|X\cap Y|$ is the volume overlapping and $|X| + |Y|$ represents sum of the volumes for the two meshes. Dice coefficient is 1 if two meshes are fitting each other completely and it

is 0 when there is no intersection.

We first simulated a standard cryoablation procedure with a single cryoprobe without any large vessels in the vicinity. The different simulated isotherm surfaces were compared with their corresponding theoretical ellipsoids proposed by the manufacturer Galil Medical as illustrated in Figure 1-4. Figure 4-4 shows different simulated isotherm surfaces:.0°C, -20°C and -40°C in blue, red and green respectively, along with the theoretical shape of the 0°C surface in yellow. Dice coefficient for the comparison of the 0°C isosurface is 0.96, which represents a high similarity. The similarity is 0.91 for -20°C isosurface and 0.81 for -40°C isosurface. Lower numbers in smaller isosurfaces are due to their smaller volume: a slight difference has a bigger influence on the similarity. Another source of discrepancy comes from the resolution of the finite difference network which in our case was 1 mm.

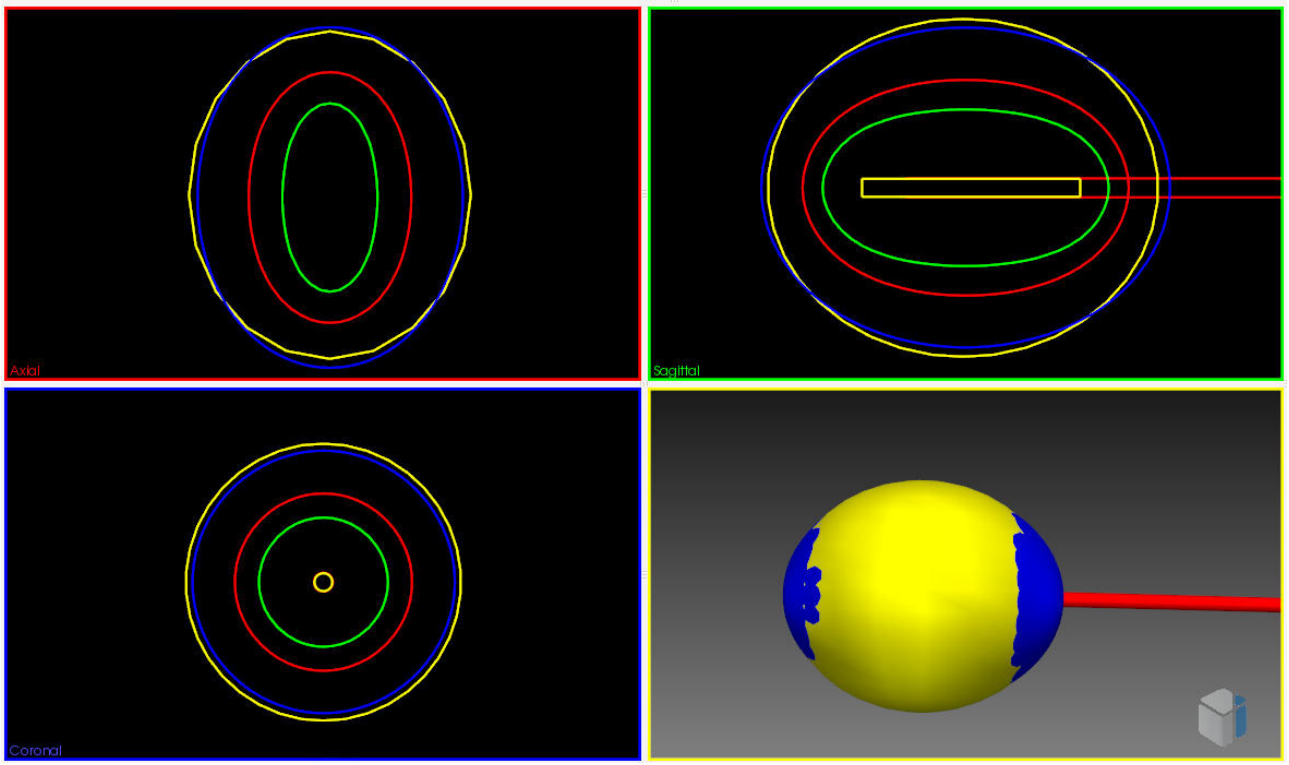

Figure 4-4 Simulated 0 °C iceball in blue is compared to its corresponding iso-therm in yellow reported by the manufacturer

The computation time for a standard cryoablation procedure is 50 seconds for the used resolution and dimensions. It is computed on a Core-i7 machine with 16 GB of memory. It is important to underline that this computational time is not changed when simulating several needles or considering the vessels and is only affected by the resolution and dimension of the discretized space around the tip, in our case 7x7x7 cm.

A similar procedure is done for two needles in order to show synergic effect of combined needles on the shape of ablation zone [11]. The resulting iceball is larger while having smoother edges comparing to separate ellipsoids. This effect is already investigated in the work of Talbot et al. [33] for cryoablation needles and Figure 4-5 shows this effect in 3D and 2D images for two needles in our software.

In a second step, we simulated the iceball produced by a single cryoprobe close to a large vessel, to visualize the influence of its heat-sink effect on the formation of the iceball. The right part of Figure 4-6 (a) shows a 3D model of the three isotherm surfaces not approaching vessels. On the left part of the figure, the same isosurfaces show deformations caused by the proximity of a vessel.

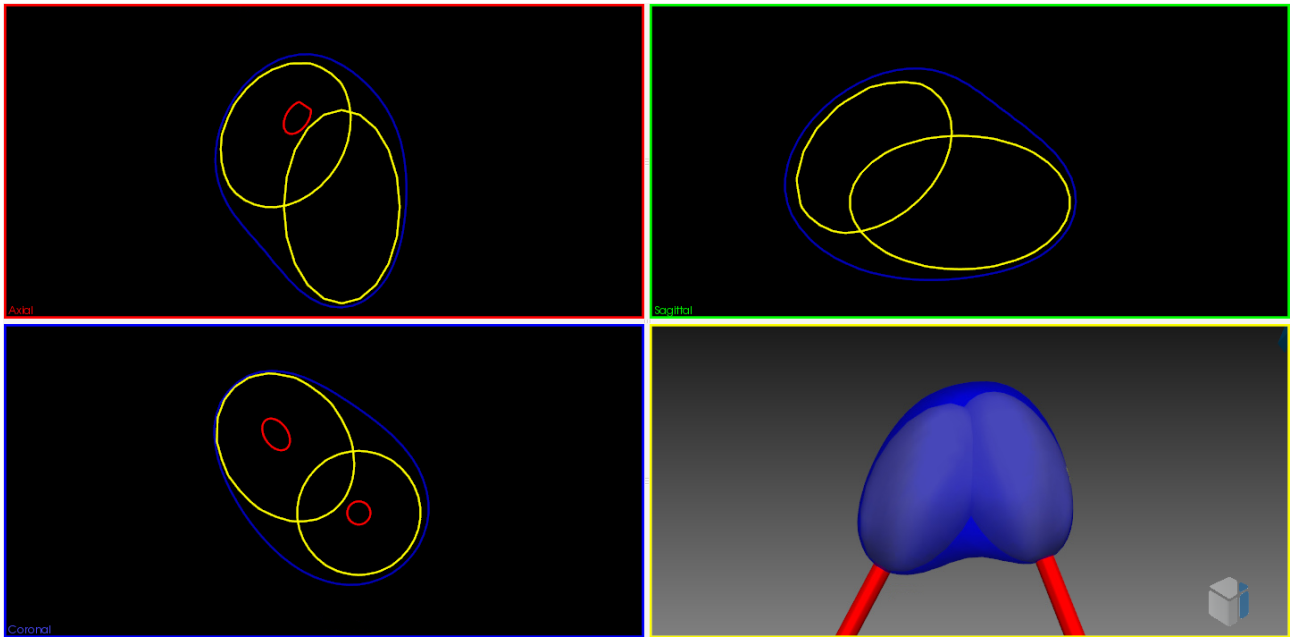

Figure 4-5 Synergic effect of two needles on the simulated iceball comparing to separate ellipsoids

In Figure 4-6 (b) the percentages of volume changes are shown for three different values of the distance from the cryoprobe tip to the vessel. As expected, we can see that the closer the tip gets to the vessel, the more the three iceballs are deformed. The 0°C isosurface, which is the larger and the more external one, is experiencing the largest deformation. This graph highlights the importance of the effect of vessels on the formation of iceballs, which has a direct impact on the chance of recurrence due to a possible over-estimation of the expected iceball.

This phenomenon is also illustrated in our patient data. On the high resolution MRI images, we superimposed a 3D model of cryoprobe in an arbitrary position close to the vessel in order to show 2D views of this effect for an easier visualization of deformations on slices. We computed and displayed the three simulated isotherm surfaces and the theoretical reference ellipsoids proposed by the needle manufacturer, and compared them. Figure 4-7 shows sequential axial slices and the shapes.

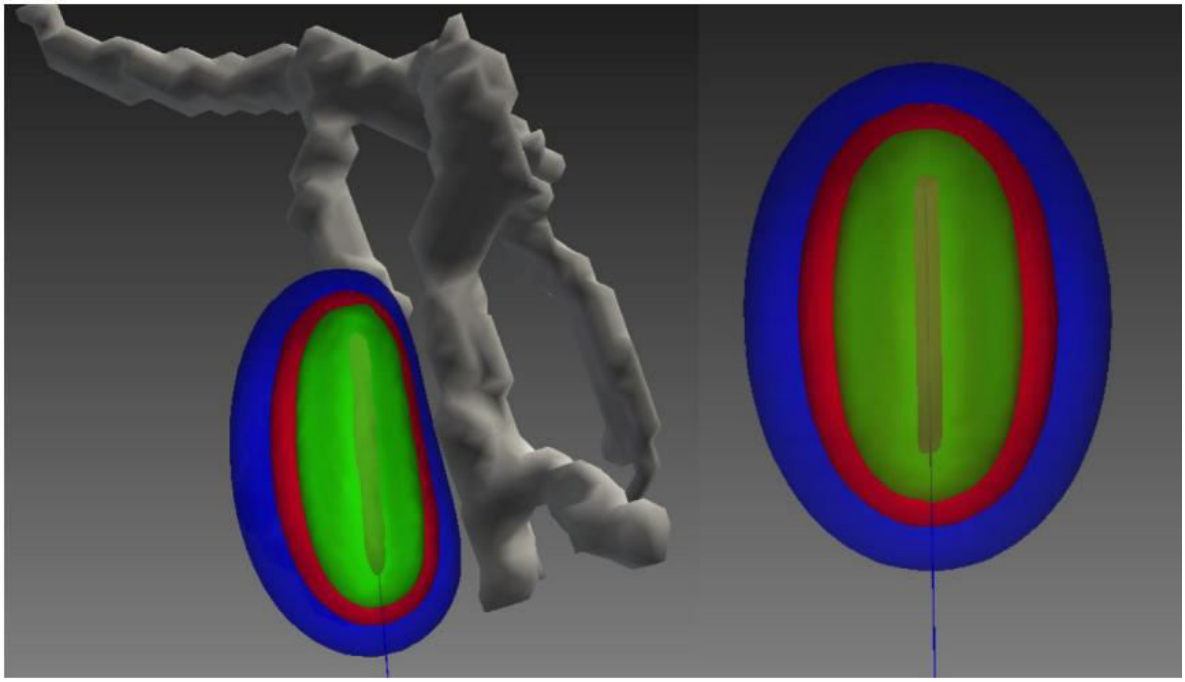

a) Iceball deformation due to the vicinity vessel vs no deformation

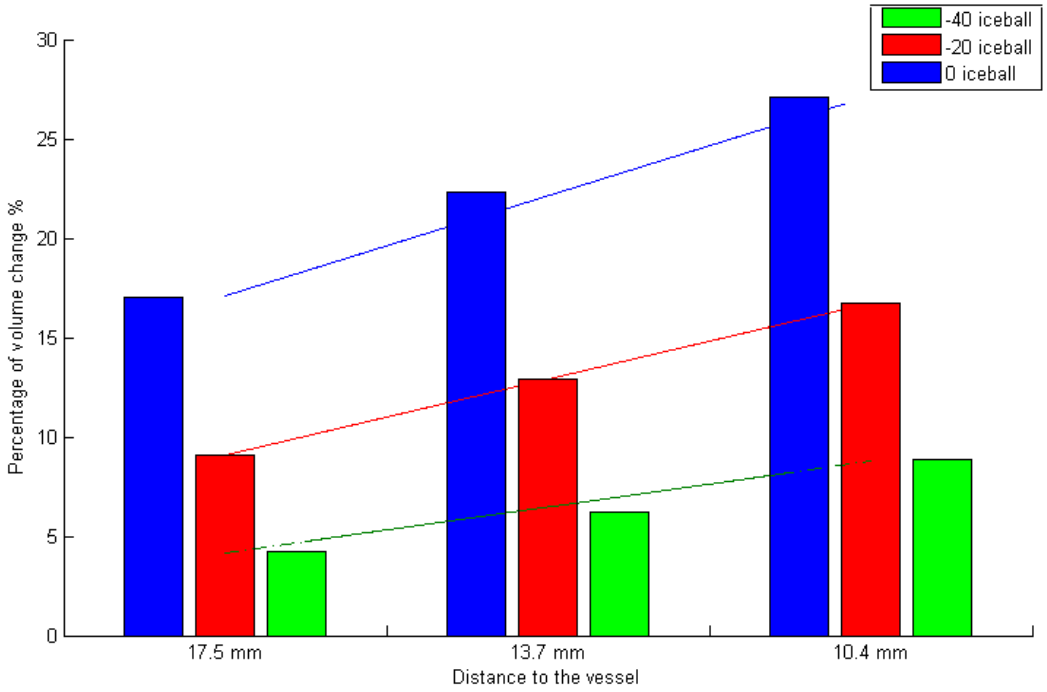

b) Percentage of volume change for 3 different iceballs vs distance to the vessel

Figure 4-6 iceball deformation due to the vicinity vessels

In order to compare the simulation rigorously and verify the situation of several interacting needles, we compared both the theoretical ellipsoids and our simulations with ground truth which in our case was the segmented iceballs from intra-operative images.

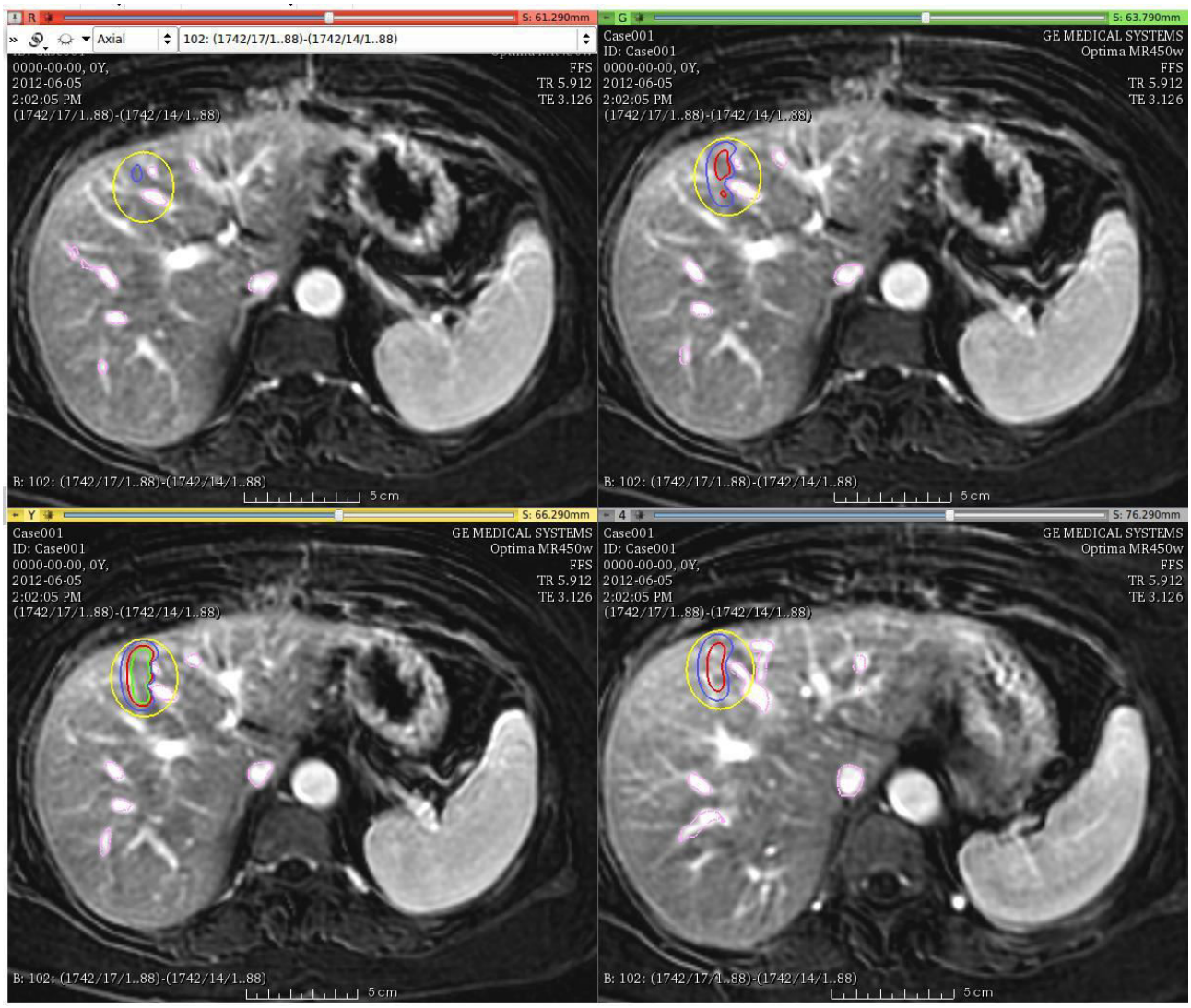

Figure 4-7 Sequential axial slices of iceballs encountering vessels. Simplified ellipsoid refers is shown in yellow and 0, -20 and -40 °C iceballs from blue to green. Vessels are in pink.

4.5 Validation

In this part simulated isotherm surfaces for one and two needles are compared with their corresponding iceballs segmented from the patient intra-operative images. In order to perform this task, the needles tips were also extracted from intra-operative images and the simulation was done based on similar needle placements (see Figure 4-8).

Figure 4-9 shows a snapshot of our TrajectoryPlanning tool illustrating the simulation results based on a single segmented needle and its iceball. The 2D slices shows a good fit between simulated and segmented iceballs while preserving large vessels and showing the correct estimation of deformation due to the vessels. In all slices ellipsoid has an overlap with vessels and gives a bigger estimation of the necrosis zone. In the case of 2 needles in Figure 4-11 one can see the superiority of simulated iceball over the theoretical ellipsoids. It shows a better fit to the segmented iceball as it counts for the interaction between the two probes, a more homogeneous shape, stays far from vessels, and does not over-estimate the necrosis compared to the two theoretical ellipsoids.

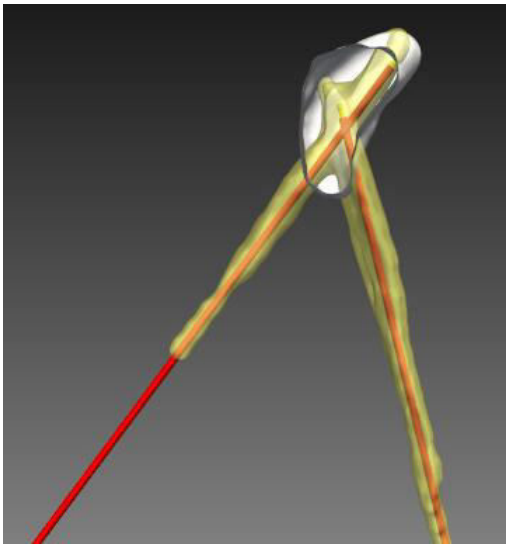

Figure 4-8 In this image segmented iceball-2 is shown in white besides segmented cryoprobes in light yellow. The simulation cryoprobes are shown as red trajectories within segmented cryoprobes.

In order to analyze more quantitatively the amount of improvement by the simulation we have used the Hausdorff distance metric as defined in section 4.3, which can be visualized in ure 4-10. Part (a) shows the comparison between the theoretical ellipsoid and the segmented iceball and part (b) shows the comparison between the simulated iceball and the segmented iceball.

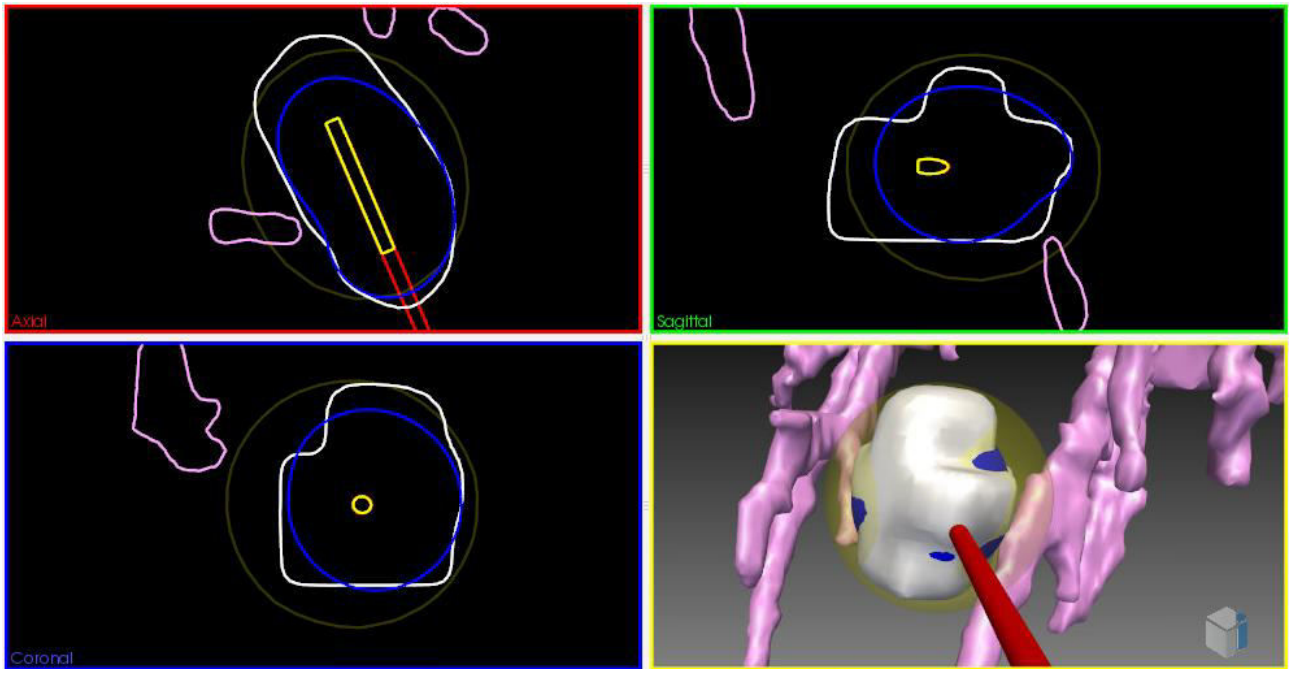

Figure 4-9 Simulated iceball in blue versus segmented iceball-1 in white for a 10 minute freezing cycle. Theoretical ellipsoid is shown in yellow. Vessels are in pink.

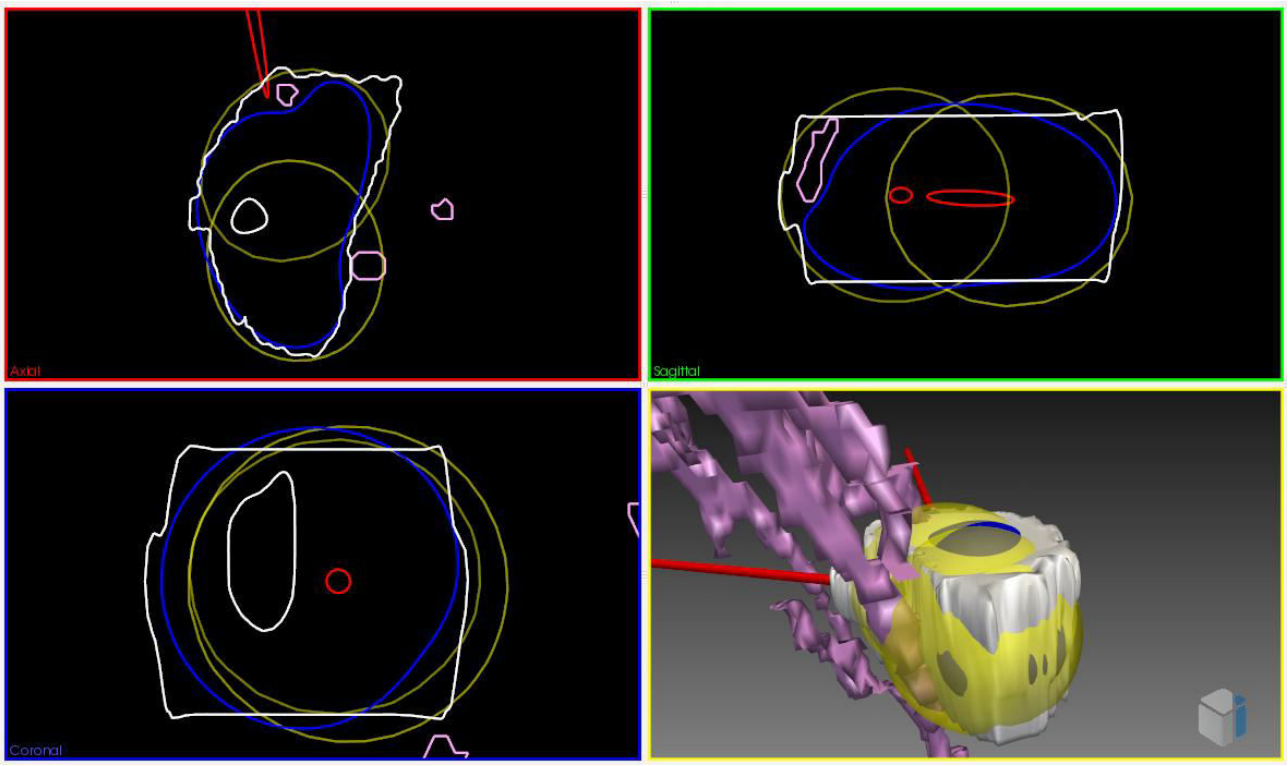

Figure 4-11 Simulated iceball in blue versus segmented iceball-2 in white for a 10 minute freezing cycle. Theoretical ellipsoids are shown in yellow and vessels in pink.

A boxplot comparison including statistical information like average, maximum, minimum, 25th and 75th percentile of values for all vertices of these meshes is represented in Figure 4-12 which shows an improvement in average distance of correspondent vertices for the case of simulation ice-ball.

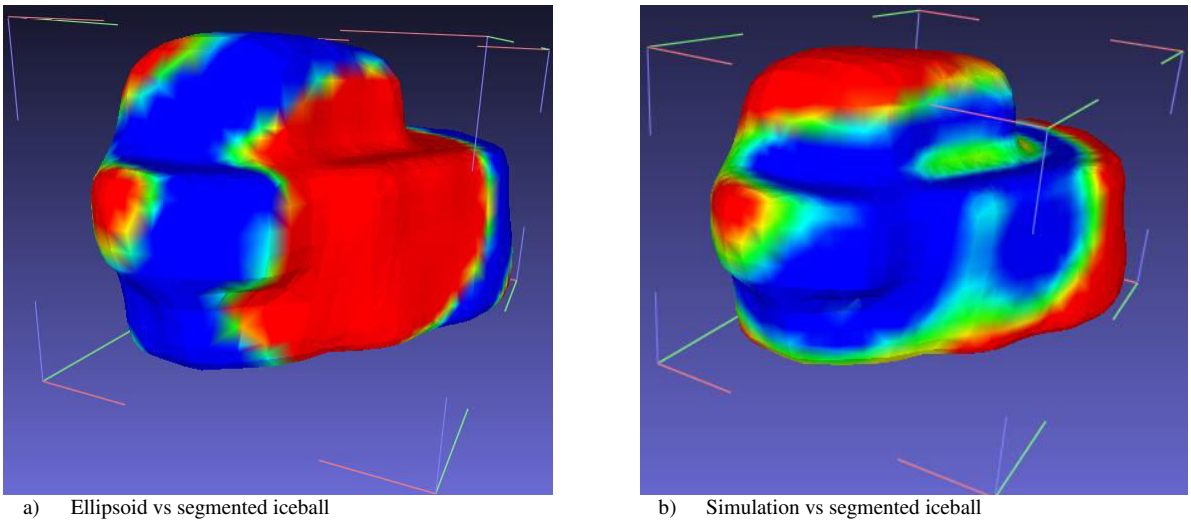

a) Ellipsoid vs segmented iceball b) Simulation vs segmented iceball

Figure 4-10 Hausdorff distance computed for each vertex of the segmented iceball-1 mesh. Blue color indicates a low distance while large distances are in red

A similar comparison was done for the two-needle case that also shows an improvement of the Hausdorff distance for the simulation iceball but less prominent (see Figure 4-13 and Figure 4-14). We can also describe these improvements descriptively using Figure 4-10 and Figure 4-13. As it is visible in the images, the Hausdorff distance is reduced for simulated iceballs on the sides of the mesh (blue color represents lower distances between two meshes) which shows they could better fit into the shape of segmented iceball while theoretical ellipsoids have better results on top and bottom planes which is due to their bigger sizes. In the presence of vessels, output of simulated iceball is smaller than theoretical ellipsoids. Due to low number of slices for segmenting the intra-operative iceball, its shape is more accurate in axial plane while in sagittal and coronal axis it is a rough approximation.

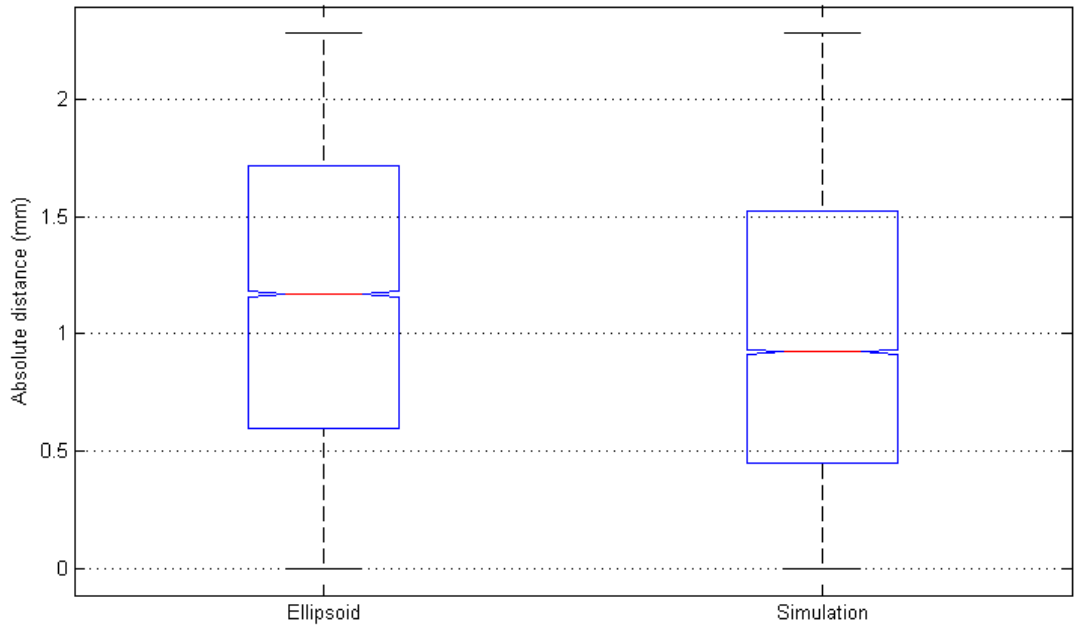

Figure 4-12 Hausdorff distance for total vertices is improved by the simulation. This is visible due to statistical parameters of the boxplot

While the Hausdorff distance metric compares more or less the shape of two meshes, we are also interested in the overlapping or difference of volumes which analyze the problem from another point of view. In order to do this we performed Boolean operations like intersection, difference and union which are shown for the case 1 in Figure 4-15. Using these volume comparison values we have computed the similarity coefficients as discussed in Section 4.4 for case 1 and 2 and it is presented in Table 2. For example in case 1 the value of similarity (Dice coefficient) while comparing theoretical ellipsoids and segmented iceball is 0.723 and this value when comparing simulated iceball with segmented iceball is 0.764. This shows an increase of intersected volume and improves the similarity of simulation iceball in contrast to the case of using simple ellipsoids. As Dice coefficient focuses on the similarities, by looking into Figure 4-15 on the second row, it is visible that the volume of difference between two meshes is also reduced which represents a better fit of two meshes.

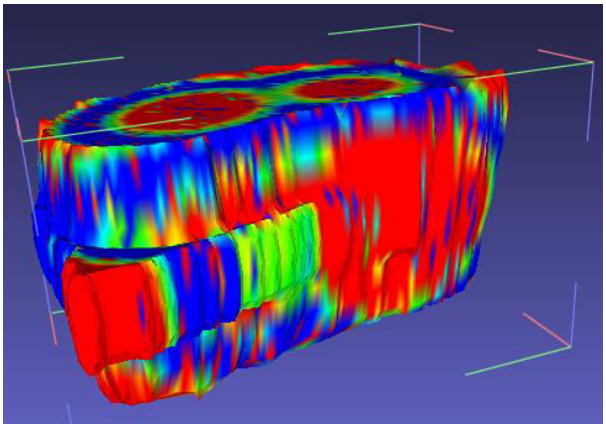

a) Ellipsoid vs segmented iceball

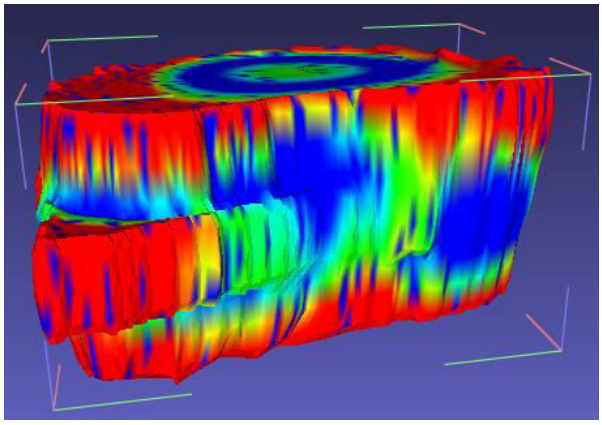

b) Simulation vs segmented iceball

Figure 4-13 Hausdorff distance computed for each vertex of the segmented iceball-2 mesh. Blue represents low distances while red is used for large distances

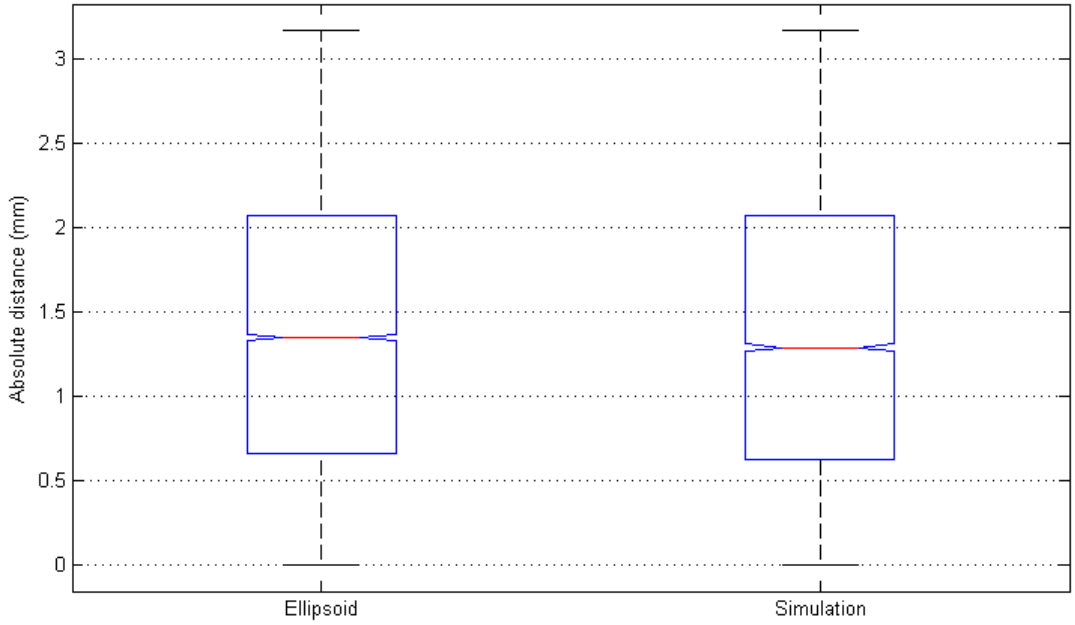

Figure 4-14 Hausdorff distance improvement for total vertices in iceball-2 is less visible and only the average of boxplot is reduced.

Table 2 Similarity coefficient for cases 1 and 2 for ellipsoids and simulated iceballs due to the segmented iceballs

Similarity coefficient	**Ellipsoid vs segmented iceball**	**Simulated vs segmented iceball**
Case 1	0.723	0.764
Case 2	0.814	0.831

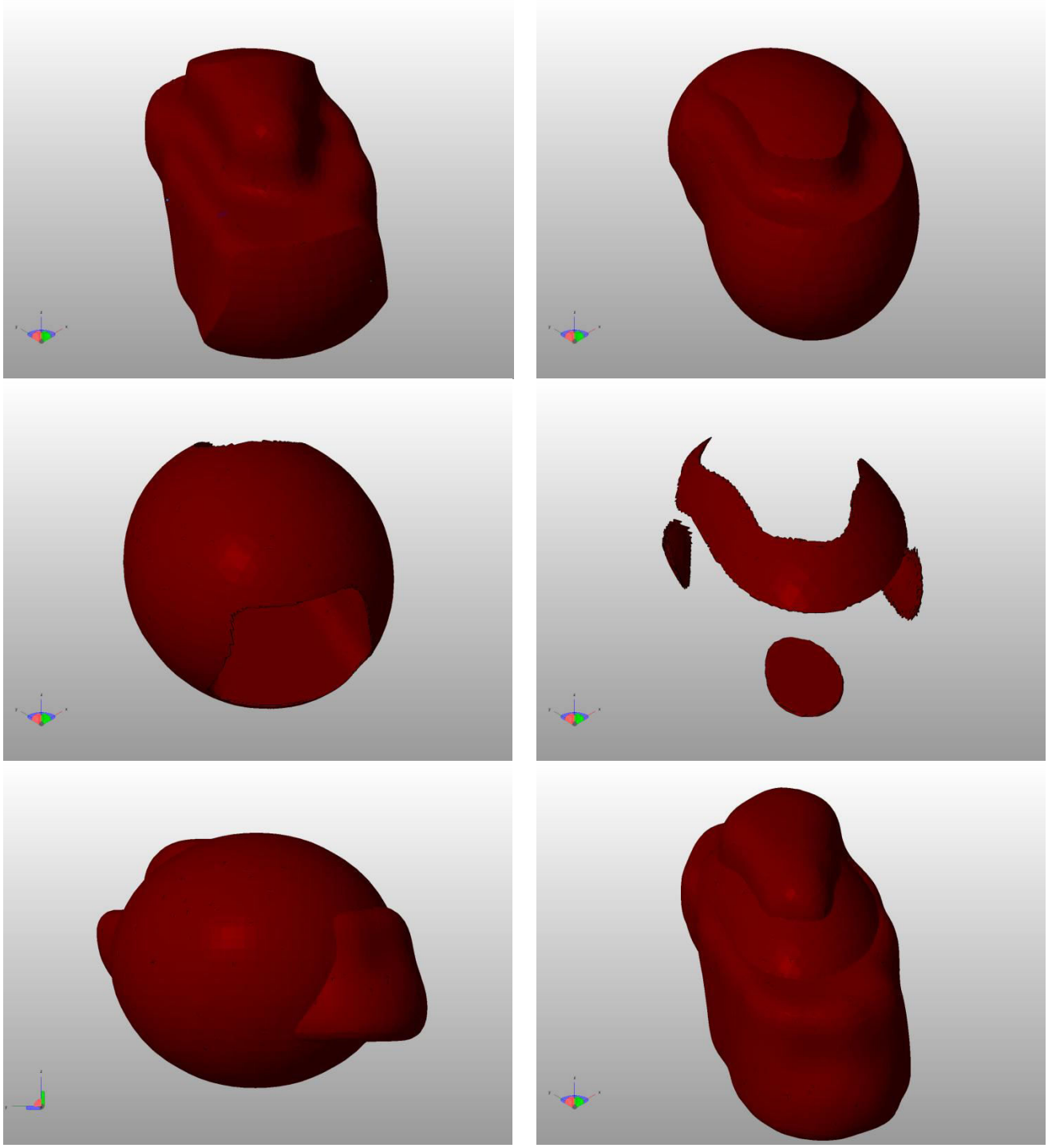

Figure 4-15 Boolean operations for comparing ellipsoid in left and simulation in right. For both of them the segmented iceball was used as reference mesh. First row is computed for intersection, second row is difference and last row is the union of each mesh with the reference mesh.

4.6 Conclusion and discussion

In this chapter we have simulated the heat propagation in the tissue while considering convective effect of large vessels. The results were compared to the proposed ellipsoids from the needle manufacturers which has a high correlation with our simulated iceballs in a tissue without vicinity vessels. They also showed the important role of the vessels on the deformation of final iceballs.

The computational time required by the solver depends only on solution space dimensions. This is interesting for us, as the ultimate purpose of this thesis is to integrate the simulations in the planning phase while studying different number of cryoprobes. Therefore the computational time for processing the bioheat simulations inside the automatic planner is independent from the number of cryoprobes.

In order to assess the results we have compared the simulated isotherm surfaces with segmented iceballs using different methods. However visualization of 2D slices mainly illustrated the improvement by a better fit of simulated iceball into the segmented iceball, some quantitative metrics like Hausdorff distance, Dice coefficient for similarity measurement and volume differences were also utilized. Each of these methods highlights the improvement over using simple ellipsoids based on its own perspective.

However, let us note that obtaining exploitable intra-operative images for this validation was challenging due to the number of required features. A dataset with pre- and intraoperative images was needed, pre-operative images should have been taken with contrast agent to have visible vessels, and intra-operative images should show completely the iceballs and cryoprobe location. We needed to know the type of the cryoprobe and the procedure of cryosurgery which was performed. In the data we could obtain, intra-operative images had very low number of slices, between 3-5, with large slice thickness which caused some false positive or false negative, introduced errors and thus affected the results in two ways. Firstly, it was hard to have a good alignment between pre- and intraoperative images, and secondly due to the few number of available slices it was not possible to have a precise segmented iceball, which had sharp edges and augmented sizes contrasting with our simulated homogenous and smooth iceballs. This can potentially decreases the amount of improvement in our simulation results. Quantifying this error while there is no interaction with the vessel only depends on the interpolation error of the iceball with 5mm slice thickness but it is more complex when the shape of the iceball is deformed due to the proximity vessels.

However some degree of improvement was seen in the validation part but it will be essential to perform more comparisons on intra-operative images with different conditions of proximity to vessels or different tumor sizes in further works. In order to have fair comparisons, it will be necessary to have more slices with thinner slice thickness for a better segmentation of the iceballs.

Chapter 5. Geometric constraints

5.1 Overview

In this chapter we describe the methods and algorithms we used to translate the planning problem into geometrical and numerical expressions to solve. In section 5.2 the structure of our framework is explained, and a descriptive implementation of the constraints is presented. Then one of the rules mentioned in section 1.3.1 is translated as an example. Besides our lexical formulation of the rules, we also describe some geometric algorithms to compute the operations required in different stages of the planning process. These algorithms and their variations are discussed in section 5.3 and a short conclusion follows.

5.2 Constraints structure

Over the past decade, our research group has developed an automatic preoperative trajectory planning tool under the form of a geometric constraints solver in C++, based on the MITK software platform, and using ITK and VTK libraries. An implementation of the planning tool in a generic way was very important as our group, convinced that many surgical planning problems involving the placement of straight surgical tools in the body were having similar issues, wanted to build a solver able to plan different kinds of interventions without writing specific code for each.

The solver receives images and segmented anatomical structures along with the intervention rules as input data. The rules are written in a specifically defined meta-language, and saved in a separate XML file which is loaded when the software is run. An XML file contains rules specific to a particular type of intervention. If an extra constraint is needed, it just has to be written in this file.

For cryoablation, a solution is defined by the position of several needles in the 3D space. The placement of one needle can be represented indifferently either by a point (i.e. the tip of the needle) and direction or by two points (tip and insertion point). The rules written in the XML file constrain the placement of the needles or express preferences of placements.

Using the existing meta-language structure, the rules mentioned in section 1.3.1 and their corresponding cost function are translated as geometric constraints. For such a translation we write constraints into terms (see Table 3), that can also be represented as trees of nodes (see Figure 5-1). Each node contains either an operator, known data, constant, or variable, based on an already defined geometric universe. Constants and known data in this universe can be selected among the usual types (e.g. *integers, real numbers, Booleans*) or composed types such as *point, shape, tool*, or *solution*. Among the available operators, we have: usual basic operators such as *plus, minus, multiply, divide, and, or*, as well as complex operators as for instance *distmin* (minimal distance between

two entities), *angle* (angle between two entities) or *volume* (volume of a shape). Lastly, the variables represent either the candidate trajectory itself (*toolTrajectory*) or some entities linked to the candidate trajectory such as *toolAblation* (the estimated ablated shape corresponding to the candidate trajectory) or *toolInsertionPoint* (the insertion point of the candidate trajectory). In order to add an extra constraint in the XML file, the necessary operators must have already been defined in the software. They are linked with data which need to be loaded in the software (such as organs shapes), variables and constants to form a new term. These terms are solved using a depth-first approach.

One of the goals of this PhD was to extend the existing solver to handle multiple needles simultaneously. Therefore, some structural modifications were required in the classes and their members, new operators and variables needed to be added in the geometric universe and also certain classes with new methods needed to be developed.

As an example, let us analyze Rule *risk_organX*. This rule aims at minimizing the risk of intersecting any of simultaneously used needles with the organ "organX" (for instance vessels) we would like to avoid. It is translated into a soft geometric constraint expressing that the minimal distance between the trajectory of each needle and the organ has to be maximized. It is computed by minimizing a numerical cost function $f_{risk\_organX} : R^{5*N} \rightarrow [0,1]$ in which N represents number of needles applied, and each needle having 5 degrees of freedom. The cost function is normalized in a way that the resulting values are between 0 and 1, in order to obtain comparable magnitudes to the cost functions of the other rules before combining them. Without this normalization, a rough combination of these functions would be meaningless.

When dealing with only one needle, the cost function simply tended to zero if the minimal distance from the needle to the organ was above 5mm, and to 1 if it was close to zero. With multiple needles, this function had to be modified to account for the distance between each needle and the organ: if the minimal distance for all needles is above 5mm then this cost function returns 0, which means there is no risk to that organ, and if there is at least one needle close to the organ it tends to 1. This leaded us to define a new operator *vectordistmin*, which consists in computing the distance between each needle of the set and a given organ and returning the minimum distance among them. A new variable also needed to be introduced, named *multipleNeedles*, expressing a set of new candidate trajectories having 5*N degrees of freedom.

Equation (5-1) specializes the rule by defining the avoidance of vessels. The associated mathematical cost function to minimize is $f_{risk\_vessels}(X)$ in which X represents the set of needles. In order to express this function as a recognizable constraint for our solver, we used our meta-language and wrote a term describing this function. This term uses existing operators (*divide, max, minus*) and constant data (organ mesh coming from the images, integers 5 and 0) defined in the solver. It also uses the new operator *vectordistmin* and variable *multipleNeedles*. The term in XML syntax is shown in Table 3. The corresponding tree is developed in Figure 5-1. In the solver, we use this tree structure to represent the constraints. If a data or variable node is used in more than one constraint, it exists only once and doesn't have to be re-evaluated several times.

$$f_{risk\_vessels}(X) = Max(\frac{5-vectordismin(X,vessels)}{5}, 0) \quad (5\text{-}1)$$

Table 3 XML formulation of the rule risk_vessel

```
<soft_constraint name="risk_vessels" label="sc_risk" minValue="0" maxValue="1">
        max( divide( minus( 5 ,  vectordistmin (multipleNeedles, vessels) ), 5 ), 0 )
</soft_constraint>
```

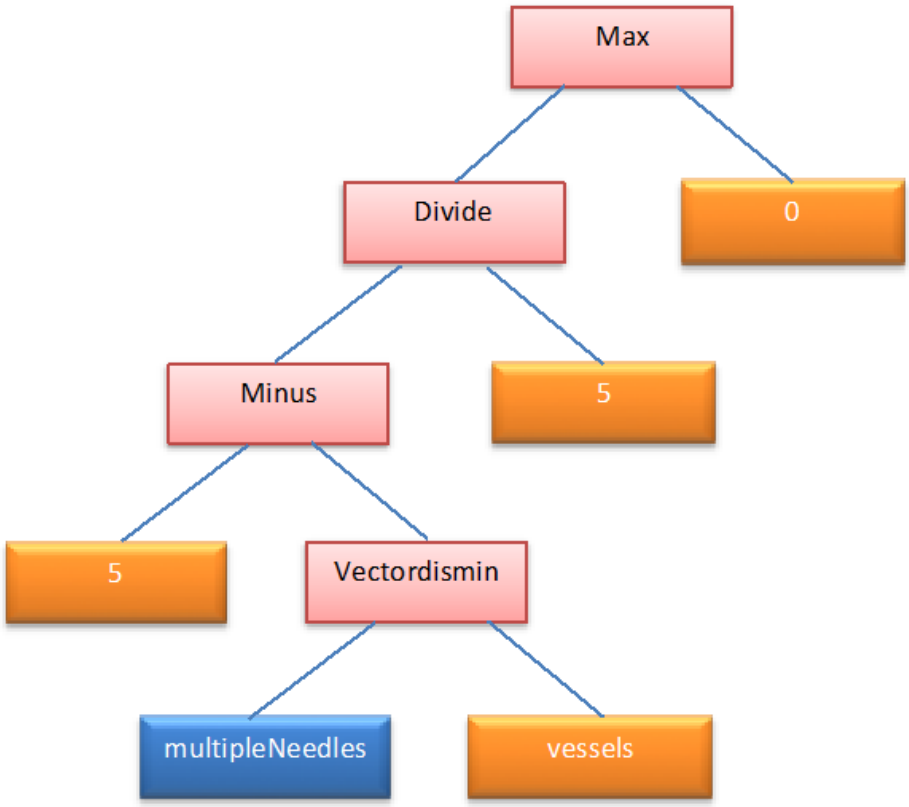

Figure 5-1 Tree representation of the constraint risk_vessels expressing the maximization of distance to vessels: operators are in red, given constant data are in orange, and the variable is in blue.

Another important constraint is to minimize the damage to the healthy tissue around the targeted tumor. Its cost function called f_{volume} is shown in Equation (5-2) and described as XML format in Table 4. In this constraint, the volume operator is used to compute the volume of the ablated region. This operator can take different types of input data in order to compute the volume of different types of shapes, such as masks (like the tumor), meshes (like the simulated iceball), and one or multiple ellipsoids. In order to discriminate these shapes, except existing variables like *toolAblation*, two other variables called *ellipsoidSet* and *iceballVolume* are also defined. These new variables determine type of the ablation region used in the planning step and *toolAblation* is used for computing tumor volum. All these names obey our naming conventions in the plugin.

$$f_{volume} = \frac{volume(toolAblation) - volume(tumor)}{5 * volume(tumor)} \quad (5\text{-}2)$$

ellipsoidSet is a simplified geometric interpretation of the ablation zone based on multiple independent ellipsoids and *iceballVolume* refers to an ablation zone computed using simulation of heat

propagation for several needles. Constraint f_{volume} is normalized between zero and one based on the tumor volume as showed in Equation (5-2). In this normalization it is supposed that the ablated volume would never be more than 5 times the tumor volume.

Table 4 XML formulation of the volume constraint

```
<soft_constraint name="volume" label="sc_vol" minValue="0" maxValue="1">
        divide( minus( volume( toolAblation), volume( tumor ) ), mult( 5, volume( tumor ) ) )
</soft_constraint>
```

In similar ways, all the constraints we detailed in Section 1.3.1 were written in XML syntax using our operators, variables and data. One last soft constraint is added, representing the aggregative constraint which combines the previously defined constraints with some chosen weighting factors, and corresponds to the aggregative cost function f_{final}. As presented in Equation (5-3) each inner cost function f_i is multiplied by a weighting factor w_i that can be controlled while the program is running. This way, based on the surgeon's needs or preferences, these values can be changed and the result is updated on the fly, without the need to modify and recompile the code.

In the rest of the manuscript describing our experiments, we will consider only 3 soft constraints: the volume of damaged healthy tissue to minimize, and the distance to ribs and vessels to maximize. Then the final cost function is:

$$f_{final}(X) = w_{volume}f_{volume}(X) + w_{risk\_ribs}f_{risk\_ribs}(X) + w_{risk\_vessels}f_{risk\_vessels}(X) \quad (5\text{-}3)$$

5.3 Required algorithms

5.3.1 Volume optimization

Ellipsoids

Among all surgical rules that our solver aims at optimizing, full tumor coverage is a crucial rule for a successful operation. It is then essential to check this condition and withdraw placement combinations that do not fulfill it. The computation of tumor coverage by the expected iceball is performed using different methods for the cases of ellipsoids and simulated isotherm surfaces. In the following paragraphs, we will explain ellipsoids case and then describe the algorithm we used for isotherm surfaces.

One naïve way to check tumor coverage by an ellipsoid is to test whether each of the tumor vertices is located inside the ellipsoid or not. This is a fast method and works well for small tumors that can be covered by a single ellipsoid. But for large tumors requiring several ellipsoids (several needle insertions) to cover the mesh, we cannot simplify by working on mesh's vertices, because in some cases a consequential portion of the inner part of the mesh volume can be forgotten, as illustrated in Figure 5-2 (a). Therefore we used a method inspired by [16] that used the voxel representation of the tumor and verified if each voxel was inside at least one of the ellipsoids. This requires more computational time but will not miss any portion of the tumor as illustrated in Figure 5-2 (b).

Algorithm 5-1 represents the pseudocode for such an approach. We improved the algorithm by computing the amount of the defect volume to guide our optimizer for subsequent iterations.

While the tumor coverage condition is met, the volume of ablated healthy tissue is another important value which should be computed for each combination of the needles in order to be minimized. The centers of the ellipsoids are supposed to be located inside the tumor or ultimately centered on border of the tumor. Since some portions of the ellipsoids can exceed the tumor mesh, the voxels located in these portions are not taken into account while browsing the tumor. A simple solution to count these voxels is to create a large cube encompassing the tumor and candidate ellipsoids, and start browsing its elements. A 2D illustration of this solution is shown in Figure 5-3 (a) and as demonstrated in this figure, the dimensions of this cube are relative to the tumor edges plus the largest axis of the ellipsoid. The pseudocode of this method is also presented in Algorithm 5-3.

In this approach the number of voxels located inside the ellipsoids is computed. Depending on the location of needles, some voxels of the cube are shared among several ellipsoids, which should be deducted from the total count. This method requires a lot of computations especially for large tumors. In order to be more efficient in such a case, another approach is introduced which browses only the voxels inside the ellipsoid as shown in Figure 5-3 (b). In this method we first voxelize all ellipsoids and count the number of voxels inside each one, and deduce voxels shared by at least two ellipsoids (see Algorithm 5-2).

The performance of these two algorithms is compared with the same voxel and tumor size. In this comparison a tumor with the dimensions of 20 mm is selected, the ellipsoid's largest axis is chosen as 10 mm and the voxel size is 1 mm. Computation time for the first method with encompassing cube is 4.20 s while it takes 0.05 s for the second method to compute this volume. Using the second method we can compute the same volume 84 times faster than the large cube while not restricting the ellipsoids to be centered inside the tumor.

Simulated iceballs

For the case of iceball isotherm surfaces the ablated volume is represented by only one surface mesh, unlike the previous case. So in order to check whether the tumor is completely covered by the iceball or not, a first simple method consists in verifying only if the vertices on the surface of the tumor mesh are located within the iceball space which makes computations faster. This is illustrated in Figure 5-4 (a), where tumor vertices are marked with green squares.

However, in case the tumor is not completely covered, the minimization method needs to modify the configuration of needles to make it converge towards good tumor coverage. In order to supervise the minimization method, it is interesting to know the volume of uncovered tumor. So a second method is to voxelize the tumor and counts its inner voxels that are not covered by the iceball to compute their total volume, as shown in Figure 5-4 (a). Algorithm 5-4 shows this modification by defining a variable called uncovered_volume as a class member. This value is updated each time the tumor coverage function is called. This modification is beneficial for small tumors because of its low cost when browsing their voxels, while it has the advantage to compute the volume of uncovered tumor simultaneously.

When the tumor coverage condition is satisfied, it is essential to compute and minimize the volume of ablated healthy tissue. In this stage since the tumor is already completely covered by the

a) Using mesh representation b) Using voxel representation

Figure 5-2 Check tumor coverage a) vertices extracted from the tumor mesh are used for the test while in b) tumor is voxelized and the inclusion of each voxel is verified [16]

iceball, we simply deduce the total points of the tumor from the iceball total number of points. It is trivial that in the proposed pipeline it is not necessary to compute volume of the ablated healthy tissue if the tumor is not fully covered and it will force the optimizer to move the needle tips (see Figure 5-4 (b)).

Algorithm 5-1 check tumor coverage algorithm for multiple ellipsoid

```
Inputs:
  tumor_mask:  binary mask of the tumor
  ellipsoid_set: 3D surfaces of multiple ellipsoids
Result:
  is_covered: Boolean indicating if tumor_mask is completely covered by  ellipsoid_set

voxel_size ← Get tumor_mask voxel size
tumor_volume ← Get tumor_mask volume
covered_count ← 0, covered_volume ← 0, uncovered_volume ← 0
tumor_volume ← total_tumor_points * voxel_size
for each tumor_mask_point in tumor_mask  do
        for each ellipsoid_mesh in ellipsoid_set do
                if (tumor_mask_point is inside ellipsoid_mesh) then
                        covered_count  ←  covered_count+1
                        break
                end if
         end for
end for
covered_volume ← covered_count * voxel_size
uncovered_volume ← (tumor_volume –covered_volume)/tumor_volume
if (uncovered_volume ==0) then
        is_covered ←  true
else
        is_covered ←  false
```

Algorithm 5-3 Compute ablated healthy tissue volume for multiple ellipsoids.

```
Inputs:
  tumor_mask:  binary mask of the tumor
  ellipsoid_set: 3D surfaces of multiple ellipsoids
Result:
  healthy_ablated_volume: volume of ellipsoid_set which is outside tumor_mask

tumor_center ← Get tumor_mask center
voxel_size ← Get tumor_mask voxel size
total_tumor_points ← Get tumor_mask total number of points
Create large_cube_mask centered in tumor_center
total_count ← 0, shared_count ← 0,  shared_ellispoid_number ← 0
for each large_cube_point in large_cube_mask do
        for each ellipsoid_mesh in ellipsoid_set do
                if (large_cube_point is inside ellipsoid_mesh) then
                        total_count ← total_count+1
                        shared_ellispoid_number ←  shared_ellispoid_number +1
                        if  ( shared_ellispoid_number  > 1)
                                shared_count ← shared_count+1
                        end if
                end if
        end for
         shared_ellispoid_number ← 0
end for
healthy_ablated_volume ← (tolal_count – shared_count – total_tumor_points) * voxel_size
```

Algorithm 5-2 Modified algorithm to compute ablated healthy tissue volume for multiple ellipsoids.

```
Input:
  tumor_mask:  binary mask of the tumor
  ellipsoid_set: 3D surfaces of multiple ellipsoids
Result:
  healthy_ablated_volume: volume of ellipsoid_set which is outside tumor_mask

ellipsoid_num  ← Get number of ellipsoid_set elements
voxel_size ← Get tumor_mask voxel size
total_count ← 0, shared_count ← 0
total_tumor_points ← Get number of tumor_mask points
for i = 1 to ellipsoid_num do
        ellipsoid_image ← Voxelize ellipsoid_set(i)
        for each ellipsoid_voxel in ellipsoid_image do
                total_count ← total_count+1
                for j = i+1 to  ellipsoid_num  do
                        if (ellipsoid_voxel is inside ellipsoid_set(j))
                                shared_count ← shared_count+1
                                break
                        end if
                end for
        end for
end for
healthy_ablated_volume ← (total_count –shared_count – total_tumor_points) * voxel_size
```

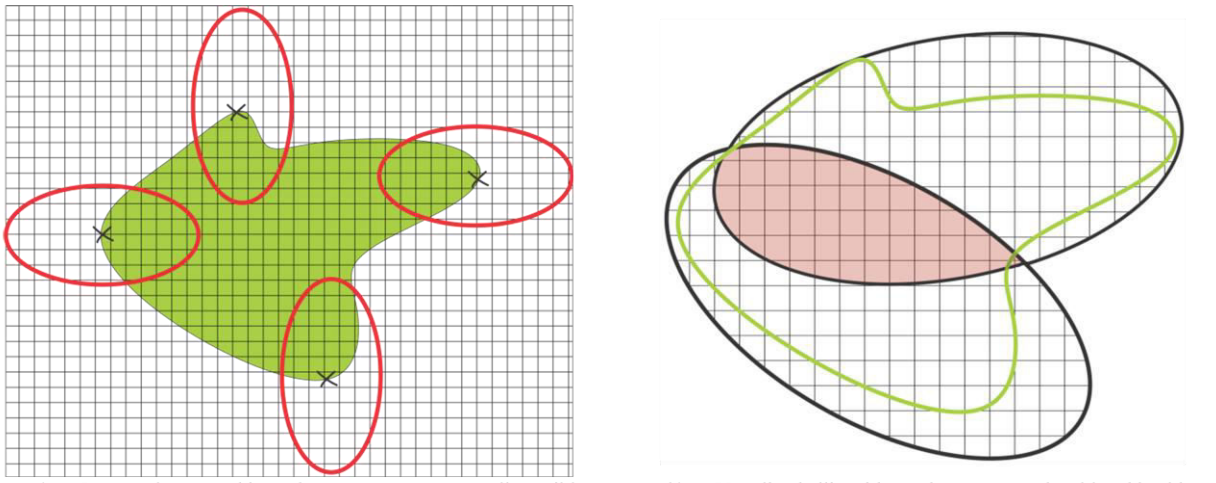

a) Large cube created in such a way to encompass all possible ellipsoids centered inside or on boundary of the tumor

b) Voxelized ellipsoids used to compute the ablated healthy volume. Shared voxels are in pink and should be deducted from the total grid points

Figure 5-3 Two proposed methods for computing the volume of the ablated healthy tissue while using multiple ellipsoids.

Algorithm 5-4 tumor coverage algorithm for iceball

```
Input:
  tumor_mask:  binary mask of the tumor
  needle_tip: set of needle tip positions and orientations
Result:
  is_covered: Boolean expressing if tumor-mask is covered or not by the iceball iso_surface

voxel_size ← Get tumor_mask voxel size
uncovered_count ← 0
bioheat_image ← Compute_bioheat_propagation(needle_tip)
iso_surface ← Threshold(bioheat_image, -40)
for each tumor_mask_point in tumor_mask do
        if  (tumor_mask_point  is not inside  iso_surface)
                uncovered_count ← uncovered_count + 1
        end if
end for
uncovered_volume ← uncovered_count * voxel_size
if (uncovered_count ==0)
        is_covered ← true
else
        is_covered ← false
```

5.3.2 Crossing needles condition

When dealing with multiple needles, a new condition needs to be fulfilled by the needles: their trajectories should not cross each other or get closer than a defined threshold based on practical considerations. In order to satisfy this condition we developed an algorithm which takes into account the distance of each pair of trajectories. A combination of these distances is returned to our

solver for its subsequent decisions. In Algorithm 5-5 a minimum permissive distance between trajectories is represented by constant *thresh*. Each time this condition is violated we penalize the distance by multiplying it by a weighted value.

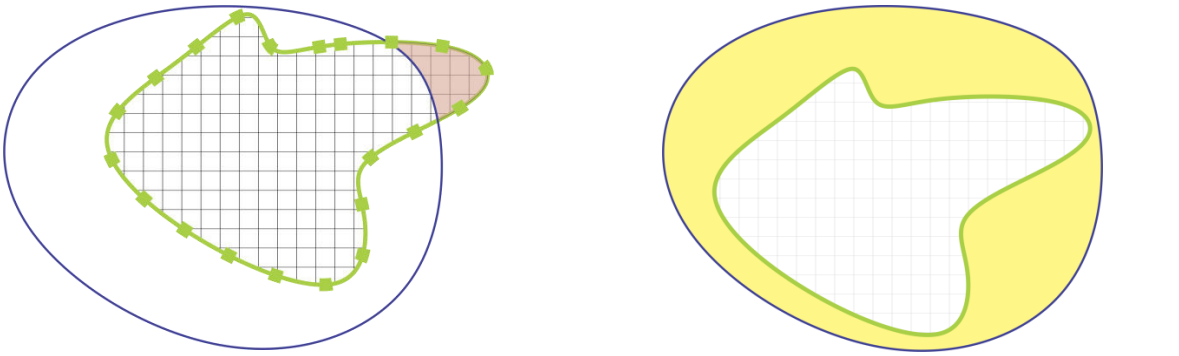

a) Tumor vertices shown as dotted are used to check tumor coverage. In order to compute uncovered volume, it is necessary to voxelize the tumor

b) Computation of ablated healthy volume shown in yellow is straightforward when the tumor is fully covered

Figure 5-4 Computing uncovered tumor volume and ablated healthy volume while dealing with iceball isotherm surface.

5.3.3 Insertion zone

In order to keep all trajectories inside the already computed insertion zone (as defined in Section 3.3), we have implemented an algorithm based on the minimal distance of each trajectory to the mesh of the insertion zone to supervise the minimizer while any of the trajectories are located outside the insertion zone. This algorithm is shown in Algorithm 5-6.

Algorithm 5-5 check needle crossing condition

```
Input:
  ellipsoid_set:  set of ellipsoids available for planning,
  trajectory_set: set corresponding trajectories
  thresh: chosen minimal distance between needles
Result:
  dist: cumulative weighted pairwise distances between needles

dist ← 0, weight ← 100
ellipsoid_num ← Get number of ellipsoid_set elements
for i=1 to ( ellipsoid_num  - 1 ) do
        for j = i+1 to ( ellipsoid_num ) do
                pairwise_dist ← distance(trajectory_set(i), trajectory_set(j))
                if ( pairwise_dist < thresh) then
                        dist = dist + weight*(thresh -  pairwise_dist )
                end if
        end for
end for
```

5.4 Conclusion

This chapter described the method in which surgical rules were converted into the lexical constraints and showed how new operators and operands defined while presenting examples. This lexical framework enables us to add new surgical rules or modify the existing ones using operators, variables and constants already available in the geometric universe. This will extend the software for its use in new applications or experiments without manipulation of the compiled binary file.

Then several algorithms required in the next chapter for optimization processes were discussed. These algorithms concern the computation of different volumes, and constraints like distance to the insertion zone or distance to other needles. Volume computations were done using multiple ellipsoids or simulated iceball and in each case the volume of covered tumor or volume of ablated healthy tissue was calculated.

As these algorithms are integrated in the optimization process and should be computed in each iteration, it was essential to implement these computations as fast as possible. For this reason, different algorithms were implemented and faster ones were proposed. For computing the simulated iceball volume, considering edges of the tumor instead of all the tumor points completed faster and for the ellipsoids volume computation, sweeping ellipsoids voxels in contrast to a large encompassing cube was more beneficial.

Algorithm 5-6 Proposed method for verifying placement of the needles regarding to the insertion zone

```
Input:
  insertion_zone: pre-computed insertion zone created after applying hard constraints,
  trajectory_set:  set of corresponding trajectories
Result:
  dist: cumulative weighted distance of needles to the insertion_zone

dist ← 0, pairwise_dist ← 0, weight ← 100
traj_num ← Get number of trajectory_set elements
for i=1 to ( traj_num ) do
        pairwise_dist ← distance(trajectory_set(i), insertion_zone)
        dist = dist + weight * pairwise_dist
end for
```

In the last part, two new constraints are introduced which are essential while working with multiple needles. The first one computes a cumulative weighted distance of all pairs of needles in order to make sure that none of the needles will cross each other in the placement phase. A weighting factor is used to penalize the violation of this constraint. For the purpose of keeping all trajectories inside the insertion zone in the second constraint, a cumulative weighted distance of each trajectory to the insertion zone is computed. In each case the corresponding algorithm was also presented for the reader to follow the required steps.

Chapter 6. Planning and optimization

6.1 Overview

Now that we introduced in Section 4.2 the numerical method to simulate accurately an iceball in the presence of vessels, and in Section 5.2 the geometrical constraints that apply on the positioning of multiple needles, this new chapter covers the core of the planning system. In Section 6.2 basic concepts of optimization are shortly described. Then, using these concepts, in Section 6.3.1 a specific formulation of the planning problem is presented in addition to the constraints. Section 6.3.2 summarize the experimented optimization approaches with their most suitable parameters to the planning problem and the final results based on these methods are shown in Section 6.4. This part describes the characteristics of experimental data and introduces several possibilities for solving the planning problem. In the following section the best method is validated in three different ways, and this chapter is concluded in the last section.

6.2 Introduction

The problem of multiple needle placement for tumor ablation can be formulated as an optimization problem with several parameters as input variables like needle's location and orientation, number of needles, needle's type and simulation time. Moreover, all the surgical rules discussed in Section 1.3.1 can be translated into the formula as non-linear constraints. Thus the best available planning is equivalent to the optimal solution of its corresponding optimization problem. For this reason Sections 6.2.1 and 6.2.2 review the logic and basic concepts of the optimization methods we experimented.

6.2.1 Optimization problem

By definition an optimization method aims at finding a desired solution among all possible solutions in an optimization problem by minimizing or maximizing a pre-defined objective function. The first step in any optimization problem is to formulate the physical problem into a mathematical model. This model should precisely describe the actual problem and any discrepancy between these two leads to final unexpected results. A non-linear single-objective optimization problem with inequality constraints is generally formulated as:

$$\min_{x \in \Omega \subset R^n} f(x) \qquad \text{subject to} \quad g(x) \leq 0 \tag{6-1}$$

Where $f(x)$ is the objective function, $x \in R^n$ is a vector of input variables, $g(x)$ represents non-linear constraints in the problem and Ω is the acceptable space for the problem.

After the mathematical formulation of the problem as an objective function f is achieved, an ef-

ficient numerical approach for optimizing it needed to be found, since any selected optimizer tries to evaluate the objective function for thousands of times [64, 65]. As most of the engineering applications need to use extensive computational methods like finite difference or finite element solvers in their objective function, which is the case of our bio-heat propagation computations, finding a tradeoff between accuracy and speed was essential.

The selection of the appropriate optimizer for a specific type of optimization problem is another important step that increases the chances of converging to the desired optimal results. Many optimization algorithms exist in the literature and no specific algorithm is widely applicable to all problems, as explained by Wolpert et al. [66]. Optimization methods can be classified in several ways based on the problem type or the solver characteristics including gradient-based (or derivative-based methods) and gradient-free (or derivative-free methods). Optimizers in the first group use the derivative information in their computations like steepest descent and Gauss-Newton methods. These optimizers are not suitable for an optimization problem where the objective is discontinuous. Conversely, optimizers in the second group like the Nelder-Mead downhill simplex method [67] only utilize the values of the objective functions and can be used when the objective is discontinuous and no derivative can be computed.

In another approach, methods can be classified into trajectory-based or population-based. A trajectory-based algorithm starts with a single initial point and makes a path towards a minimum as the iterations and optimization process continue. A popular example is the well-known simulated annealing method [68]. Population-based algorithms such as genetic algorithm [69] or particle swarms method [70, 71] use several solutions and proceed in multiple paths.

Algorithms can also be classified as deterministic or stochastic. Deterministic methods have no random nature and behave in a pre-defined way. Such algorithms will always reach the same final point when starting with similar initial point. Hill-climbing and downhill simplex are good examples of deterministic algorithms. If the objective function of an optimization problem is highly nonlinear and multimodal, these algorithms are not suitable due to its local nature. On the other hand, if there is some randomness in the algorithm, the algorithm usually obtains different results in each run of the algorithm, even though the initial point remains the same. However, using a sufficiently large number of random drawings, these algorithms are supposed to converge statistically towards the same minimum. Genetic algorithm is an example of such stochastic algorithms.

Several types of randomness exist in the stochastic algorithms. For example, a simple and efficient method is to add a random starting point to a deterministic algorithm. The hill-climbing method with random restart is an example. This simple technique is easy to implement and also efficient in most cases. A more sophisticated way to create randomness in an algorithm is to use randomness inside particular components of an algorithm, which in such a case is called a heuristic algorithm [72, 73]. The genetic algorithm uses randomness for crossover and mutation components in terms of a crossover probability and a mutation rate.

From another point of view, algorithms can be classified into global and local methods. Local search optimizers, like simplex method, typically converge to a local solution, not necessarily the best solution. Such algorithms are often deterministic. They have the drawback of getting often

stuck in local optima, while it is usually desired to find the global optimum for any given problem. In most cases, modern heuristic algorithms are designed for global optimization, though not always successful or efficient.

For computationally expensive, noisy or non-differentiable problems, using the actual objective function is not necessarily the best practice. In such cases, the surrogate-based optimization algorithms may be useful. In such approaches, the direct optimization of the objective function is substituted by iterative updates and optimizations of a low fidelity model of its values over the space called surrogate [74]. The surrogate model is constructed from the sampled evaluations of the original objective function: it is assumed to be a cheap, smooth, and easy to optimize substitute of the objective function, while being reasonably accurate to generate a good prediction of the function's optimum.

After choosing a suitable solver among these above mentioned categories, one should set the internal parameters of the solver in order to fit the problem characteristics at best and increase the robustness of the algorithm for this type of problem. The different methods provide many simple or sophisticated parameters to set beforehand. They should be considered while selecting the optimizer for a specific problem. In practice, even with the best possible algorithms, the optimal solutions might still not be achieved, as most of the non-linear global optimization problems are NP-hard and no efficient solution (in the polynomial sense) exist for them. So the main challenge is to find an optimization algorithm to obtain the best possible solutions in all cases, in a reasonable time (with a minimum number of iterations), while being able to define good parameters that work for any possible experimental case without the need of adjusting them for each case. This is the aim of Section 6.4.

6.2.2 Constraint handling

Constraint handling methods can be classified into generic methods that do not use the mathematical structure of the constraint, and specific methods that are only applicable to a specific constraint type. Generic methods, like the Lagrange multiplier method mostly applied to equality constraints and the penalty function method [75] can be simply used in different problems with no change to the algorithm. But as generic methods, their performance can be suboptimal. However, methods like the cutting plane, the gradient projection and the reduced gradient [76] have more accurate results, but they are applicable to specific problems with convex functions and to problems having few variables, due to their computational burden with large number of variables.

Because of the above restrictions in constraint handling methods, in this thesis a nonlinear constraint handling technique based on the penalty function method is used. The penalty terms are combined with the actual objective function in such a way that while comparing two feasible solutions, the one with better objective function value is chosen, when one feasible and one infeasible solution are compared, the feasible solution is chosen, and in a case with two infeasible solutions, the one with smaller constraint violation is chosen.

The penalty function method [77] for general optimization constraints needs to modify the objective function with a penalty term which depends on the amount of constraint violation $h: R^n \rightarrow$

R. The original optimization problem in (6-1) is thus modified as below, where $\lambda > 0$ is a penalty parameter:

$$\min_{x\in\Omega\subset R^n} f(x) + \lambda h(x) \tag{6-2}$$

If the penalty parameter is iteratively increased (tending to infinity), the solution of (6-2) can converge to the original problem in (6-1). However, in certain cases, a finite (and fixed) value of the penalty parameter λ results in the correct solution and is called the exact penalty [77]. By adding the penalty terms to the objective function, the modified cost function around the solution is not smooth [77], and thus the amount of non-linearity for the corresponding optimization problem increases. In such a case, the derivative-free optimization methods can be appealing.

The general definition of constraint term $h(x)$, where I and J are the indices that refer to inequality and equality constraints is:

$$h(x) = \sum_{i\in I} \max\big(0, g_i(x)\big) + \sum_{j\in J} \big|g_j(x)\big| \tag{6-3}$$

It should be noted that in our problem we have only inequality constraints. In the formula mentioned above the search includes both feasible and infeasible points. Such optimization methodologies in which the optimum can be approached from outside the feasible region are called exterior methods [78].

6.3 Surgical planning formulation

6.3.1 Problem formulation

The optimization process allows to refine the number and placement of the needles (3 translations and 2 rotations for each) to minimize a defect function. It is based on an iterative procedure including the bioheat equation resolution or computation of specific volumes for multiple ellipsoids at each step. In the case of simulated iceballs, every resolution begins with the assumption that an initial placement of the cryoprobes is given. Then, the bioheat equation can be solved. The resulting temperature field is processed to evaluate the defect function providing a quantitative estimate of the mismatch between the frozen tissue and the target tissue. Equations (6-4) – (6-8) show definition of the cost function and its related functions.

$$f(T) = w_{\text{volume}} * f_{volume} + w_{\text{risk\_vessel}} * f_{\text{risk\_vessels}}(T) + w_{\text{risk\_ribs}} * f_{\text{risk\_ribs}}(T) \tag{6-4}$$

$$f_{volume} = \int_V \mu_{\text{healthy}}\big(\theta_T(x)\big)\, dx \tag{6-5}$$

$$\mu_{\text{healthy}}\big(\theta_T(x)\big) = \begin{cases} 1 & \text{if } \theta_T(x) \le \tilde{\theta} \text{ and } x \text{ is in the healthy region} \\ 0 & \text{if } \theta_T(x) > \tilde{\theta} \text{ and } x \text{ is in the healthy region} \end{cases} \tag{6-6}$$

$$f_{\text{risk\_vessel}}(T) = \max\left(\frac{5 - \min\limits_{i=1:N} dist_{\text{vessels}}(t_i)}{5}, 0\right) \tag{6-7}$$

$$f_{\text{risk\_ribs}}(T) = \max\left(\frac{5 - \min\limits_{i=1:N} dist_{\text{ribs}}(t_i)}{5}, 0\right) \tag{6-8}$$

Where T represents a set of simultaneous trajectories with N elements which N is the number of

needles used in the operation. Each element of this set is taken from Ω which is a complete set of possible parameters for needle placement (3 parameters for translation and 2 for orientations). Finally $x \in S \subset R^3$ presents an arbitarary point inside the tissue.

$$\Omega = \{P \in R^5 | \sigma_i \leq p_i \leq \tau_i; \sigma_i, \tau_i \in R\} \tag{6-9}$$

This objective function is subjected to several non-linear hard constraints which have been studied in details in previous chapters. Computation of several hard constraints in each iteration is unnecessary once there is one constraint which is already violated. Thus a sequential resolution of the hard constraints is reasonable. For this reason in the first place we prioritize all the constraints and then added a regularization factor (bias value) to each constraint in order to keep its output value in a pre-defined range. In this way the consequent constraints are computed only if all their previous constraints were satisfied. In Equations (6-10) – (6-14) an aggregative sum of three hard constraints and its related functions as well as their weighting and regularization factors are presented.

$$h(T) = \text{Constraint}_{IZ}(T) + \text{Constraint}_{Cross}(T) + \text{Constraint}_{Coverage}(T) \tag{6-10}$$

$$\text{Constraint}_{IZ}(T) = \sum_{i=1}^{N} w_{IZ} * |dist_{IZ}(t_i)| + \text{bias}_{IZ} \tag{6-11}$$

$$\text{Constraint}_{Cross}(T) = \sum_{i=1}^{N-1} \sum_{j=i+1}^{N} w_{Cross} * max\big(\tilde{d} - dist(t_i, t_j), 0\big) + \text{bias}_{Cross} \tag{6-12}$$

$$\text{Constraint}_{coverage} = w_{Coverage} * \int \mu_{tumor}\big(\theta_T(x)\big)\, dx + \text{bias}_{coverage} \tag{6-13}$$

$$\mu_{\text{tumor}}\big(\theta_T(x)\big) = \begin{cases} 0 & \text{if } \theta_T(x) \leq \tilde{\theta} \text{ and } x \text{ is in the tumor} \\ 1 & \text{if } \theta_T(x) > \tilde{\theta} \text{ and } x \text{ is in the tumor} \end{cases} \tag{6-14}$$

Where $h(T)$ is a cumulative sum of all hard constraints in our problem; Constraint_{IZ} will enforce the trajectories to locate in a pre-computed insertion zone; $\text{Constraint}_{Cross}$ is the condition which avoids solutions with too close or crossing trajectories. In this constraint $\tilde{d}$ is the minimum distance between two trajectories. The last term in Equation (6-10) checks whether the tumor is fully ablated or not, $w_{IZ}, w_{Cross}, w_{Covg}$ express the penalty weights and bias_{IZ}, bias_{Cross}, $\text{bias}_{Coverage}$ are regularization biases for each hard constraint. Finally similar to the Equation (6-2), this optimization problem including all its non-linear hard constraints can be formulated as follows:

$$\min_{T \in R^{5*N}} f(T) + h(T) \tag{6-15}$$

This modified formula will be used as the optimization cost function afterwards. In order to normalize the values of this cost function, all the weights and biases are chosen in such a way to restrict the cost function value between 0 and 100. This range is divided into several bounds which are regulated for each constraint depending on how all weights and biases are chosen. For the comparisons in following Sections 6.4 and 6.5 we have chosen the bound [55, 100] for possible objective function values obtained by violating the insertion zone and crossing needles constraints. The bound [25, 55] is selected for possible values of objective function while the tumor coverage constraint is violated and finally the least bound [0, 25] will refer to the possible values for the soft constraints in Equation (6-4). Inner terms in this equation are already normalized as discussed in Section 5.2 and here are scaled using their weights to fit this bound.

6.3.2 Optimization methods

Methods used in this chapter are selected based on the special properties of the objective function and hard constraints. The objective function of the planning problem is multi-modal and non-linear while the hard constraints are discontinuous, non-smooth and there is no explicit formula available for them. Therefore, all of the optimizers are selected among derivative free methods with local and global characteristics in accordance to a classification by Rios et al. [79]. Specific properties of each selected method are shown in Table 5. Five optimizers are selected among SCOLIB[6] optimization library and one method for surrogate-based optimization is taken from the DAKOTA[5] optimization library.

SCOLIB[6] (known also as COLINY) is a collection of non gradient-based optimizers. These optimizers include coliny_cobyla, coliny_direct, coliny_ea, coliny_pattern_search and coliny_solis-wets which will be shortly introduced in this section. Each method uses a specific stopping criterion based on its optimization logic, which can be a maximum number of iterations or a threshold based on a relative change in the objective function value between successive iterations. For our experiments, the maximum number of iterations was set to 10,000 and for the stochastic methods each solution was repeated five times and the most frequent or the average solution was selected.

Each optimizer requires to set several variables or to select options among the available parameters. There is no unique configuration suiting all optimization problems and one should set them according to the problem in hand. So, in a preliminary step several test problems have been solved by each optimizer and continuously changed the parameters. The goal was to find the parameters that produced the best solution while keeping their efficiency in all the tests. All methods and parameter specification names used in the following tables are directly taken according to their source naming conventions.

Table 5 Classification of selected methods based on their properties

Method	✓	local	deterministic	unconstrained	direct	gradient based
	×	global	stochastic	constrained	model based	derivative free
coliny_cobyla		✓	✓	×	✓	×
coliny_direct		✓	✓	×	✓	×
coliny_pattern_search		✓	×	×	✓	×
coliny_solis-wets		✓	×	×	✓	×
coliny_ea		×	×	×	✓	×
SBO_trust		✓	×	×	×	×

In the following section a short description of each method we chose to experiment is presented briefly along with the selected parameters.

coliny_pattern_search

In each iterate of this method a pattern is generated from a set of points and the location of im-

[5] https://dakota.sandia.gov/
[6] https://software.sandia.gov/trac/acro/wiki/Packages

proved points in the design space is determined. Traditional pattern search methods use a fixed pattern to find improvements of the current iterate but the SCOLIB pattern search method implemented a more general strategy. It controls how the search pattern is generated, as well as how it should be evaluated. The form of the pattern search is controlled by the pattern_basis parameter. Coordinate basis is selected for the pattern_basis in which the pattern search uses the forward or backward points in each coordinate direction. The initial_delta and threshold_delta parameters provide the initial pattern size and the minimum size of the pattern to terminate the algorithm and they are respectively set to 1 and 1e-8. This distance is paved with different step lengths which can be expanded or contracted. The value of contraction_factor is set 0.9 which prevents this method to converge very fast. It can also expand the step length by the value 1/contraction_factor. exploratory_moves controls how a new pattern is adapted which is set to adaptive_pattern in our tests and will change the pattern each time an improvement point is found.

coliny_solis-wets

This algorithm is a simple greedy local heuristic method for variables in the continuous domains. Trial points are generated using a multivariate normal distribution, and then failed trial points are reflected to different directions of the current point in order to find a descent direction. In many of the optimization problems, a greedy method can't produce an optimal solution, but it can converge to the solutions approximating the global optimum. This method accepts the parameters like dynamic rescaling of the step length, initial_delta, threshold_delta and contraction_factor which are set similar to the pattern-search method.

coliny_cobyla

COBYLA is the abbreviation of Constrained Optimization BY Linear Approximations which is an extension to the Downhill simplex method in order to handle linear or nonlinear constraints. The COBYLA method applies linear approximations to the objective function and approximations are computed using the linear interpolation at N+1 points among the input variables with N equals to the number of variables. The vertices of a simplex is generated from these interpolated points. The step length modifies the size of the simplex which is automatically reduced from an initial_delta = 0.5 to the threshold_delta = 1e-8.

coliny_direct

The DIviding RECTangles (DIRECT) optimization algorithm is a non gradient-based global optimization method which tries to merge local and global search characteristics. Local search is done in dominant regions of the search space while global search is used for unexplored regions. DIRECT method adaptively subdivides the feasible space in the proximity of a good solution. A subregion is subdivided if its size relative to the largest subregion is less than global_balance_parameter which is set to 0.7 in the tests. Intuitively, this makes large subregions to be subdivided prior to the small subregions. The local_balance_parameter checks whether the smallest subregion should be subdivided or not and a small value like 1e-8 is set in order to have a good convergence.

coliny_ea

Evolutionary algorithms are inspired from natural selection and reproduction processes and try to modify the parameters in order to ensure the survival of the specific samples in large populations. These algorithms are constructed as below:

1. In the first place an initial population should be randomly selected then function evaluations are computed for these individuals
2. Parents selection is done based on a relative fitness metric
3. Perform crossover and mutation to generate new individuals among those parents
4. For two selected parents a crossover should be applied with a fixed probability
5. If using crossover, mutation also should be applied to the newly generated individuals in previous step with a fixed probability
6. If no crossover is applied, then a mutation with a fixed probability is used for a single selected parent
7. In this stage, function evaluations are computed on the new individuals
8. Then replacement is done to create the new population.

Finally one should return to the parent selection step and continue the algorithm until the convergence criterion is met. The specification of used parameters in the experiments is shown in Table 6.

Table 6 Specification of input parameters used for the coliny_ea method

initialization_type	unique_random
population_size	number of variables
fitness_type	merit_function
crossover_rate	0
mutation_type	replace_uniform
mutation_rate	1
replacement_type	elitist

SBO_trust

Surrogate based optimization uses different types of approximation to build a low fidelity surrogate model of the objective function. It is regularly updated using data from a "truth" model. This surrogate model is the interpolation or regression of the truth model which is a high-fidelity simulation model. The surrogate-based methods aim at reducing the total number of truth model simulations and to smooth noisy data with simple analytical functions. Some existing global and local surrogate methods were tested on our planning problem. In global methods the surrogate model is updated with each true function evaluation so the required time for building the surrogates is an overhead to our computational time and it is annoying while working with more than 20 variables. As an example for 42 variables it takes 60 seconds to build the global surrogate in each iteration. We also conclude that the results of minimization in different tests were comparable to a less extensive surrogate method called surrogate local trust region method. Surrogate local trust region method restricts the range of variables to a trusted region in each iteration and builds a local surrogate of the

objective function using samples drawn from that region. Afterwards a minimization method is used to find the optimal point of the surrogate and based on the success of that point comparing to truth model, the trust region changes its center, shrink or expand and repeats this process till the size of trust region is less than a threshold. Finally, specification of our used parameters in the experiments is presented in Table 7.

Table 7 Specification of input parameters used in SBO_trust method

trust_region		
	initial_size	1
	minimum_size	1 e-10
	contract_threshold	0.2
	expand_threshold	1
	contraction_factor	0.8
	expansion_factor	3
FRCG conjugate gradient optimization method		
	max_function_evaluations	200
	convergence_tolerance	1e-8
surrogate_type		
	Interpolation_method	gaussian_process or kriging
	correction_method	additive zeroth_order
sampling		
	number of samples	number of variables
	sample_type	latin hypercube sampling

6.4 Experimental study

In this section different tests are done to compare the speed and convergence of the selected methods. The tests are presented by order of increasing complexity. The problem complexity depends firstly on the optimization parameters, which are the number of variables (variable space). In our case, the number of variables depends on the number of needles and the degrees of freedom of each needle. The effect of these parameters has been investigated by increasing the tumor size which impacts the minimum number of required needles to completely cover the tumor, thus the number of variables of the optimization. Therefore, in a first study the goal is to cover the tumor regardless of surrounding organs in order to observe the effect of the search domain on optimization results.

The second parameter which increases the complexity of the problem is the objective function characteristics, like the degree of nonlinearity or non-smoothness. In our problem, adding obstacles constraints or avoiding needles crossing constraint changes the shape of the objective function. Moreover, the observance of hard constraints by using penalty functions to ensure needles inclusion in the insertion zone or a minimum pairwise distance between needles increases the nonlinearity and discontinuity of the objective function and consequently makes the problem harder to solve. Thus a second study investigates the effect of the mentioned constraints on the optimizer's behavior. In order to perform these ordered tests, we have used different cases with specific properties as described in Table 8 for our tests.

Table 8 Specification of properties for different cases used in the tests

Case number	Tumor size	Insertion zone complexity	Distance to vessels
case#1	small	simple	far
case#2	medium	simple	far
case#3	medium	intermediate	close
case#4	medium	intermediate	far
case#5	large	simple	far
case#6	large	complex	far

6.4.1 Tumor coverage problem

We have used three cases among our six sets of prepared data (case#1, case#4 and case#6) with an increasing complexity to investigate the speed and convergence of optimizers in this section. For each case, planning started with a low number of needles and it was increased if no method was able to converge to a good minimum. No other hard constraint except full tumor coverage was considered in this experiment and all the volume computations were done using simplified ellipsoids as discussed in Section 5.3.1. In case#1 the tumor volume is the smallest with 1.050 cm^3. In order to ablate this tumor the needle model providing the smallest iceballs was selected among the different available needle types: IceSeed from Galil Medical. With this model, the volume of the -40°C ellipsoid is 1.473 cm^3. While the volume of the ellipsoid is larger than the volume of the tumor, it was not sufficient to cover the tumor due to the tumor shape as illustrated in Figure 6-1.

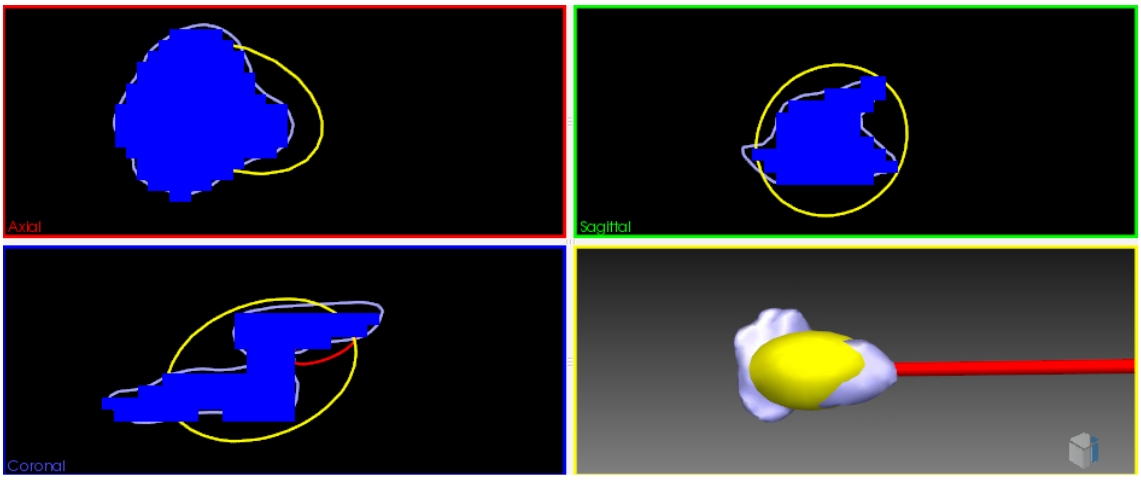

Figure 6-1 One needle ellipsoid can't cover the tumor with a smaller volume due to the non-homogeneity of tumor shape

In order to fully cover the tumor, the planning was experimented with two and three needles for comparing the methods behavior. It is visible in Figure 6-2 (a) that SBO-trust and Pattern-search could cover the tumor in less than 300 iterations while EA needed more than 1000 iterations for this task. Direct method rapidly started to reduce the objective function value but it got stuck in a local minimum for the rest of its iterations. The same situation happened for the Solis-wets which is a greedy method. Cobyla had the worst behavior, its speed was lower than other local search methods

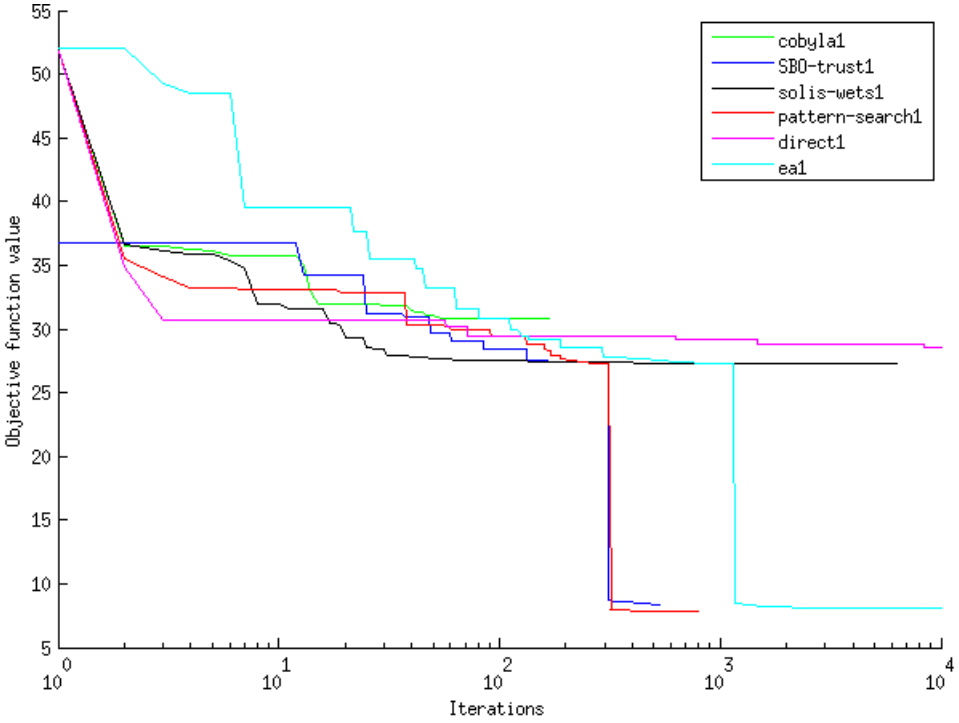

a) Six optimizers for Case#1 with two needles

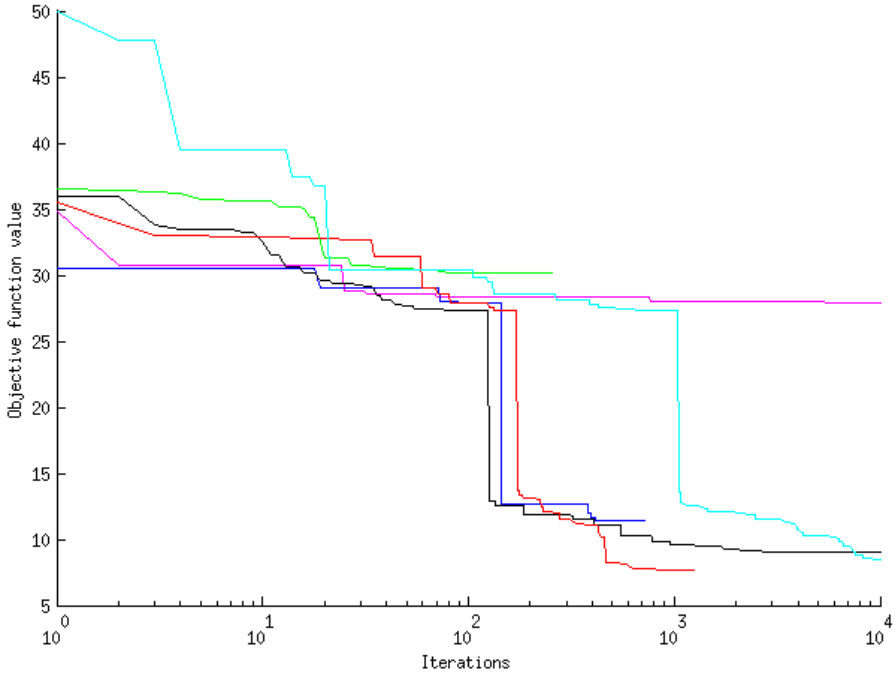

b) Six optimizers for Case#1 with three needles

Figure 6-2 Profile of the objective function values while covering the tumor with two different needle numbers. Speed and accuracy of the methods are compared using this profile.

and it converged into a local minimum close to its initial point. In Figure 6-2 (b) a similar trend is shown for the case of three needles but this time the Solis-wets was able to cover fully the tumor. Minimum damage to the healthy tissue is one of the main goals in the planning procedure so after covering the tumor, the minimum amount should be found. Table 9 represents a comparison among the four most successful methods based on the objective function value in the bound [0, 25]. The structure of the objective function value bounds is already described in the end of Section 6.3.1. However adding the third needle helped Solis-wets method to completely cover the tumor but in average tended to increase the volume of damage to the healthy tissue.

Table 9 Comparison of four most successful methods after convergence based on the optimizer's objective function value

method	Two needles	Three needles
Pattern-search	7.80	7.75
SBO-trust	8.39	11.37
EA	8.07	8.42
Solis-wets	-	9.08

In a similar way, experiments were performed on case#4, which has a medium tumor of 2.052 cm^3. As for the previous case, planning was done using different numbers of needles in order to compare the convergence. In this case, four IceSeed needles were required by the optimizers to fully cover the tumor. Experiments were also performed on case#6 with a big tumor of 3.645 cm^3 using seven needles. Figure 6-3 (a) and (b) illustrates the profile of all six optimizers for these cases with a trend similar to the previous experiment in which EA converges after a lag.

The interesting point in these tests highlights the effect of the increase in the input variables as the tumor size increase and the number of required needles increase, each optimizer needs more number of iterations to cover the tumor see Table 10.

Table 10 Minimum number of iterations for the tumor coverage problem is increased in cases with higher complexity

Method	Min iterations in case#1	Min iterations in case#4	Min iterations in case#6
Pattern-search	173	539	815
SBO-trust	145	553	1472
Solis-wets	126	937	1930
EA	1048	3464	-

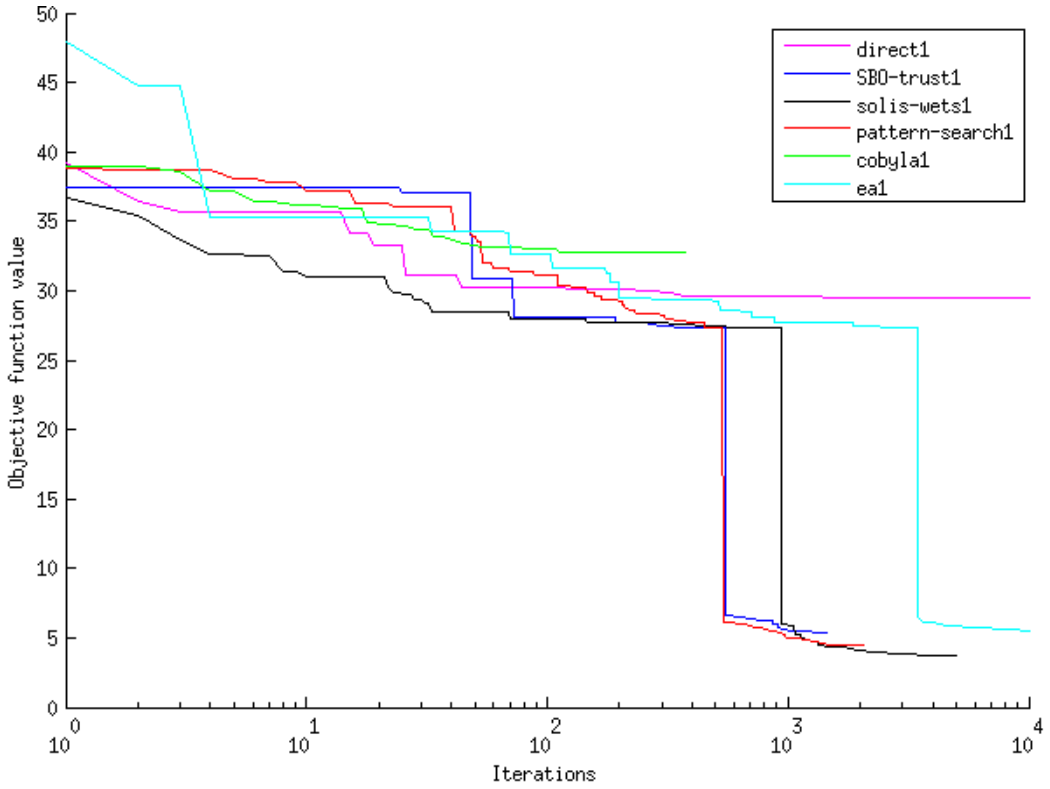

a) Result of six optimizers on the case#4 with four needles

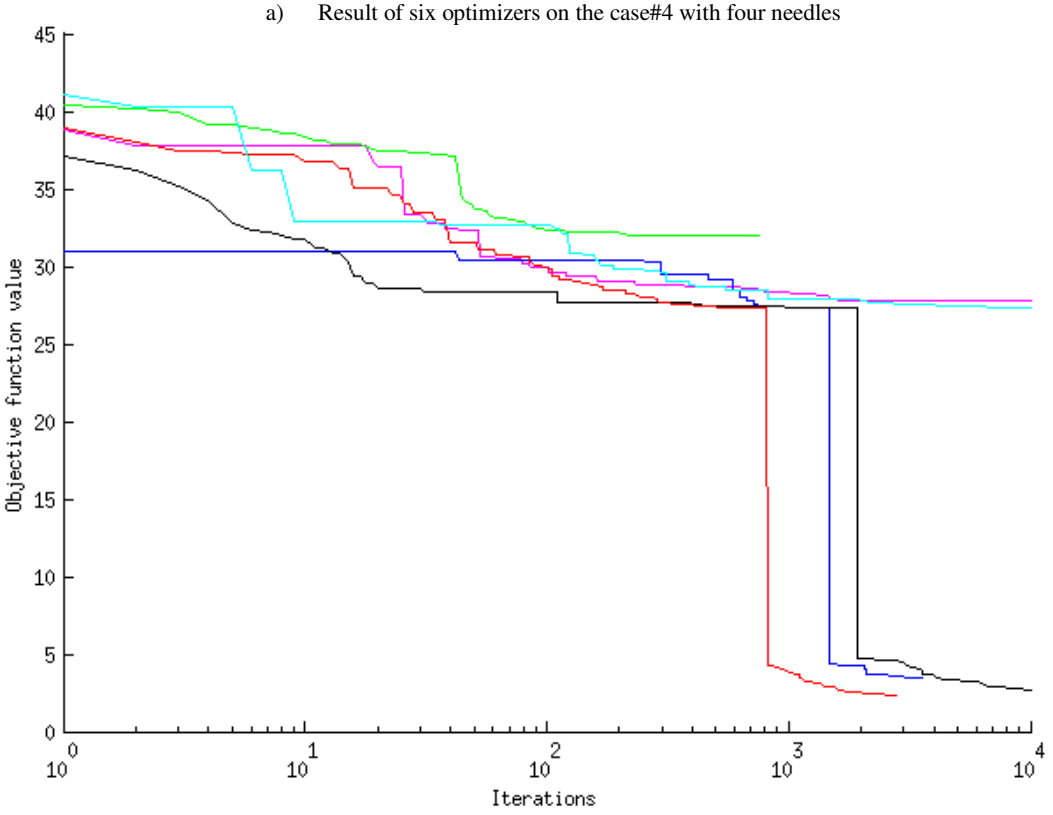

b) Result of six optimizers on the case#6 with seven needles

Figure 6-3 Comparing the profile of optimizer's objective function value in the tumor coverage problem for two cases

More experiments on covering larger tumors using IceSeed needles convinced us to use needle types providing larger -40°C iceballs as IceSeed is the model of needle with the smallest iceball. An example of using larger needles will be discussed in the next section.

6.4.2 Planning in presence of all constraints

In this section we are interested in ablating the tumor in presence of all the constraints discussed in the previous chapters like obstacles and crossing needles. The selected optimization methods in this part were applied on Equation (6-15) that solves the objective function while checking hard constraints satisfaction at the same time. The experimental data used in this section were again case#1, case#4 and case#6 in order of increasing complexity and with the same number of needles of the previous section. The insertion zone for each case was already computed.

As shown in Figure 6-4 (a) for case#1 only Pattern-search and Solis-wets were able to cover the tumor while satisfying the hard constraints and other methods were trapped in local minima. In this case the optimizers started with a low objective function due to a large insertion zone and low number of needles (this is important because the penalty terms are defined as accumulative distance error).

Table 11 Comparison of speed and convergence for successful search methods with and without the constraints

method	no constraints min value /min iterations for tumor coverage	with constraints min value /min iterations for tumor coverage
Pattern-search	7.75/173	11.88/237
Solis-wets	9.08/126	9.32/517

When comparing these results with the experiment of Section 6.4.2, we can see that optimizers needed more iterations to converge (lower speed) and the convergence was reached with a higher objective function value (see Table 11). This trend is similar for case#4 (see Figure 6-4 (b)), for which only one method was successful, and for case#6 (see Figure 6-5) for which it was not possible to cover the tumor while keeping the trajectories within the insertion zone. For case#6, planning with eight needles has also been investigated for this case with no success to fully cover the tumor.

This situation is caused by a tight and discontinuous insertion zone in case#6 as shown in Figure 6-9 (a) while it was possible to cover the same tumor with a wider insertion zone as in Figure 6-9 (b). But in order to ablate such a tumor, the surgeon should use a needle with a bigger iceball. So in Figure 6-5 (b) four IceSphere type needles were chosen to cover the tumor with a very good convergence 4.81% and a minimum number of iterations of 280 which seems fast and accurate.

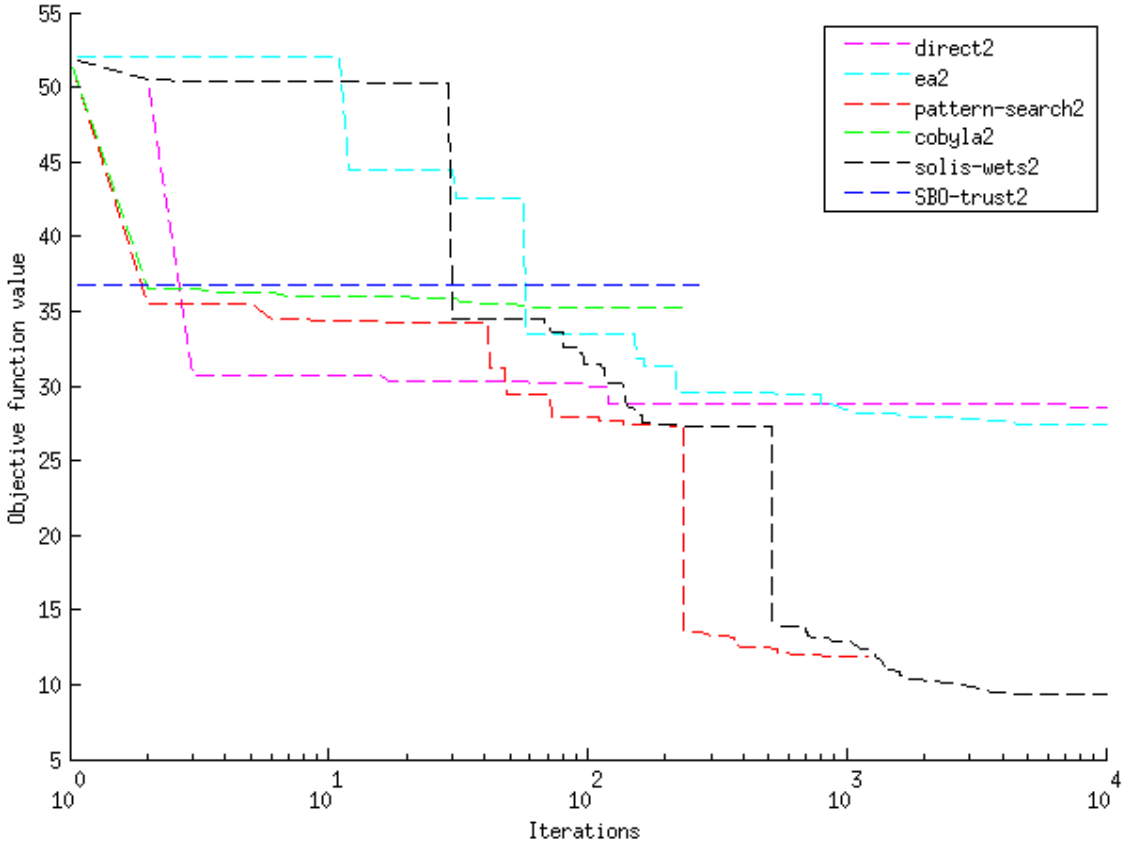

a) Six optimizers for the Case#1 with 3 needles

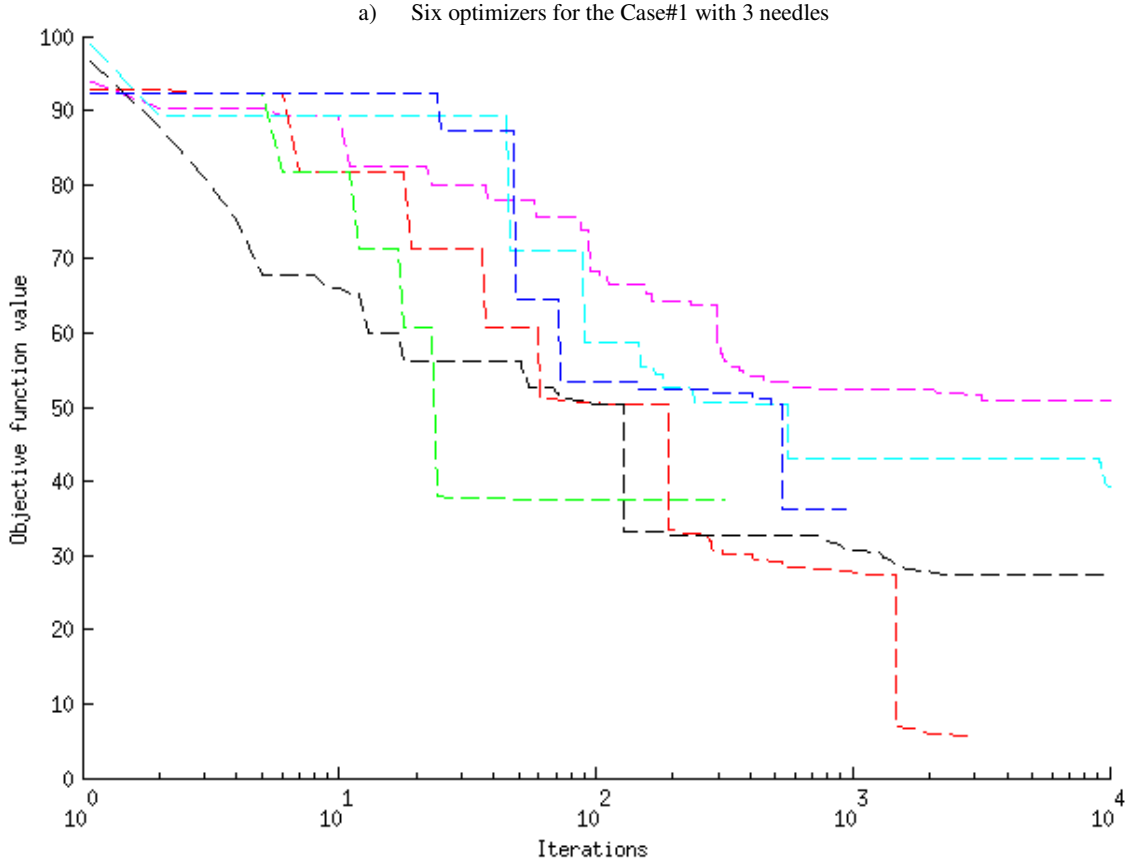

b) Six optimizers for the Case#4 with 4 needles

Figure 6-4 Profile of the optimizer's objective function value in presence of all constraints. Similar needle numbers and optimization methods are used in contrast to the cases with only tumor coverage constraint, but they are named and sketched differently for comparison purposes.

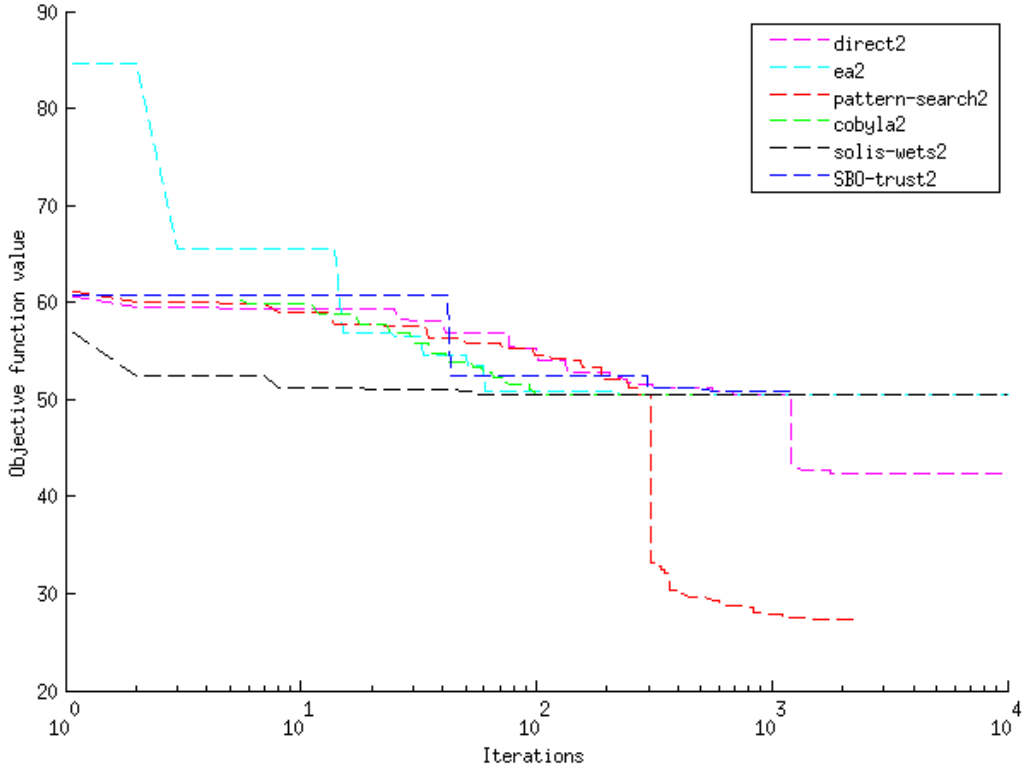

a) Six optimizers for theCase#6 with 7 needles

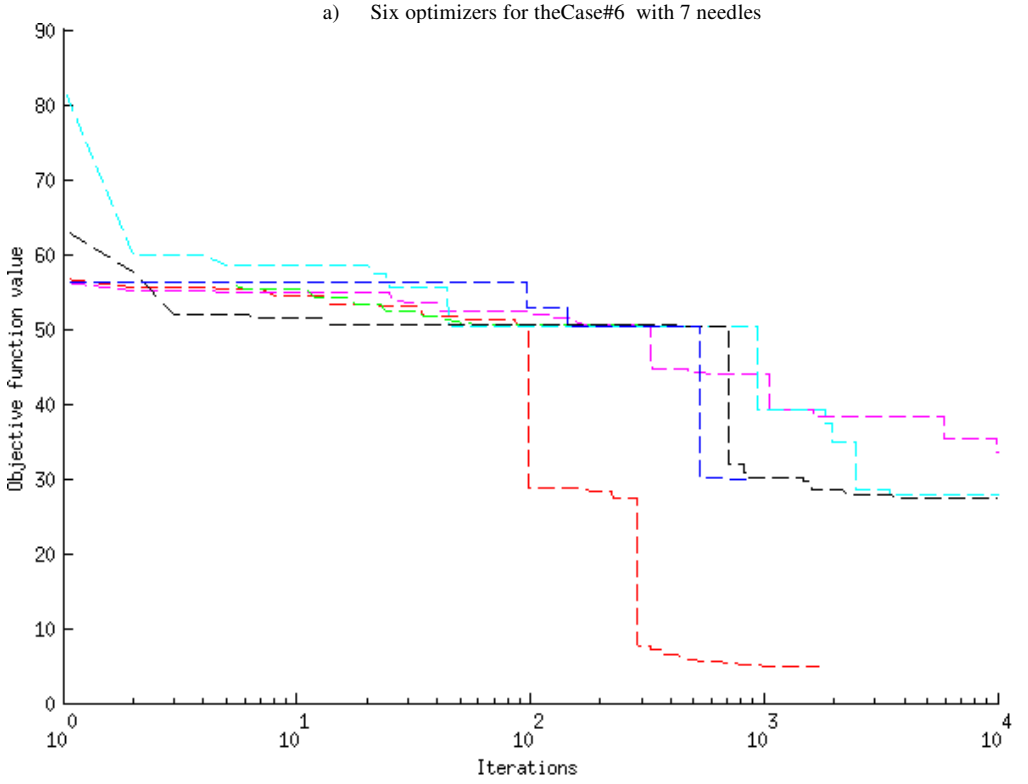

b) Six optimizers for theCase#6 with 4 larger needles

Figure 6-5 Effect of needle size on the solution of the hard problem. Profile of the objective functions shows that in a complex problem with all constraints and large tumor increasing the ablation zone can lead to a solution.

Another interesting point is the effect of the weighting terms in Equation (6-4). As discussed in Section 3.3, the insertion zone is defined as the subset of the skin containing all insertion points allow-

ing for feasible trajectories, i.e. satisfying the hard constraints. Among the hard constraints, the obstacles avoidance is treated by keeping only portions of the skin from which any straight line towards the barycenter of the tumor does not cross any obstacle. This hypothesis is not precise as the needles tips can be placed in tumor points other than the barycenter. The amount of error depends on the displacement from the barycenter and the geometry of the obstacles. In order to fix this problem as already mentioned in section 3.3 a term is added to the objective function value that counts the distance to the obstacles like ribs and vessels.

Figure 6-6 illustrates two successful solutions for the planning of case#4. In both cases, full tumor coverage is achieved and all trajectories are inside the insertion zone. For the right image, weight w_{vessel} in the term $f_{\text{risk\_vessel}}$ in Equation (6-4) was set to 0.0, resulting in a foremost needle closer to the vessel, while it was set to 0.2 for the left image where we can see that the foremost needle is farther from the vessel.

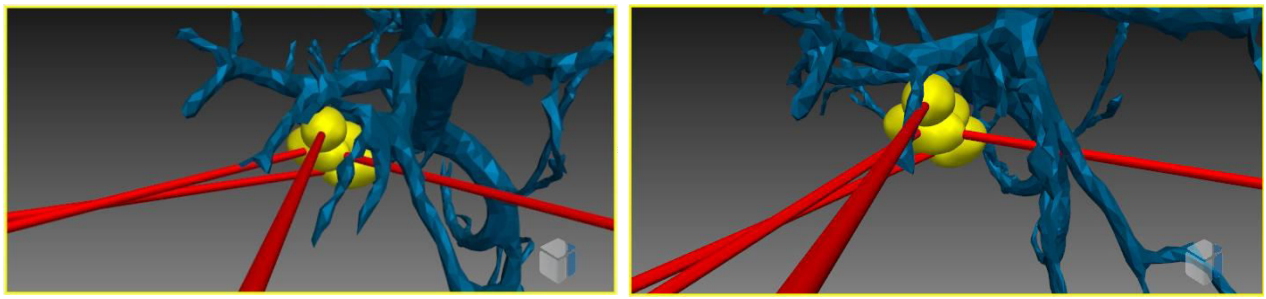

a) Weight of distance to vessel set to 0.2 b) Weight of distance to vessels set to 0.0

Figure 6-6 Changing the soft weights in the objective function results in crossing the obstacles while trajectories in both cases are inside the insertion zone.

6.4.3 Influence of the initial point on optimization

Many optimizers require a good guess for the initial point to converge accurately or for a fast convergence. We evaluated the effect of the initial point on different optimizers. Several points were selected to initiate each optimization process and finally the results of an initial point in middle of the variable bounds were compared to the worst initial point located outside the tumor's bounding box. Case#2 is used in this experiment which has a medium tumor size to provide enough space for changing initial points inside the tumor and a simple insertion zone in order not to be affected by the insertion zone shape.

Cobyla, Pattern-search and Solis-wets were the most sensitive to the choice of initial point and trapped into local minima. They could not converge to the same minimum when using different initial points. These final objective function values are presented in Table 12 and illustrated in Figure 6-8. Direct method does not use a user defined initial point so, it is computed once in order to show its behavior in this new case. SBO-trust and EA were the most interesting, converging differently but towards a similar minimum. The convergence was obtained with more iterations, as shown in Figure 6-8. This image is zoomed and the horizontal axis is not logarithmic in order to intuitively show the lag of convergence between two conditions for EA and SBO-trust. Based on these observations SBO-trust, EA and Direct can be considered as more robust to the initial point variances than the other three methods.

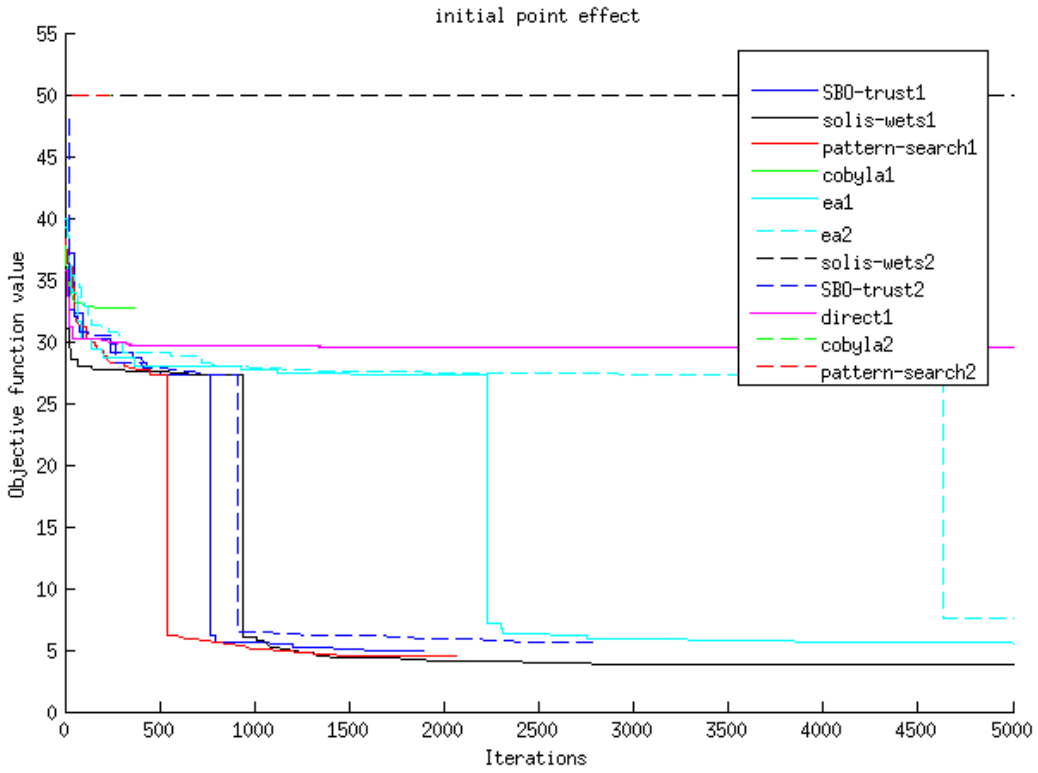

Figure 6-8 The profile of optimizers with two different starting points. Dashed lines illustrate the objective function profiles when using the worst starting point and they are labeled with Optimizer_name2 in contrast to solid lines which were initialized in the middle of their variable bounds.

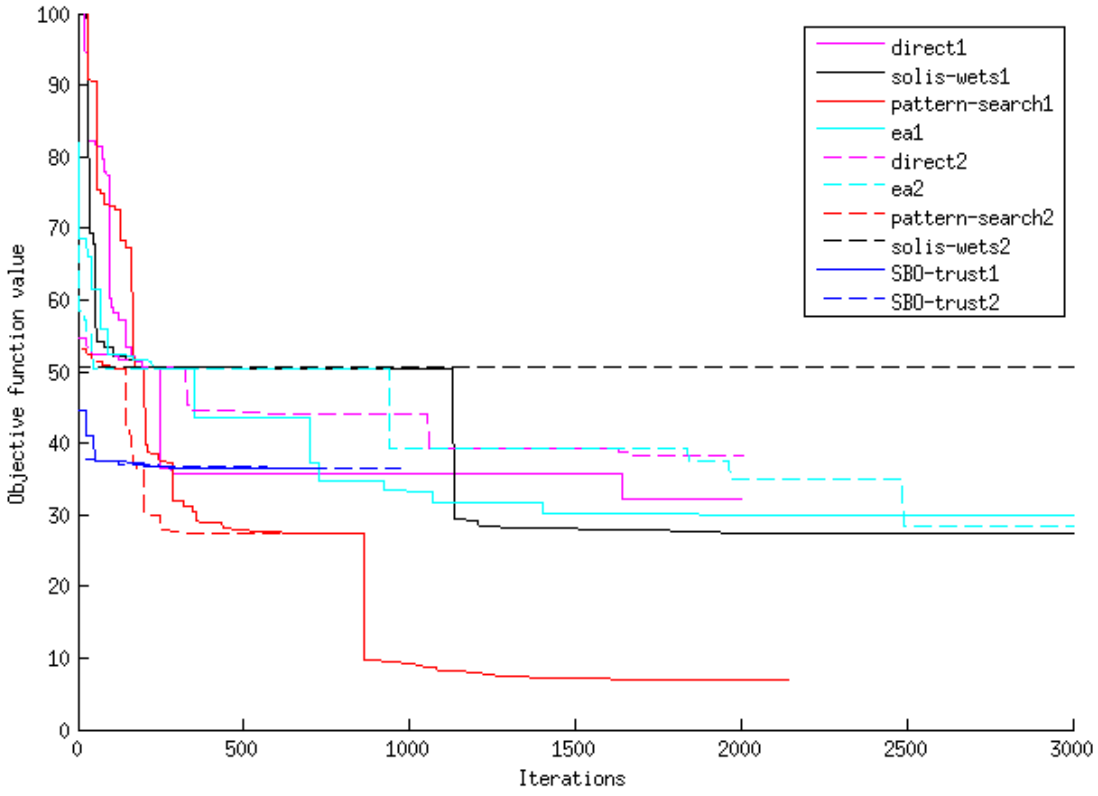

Figure 6-7 The effect of insertion zone complexity on the behavior of different optimizers is investigated. In this image solid lines demonstrate the trends of optimizer's objective function for simpler case#5 while dashed lines refer to the case #6

Table 12 The effect of initial point variation on the optimizer's final objective function value

Method	Initial point in the middle of the bounds	Initial point out of the tumor bounding box
Cobyla	32.76	50
Pattern-search	4.44	50
Direct	29.45	29.45
Solis-wets	3.77	49.95
EA	5.27	6.84
SBO-trust	4.93	5.58

6.4.4 Influence of the insertion zone on the optimization

In order to demonstrate the effect of the insertion zone on the optimization results, we compared the planning output for case#6 with two different placements of the same tumor shape and size. We created a synthetic case called case#5 by displacing the tumor to a posterior region of the liver which has a lower vessels density and a lower number of blocking ribs. In Figure 6-9 (b) the computed insertion zone is illustrated for these two conditions with a larger insertion zone and fewer numbers of discontinuities for the second one. After computing the insertion zone for both cases, different optimizers are used to compute the best planning solutions in presence of all the constraints. In Figure 6-7, the trend of each optimizer is drawn for both cases #5 and #6. None of the optimizers could cover the tumor in case #6 as it was discussed before in Section 6.4.2 for seven needles and small needle size. Then by repeating the experiment for the case#5 with similar tumor and needles but different insertion zone the Pattern-search method was able to successfully reach a good minimum which is due to the smoother insertion zone in this case. Figure 6-7 is zoomed into the first 3000 iterations and sketched on a non-logarithmic scale to have a better view on the changes between two conditions while the rest is more or less stable. In this figure, Pattern-search, Direct, EA and Solis-wets are the methods which have changed their convergence due to the insertion zone. For the SBO-trust the convergence did not changed between these two conditions. Table 13 presents the minimum values found by different optimizers after their convergence reached in two conditions of insertion zone.

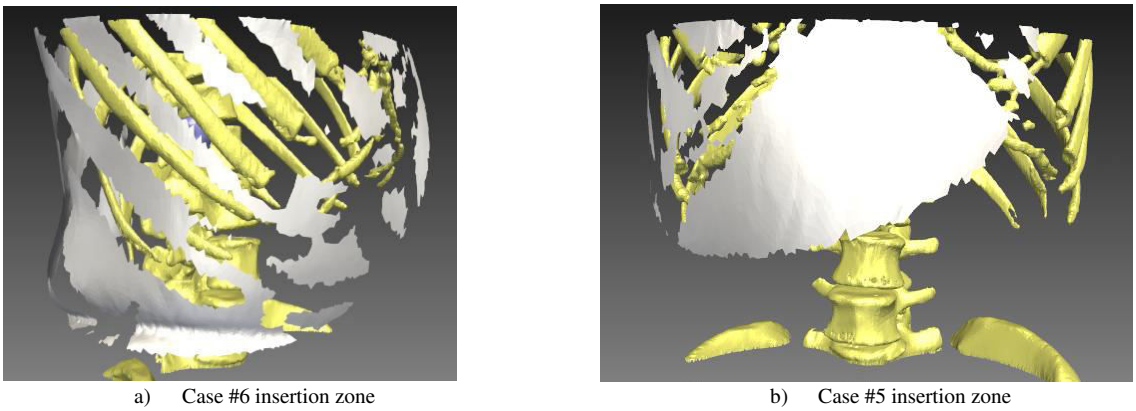

a) Case #6 insertion zone

b) Case #5 insertion zone

Figure 6-9 Computed insertion zone for two cases. Insertion zone in (a) shows a more complex and discontinuous solution space comparing to (b)

Table 13 Final objective function values for five optimizers found in two different conditions of the insertion zone

Method	Insertion zone case#5	Insertion zone case#6
Pattern-search	6.93	27.25
Direct	32.12	38.34
Solis-wets	27.29	50.52
EA	27.31	27.91
SBO-trust	36.45	36.45

6.4.5 Hybrid opimization and multiple output

The goal of planning tools such as ours is to assist the surgeon to find a good solution but still customizable for his experience and skills. In order to fulfill this target, it is essential to propose several optimal or near-optimal solutions to the surgeon. In order to produce such distinct propositions, we have defined a hybrid optimization method, using firstly a global method like genetic algorithm, building separate clusters among the best solutions Figure 6-10 (a), and then using a local optimization method in each cluster. For this purpose, an Euclidean distance metric was used to check the distance between computed best solutions by the global method. The centers of these clusters were chosen from the best answers of the global search. They were rejected if they are closer than a threshold to other centers. After clustering the solutions, a local optimization method is applied to find the local minima in each distinct cluster. Pattern search method was used, as it has shown to be our best global method so far, for the planning of case#4 in presence of all the constraints.

The distances between the optimal solutions of the distinct clusters are shown in the upper triangle of

Table 15. These values are normalized for each direction and also for the number of needles, for example if distance between solution one and two is 2 mm, it means that on average there is 2 mm distance in each direction x,y and z for any corresponding needle. The angular distance is presented in the lower triangle of

Table 15 and it is also normalized for each needle and each direction of $\alpha, \beta \; and \; \gamma$.

Among these solutions, six could converge to a good local minimum which covers completely the tumor as shown in Figure 6-10 (b). Finally the planning using this hybrid method could converge to a better solution compared to the results of the best optimizer for case#4 shown in Figure 6-4. The value of objective function was lower as presented in Table 14.

Table 14 Optimal value of the objective function improved while using the hybrid method

Method	Pattern-search	Hybrid
Optimal value	5.65	4.23

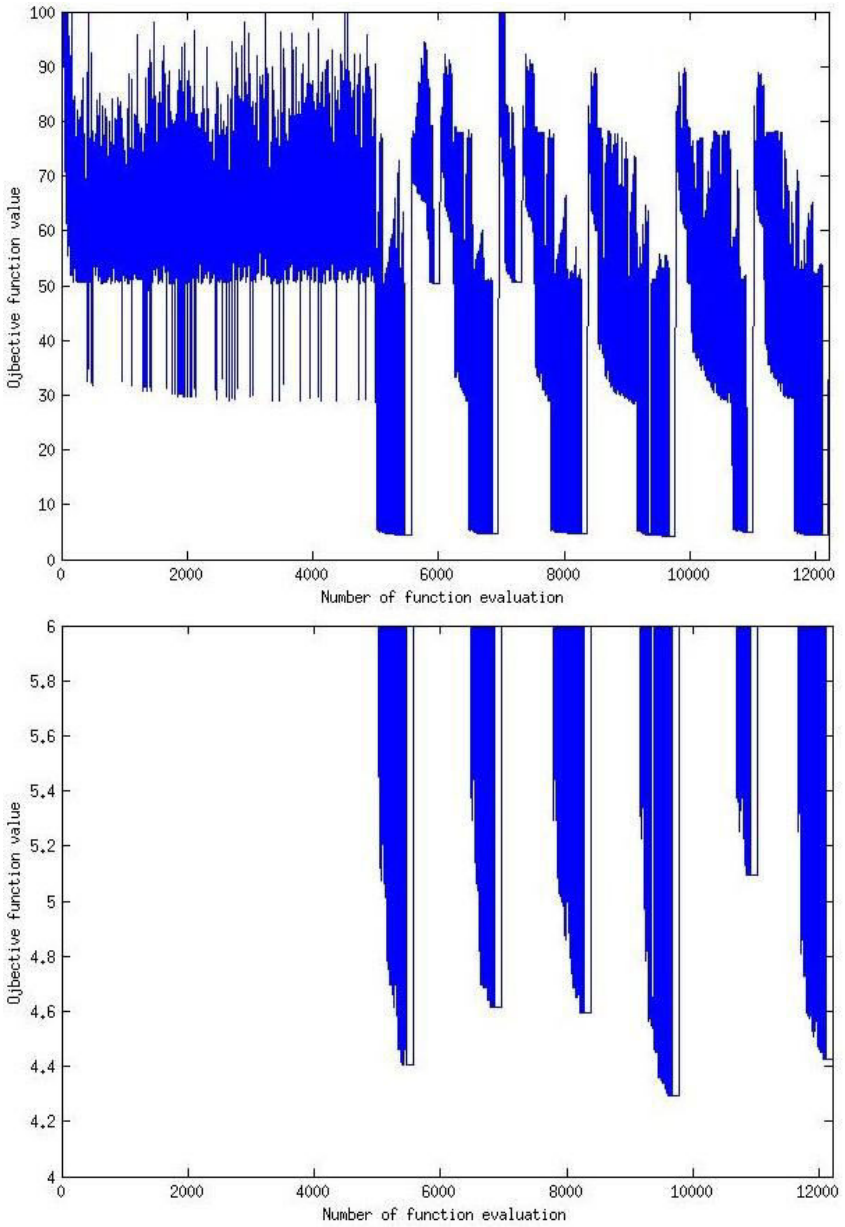

Figure 6-10 Complete trend of the hybrid optimization method is illustrated in the upper image. Eight distinct solutions selected from the first global method is shown along with their following local optimization trends. In the lower image six succesful solutions are compared.

Table 15 Angular and translational distances of 8 distinct solutions computed after the global optimization. All distances are normalized for each needle and each direction

Needle lable		Distance to needles (mm)							
		#1	#2	#3	#4	#5	#6	#7	#8
Anglular distance (degree)	#1		1.5	1.6	2.5	1.1	2.1	1.1	1.6
	#2	21.5		2.3	1.8	1.9	2.1	2.3	2.4
	#3	16.3	23.9		2.7	1.5	1.8	1.7	2
	#4	30.7	29	34.3		2.6	2	3.1	3.1
	#5	21.5	16.4	20.7	27.3		2	1.7	1.9
	#6	22.3	10.9	28.4	31.3	22.7		2.3	2
	#7	6.6	20.2	16.2	32.9	20.5	21.6		1.1
	#8	11.9	17.4	20	31.7	18.3	19	8.6	

6.4.6 Two-phase optimization

Estimating the ablated tissue using pre-defined theoretical ellipsoids is very fast, and enables to afford the use of optimizers with high numbers of iterations, or use hybrid methods, or optimizating with multiple starting points as presented in previous sections. But as discussed in Chapter 4, ellipsoids do not precisely estimate the ablation zone when using multiple needles or interfacing with other sources of heat in their neighborhood. Post-operative complications are directly related to the failure of a good ablation zone estimation. As explained in Chapter 4, the simulation of the heat propagation proposes more accurate results, so we wanted to use these more realistic simulations of the iceballs in our optimization process. However, the simulations are much longer to compute, so a fast optimization would be required.

In order to have an intuitive estimation of the time that would be needed by the optimization process using only iceballs simulations, we showed on top of Figure 6-11 the profile of a Pattern-search optimizer as a dashed line. This optimizer uses the same objective function formula as in section 6.3.1 but uses the simulated iceball as explained in Chapter 4. Each iteration takes about 50 seconds on a core i7-3.4 PC to compute the simulations, and as shown in this figure it needs more than 700 iterations to converge. In total this optimization takes more than 9 hours and 43 minutes which is not efficient enough for a use in clinical routine. It would be worse if one needs to change some parameters and observe the difference.

Two-phase optimization in cryosurgery was used by [40] for bubble packing and force field analogy. As the optimization of the ellipsoids is fast (about a few seconds), it can restrict the search area to a smaller bound and then performing a new search with simulated iceballs in this restricted region which can lead into a more accurate results. Pattern-search method was chosen for optimizing the ellipsoids as it was successful in all the tests above. Then as shown in previous section for the hybrid methods, different optimizers can continue the search process from the best location found by the Pattern-search method.

Figure 6-11 illustrates in solid lines, trends of the second phase of optimization since the first phase using ellipsoids is fast. Direct and EA methods could converge to an objective function value of 8.3 in less than 30 iterations (25 min) while 120 iterations (100 min) were needed for SBO-trust and Solis-wets. These experiments were performed on case#4 with the vascular structure relatively far from the tumor location as shown in Figure 6-12 which has a small influence on iceball deformation. It can be predicted that the optimized ellipsoids will more or less fit the simulated iceball and a fast convergence in the second phase supports this prediction in Figure 6-11.

In contrast to case#4, a similar experiment was performed on case#3 which was chosen specifically to evaluate the effect of vessels on the number of required iterations for a similar convergence. case#3 and case#4 are taken from two different patients but in order to compare the effect of vessels on the optimization process we have chosen case#3 to have a tumor shape and size approximately similar to case#4 but located closer to the large vessels. The profile of the optimization in Figure 6-13 shows a slower performance of the same optimizers for case#3 compared to case#4, for both one-phase and two-phase algorithms: more than 2000 iterations are required by Pattern-search method in order to completely cover the tumor while only 80 iterations are needed for a two-phase

optimization to reach a good minimum. Figure 6-14 demonstrates the final solution of case#3, along with the wrong estimation of the produced ablation zone if using ellipsoids in such a case. Note that the real effect of cryoablation, represented by the blue iceball, is larger than the union of all ellipsoids, which is a known effect: the cumulated production of cold by several simultaneous sources produces a larger frozen volume than sources of cold considered separately. We can also note that in Figure 6-14 the iceball does not intersect the vessels whereas the ellipsoids do.

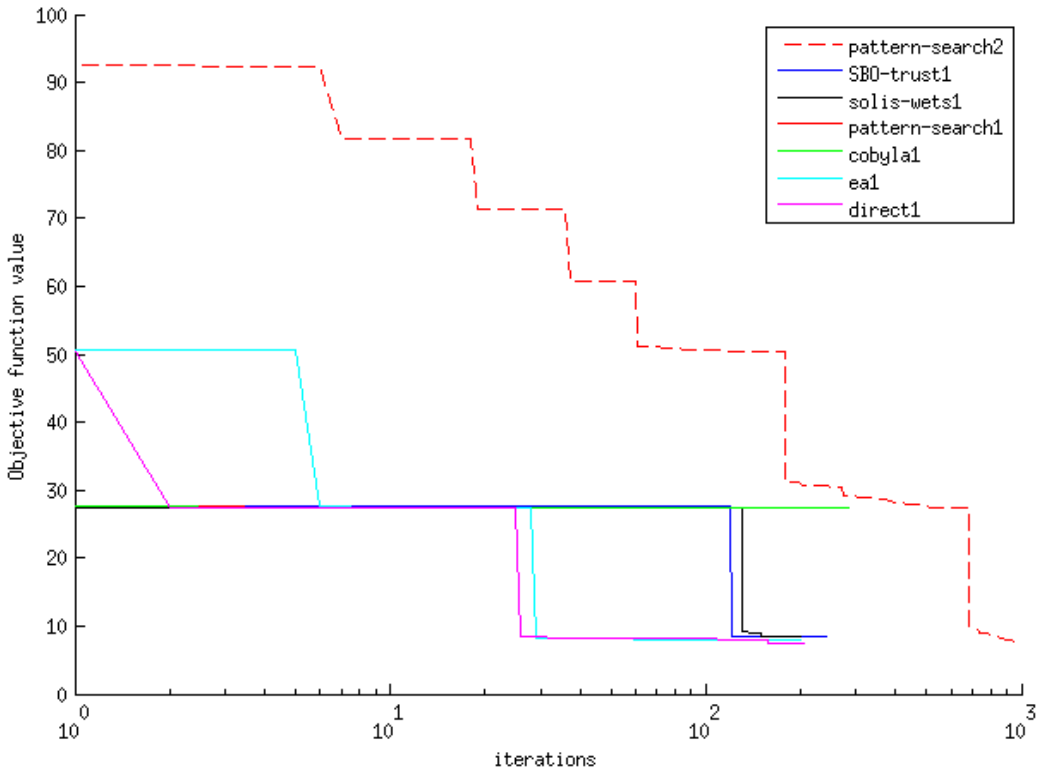

Figure 6-11 Comparison of single-phase optimization using simulated ablation zone in dashed line and several two-phase optimization methods sketched as solid lines.

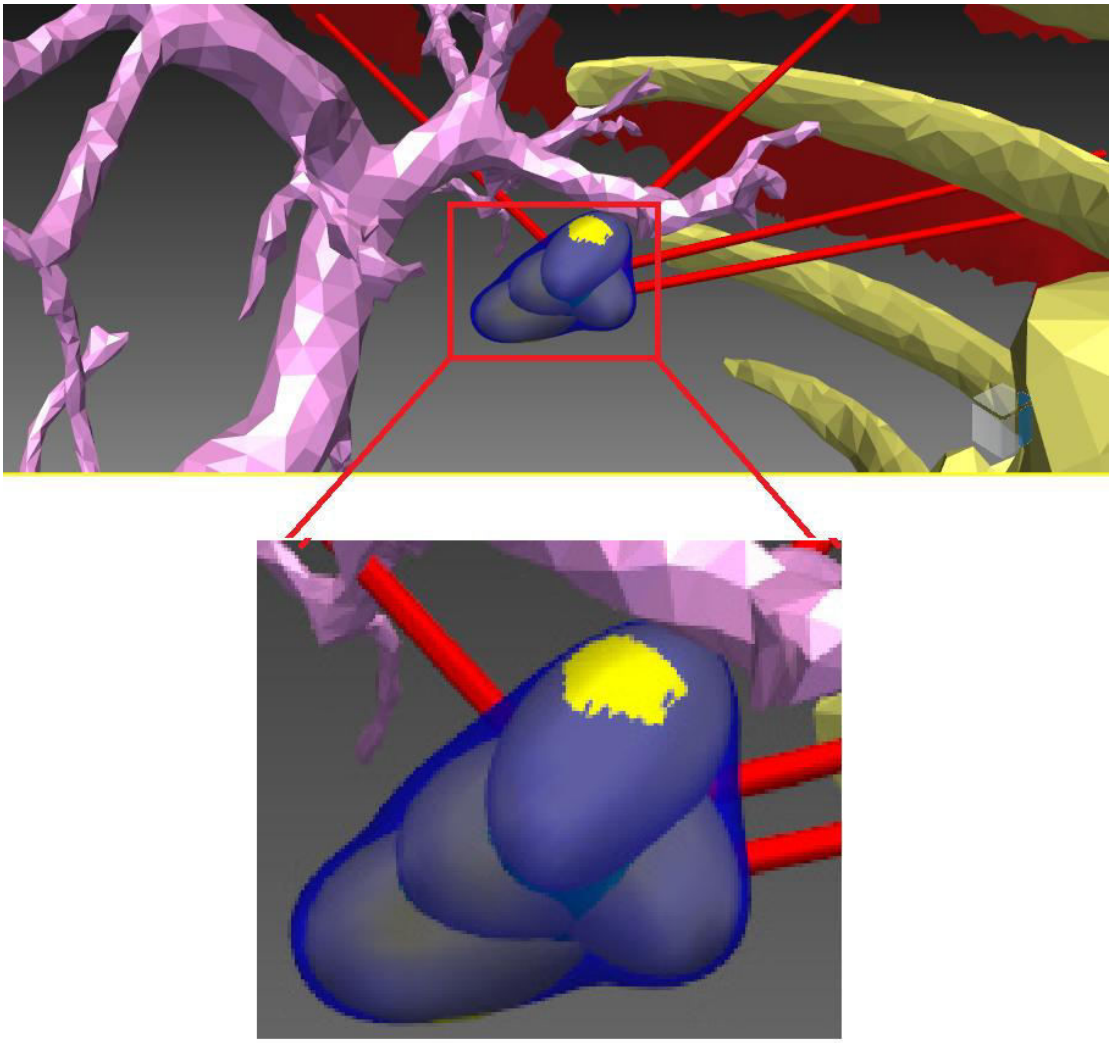

Figure 6-12 Result of planning for case#4 with a simple vascular structure close to the tumor. Ellipsoids are in yellow while simulated iceball is in semi-transparent blue.

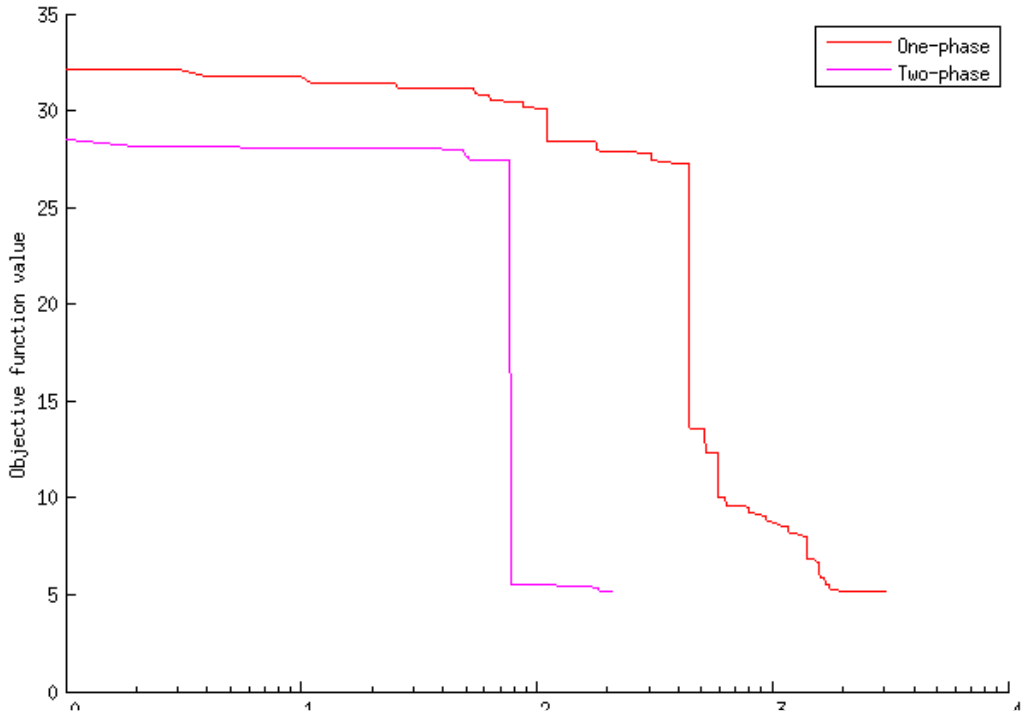

Figure 6-13 Comparison of one phase and two phase planning with a complex vascular structure close to the tumor

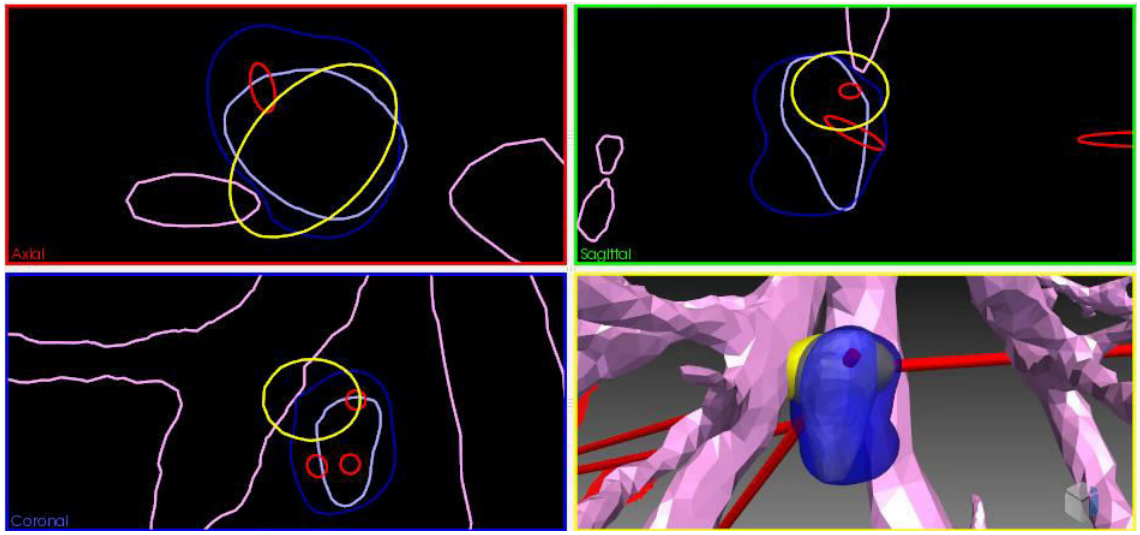

Figure 6-14 Result of planning for case#3 with a complex vascular structure close to the tumor. Iceball is in blue, tumor in gray, vessels in pink and ellipsoids in yellow.

6.5 Validation

Six optimizers were experimented in this chapter to minimize an objective function and some constraints in equation (6-15). In order to verify the accuracy of the final solutions, we propose three methods in the following.

6.5.1 Ground truth

In this planning problem, the objective function value is zero if several hard and soft constraints are met. For the hard constraints, all the trajectories should be inside the insertion zone (this covers the constraints for avoiding obstacles and tangency to the liver), needles are very close to each other, the tumor is fully covered and for the soft constraints, no region is ablated outside the tumor

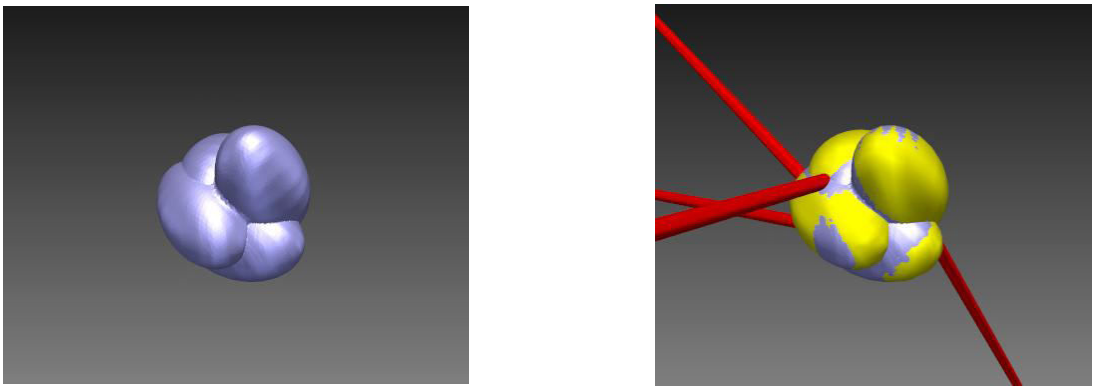

a) Synthetic tumor b) Covered parts in yellow

Figure 6-15 Synthetic tumor is specifically defined in order to validate the convergence of Pattern-search method

and all trajectories are far enough from the ribs or vessels. When choosing a tumor with a random shape, there is no guarantee that such a combination exists. Therefore, a synthetic tumor was designed using four needles placed manually in a place satisfying all these constraints and then the

aggregative mesh of their four corresponding ellipsoids was saved as a ground truth. Applying the Pattern-search method on this data converged to the value of 2.59 for the objective function and the covered tumor is illustrated in Figure 6-15. In this validation step using the ellipsoids we observed that our best method could not converge to zero for a synthetic case with a feasible best solution but still we had a good approximation of it.

6.5.2 Monte-Carlo optimization

Another way of validating the approach is to compare it to an exhaustive method. However, searching whole problem space is in order of exponential-time. As an example, when optimizing four needles each needle has 5 parameters: three translations that can be discretized at best into 20 different values, and two rotations that can be discretized into 360 different states for each direction. So in total there would be $20^{3*4} * 360^{2*4} = 1.155e^{36}$ possibilities which 4 is number of the needles. In contrast to an exhaustive method, a randomized method can be used with a polynomial-time [80]. In this part a Monte-Carlo sampling over the variable space was used to validate the convergence of case#1 with 3 needles. Case#1 is selected due to its simpler condition and less number of required samples for a good convergence. We have used two million samples for this comparison and volume computations were done using ellipsoids. The minimum objective function value found equals to 11.93 while this value for its correspondent case in Pattern-search is 11.88 and 9.32 for Solis-wets as mentioned in Table 11. This type of validation is not feasible for the planning using the simulation due to the large number of required iterations. However this method can't present a ground truth for the comparisons but extensive sampling of the variable space can override the local minimums and search into the whole domain evenly and finally presents an estimation of the best solution.

6.5.3 Surgeon planning

The goal of this part was to compare the planning chosen by the surgeon with the planning proposed by our optimization tool. This test was performed on the MSKCC dataset, where the tumor

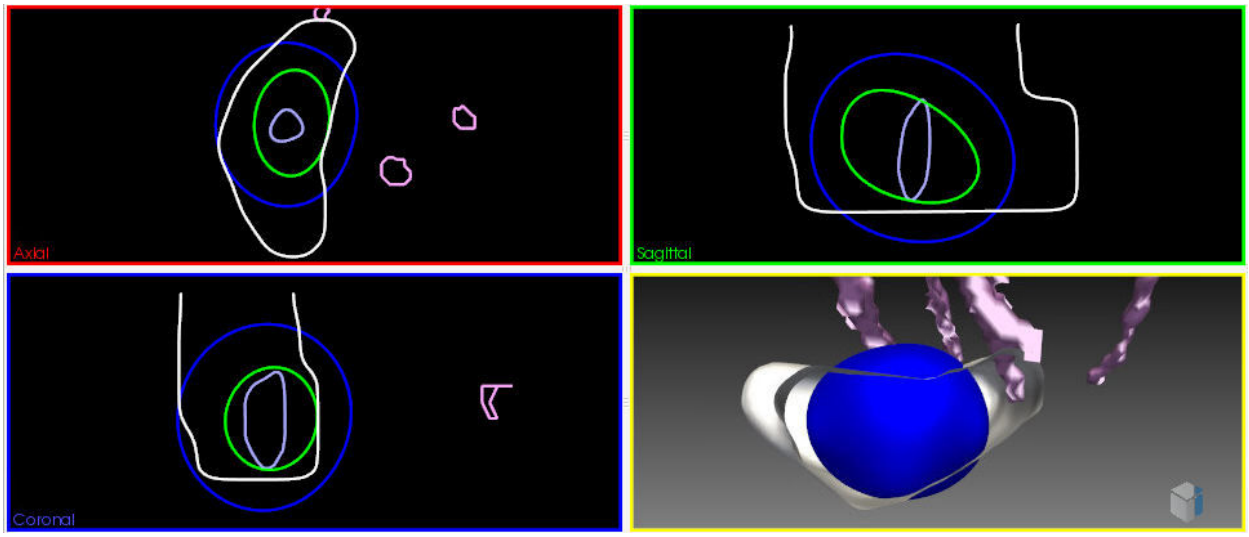

Figure 6-16 The comparison between the 0 °C iceballs in the planning tool in blue and the intra-operative images in white. Tumor in gray is completely covered by -40 °C iceball which is presented as a green surface.

was treated using two needles, and the iceball could be segmented as explained in Chapter 3. In the first place we have tried to plan the operation using only one needle but it was not successful to cover the tumor. Then, the planning was repeated with two needles as done by the surgeon. As explained in Chapter 3, only the 0°C iceball was visible in the intra-operative images so in order to make a fair comparison of the ablation zone, 0°C iceballs were compared between the planning tool and its equivalence in the intra-operative images. However, for the optimization phase the -40°C iceball was used to ensure a complete tumor necrosis. Our planning tool computes and displays three different iceballs with 0, -20 and -40°C thresholds for comparison purposes as shown in Section 4.3. Figure 6-16 shows the intra-operative iceball in white, and the simulated iceballs after a complete freezing cycle, with consideration of the vessels. In order to assess the efficiency of the planning, we computed the difference between the volumes of segmented and computed iceballs. This is a reasonable comparison since the proposed trajectories are far enough from the vessels and ribs. A smaller iceball is much safer for the patient to keep his normal tissue untouched. In this experiment, the objective was to see if our automatic planning tool was able to find a better set of trajectories, allowing for a smaller ablation while still covering the tumor entirely. This objective was reached as the iceball produced by the placement of needles we found was smaller, with a percentage of volume improvement of 31.58%.

6.6 Conclusion

In this chapter, the cryosurgical planning problem was formulated into an optimization problem. As the defined objective function and constraints were highly non-linear, discontinuous and no explicit formula was available, then several gradient-free methods were selected and experimented for the solution of this problem. The optimization problem was firstly solved only for the tumor coverage with a smoother objective function on several test functions in order of complexity. Among these selected methods, SBO-trust, Pattern-search, Solis-wets and EA could completely cover the tumor with a low number of iterations while the required number of iterations was increased by the complexity of the problem.

In another attempt, the planning problem was solved in the presence of all mentioned constraints in this thesis. By applying successive methods in a preliminary stage, only Pattern-search and in one case Solis-wets were able to satisfy the constraints, cover the tumor completely and finally decrease volume of damage to the healthy tissue. It was also shown that for the large tumor case, we need to use needles with larger iceball.

A comparison was made to show the influence of other factors like insertion zone or initial condition to the optimizer's results. If the insertion zone was more discontinuous and narrower, three different trends were observed for the optimizer's performance. In the worst case, the Solis-wets and Pattern-search methods lost their convergence found in their previous condition (but still a good convergence comparing to others) while Direct and EA could reach the same convergence as before with an increased number of iterations. SBO-trust was not affected with this change. In the initial position test, Cobyla, Solis-wets and Pattern search are completely affected when initializing needle tips outside the tumor's bounding box but the results are more robust for other methods.

Considering the results mentioned in tumor coverage and planning with all constraints, as far as keeping the needle tips inside the tumor's bounding box, we conclude that Pattern_search method was the most successful method for different tumor sizes and different shapes of the insertion zone.

In the hybrid optimization section, the idea of mixing global and local optimization methods was used to find several distinct insertion solutions and more accurate results, as shown in Section 6.4.5. The idea of proposing several solutions to the surgeon is very interesting due to different priorities and skills of each surgeon.

All the experiments mentioned above were performed using the simplified ellipsoids as the ablation zone. In the next section, the simulated iceballs discussed in chapter 4 were integrated in the optimization process instead of the ellipsoids. It was shown in Figure 6-11 that generally the number of iterations required for covering the tumor in presence of all constraints is lower due to the smoother and synergic shape of the iceballs comparing to ellipsoids but the time needed for a complete planning in this way is not feasible in practice for planning in the operating room. Therefore, a two-phase optimization method was proposed which accelerates the planning using a cheap optimization phase with ellipsoids and then by restricting the search domain continuing the optimization with simulated iceballs. Then the effect of vascularized structure on the results was shown in another test which slows down the convergence process.

Finally 3 types of validation were examined for the best solutions. First, a synthetic tumor was created using ellipsoids which constitutes a ground truth for the optimization, and the Pattern-search method could fit into the synthesized tumor with a good approximation. Another validation using Monte-Carlo sampling method was performed and showed that optimizers could have the same accuracy as a Monte-Carlo method with more than two million samples. The last experiments showed an improvement of 31.58% in preserving patient's healthy tissue compared with intra-operative images done by a skillful surgeon.

Chapter 7. Conclusion and discussion

7.1 Overview

In this chapter, first we summarize and discuss the advantages and weak points of the methods used for the cryosurgical planning throughout this manuscript and then shed light to the future paths which can be followed using the tools proposed in this work.

7.2 Conclusion and discussion

In this thesis, we combined visualization, interaction, simulation and automatic optimization in a complete approach for the assistance to preoperative planning of image-guided percutaneous cryosurgery, which has shown to improve the quality of surgical planning outcome while sparing a lot of time to the surgeon. Thanks to a generic design, the software has the possibility to be extended to a wider range of surgical rules or even other trajectory based interventions, in addition to its already existing applications like cryosurgery, RFA and DBS.

The main goal was to find a fast and accurate solution to apply in the operation room. For the sake of accuracy, bio-heat propagation was carefully solved considering most of the heat sink effects in its surroundings. Metabolic heat, blood perfusion and large vessel's convective effect were investigated and the amount of deformations relative to distance to the vessels have been studied. Then validations using manufacturer's available data for a standard cryosurgery procedure and intra-operative images for one and two needles were performed.

For the planning phase, and with a surgeon's consultation, several constraints were adapted to mimic the surgeon's concerns during the operation. Some of the constraints were applied in a pre-processing step while others were handled by penalty functions. After the formulation of the planning problem, several optimization methods were experimented to find the best solutions and to find a good minimum. In order to compare the optimizers in practice, six patient cases were used and the performances of the different optimizers were evaluated, regarding initial points and complexity of the objective function.

Let us note the well-known global method of Simulated annealing was absent from our experiments related in this thesis. In a preliminary study that we did not include in this manuscript, we implemented in MATLAB[7] a comparison of several optimization methods like Pattern search, Surrogate modeling, EA, Multi-level Coordinate Search (MCS) and Simulated annealing, only applied to the tumor coverage problem, in order to have a first idea of their convergence on this specific

[7] https://www.mathworks.com/products/matlab/

problem, before testing them on larger datasets and more complicated conditions. Among these methods Pattern_search, Surrogate modeling, EA and Simulated annealing demonstrated fast and accurate results. However Simulated annealing method was later substituted with Solis-wets method due to the difficulty of setting appropriate parameters, which has to be specific to each case. We estimated that it would not be convenient in practice to use this method in further developments if it requires a long process of parameters adjustments by the surgeon for each new patient. Our preliminary study was published in [81], to which we refer the reader for more details. This paper is also included as Appendix 1.

We found that methods like Direct and Cobyla were not suitable for problems with highly non-linear objective function and got easily stuck in local minima. Stochastic methods like Solis-wets, EA and adaptive Pattern-search method can overcome these issues and reach a good minimum. The dimensionality of the problem and non-smoothness of the objective function due to the shape of the insertion zone were found to rapidly increase the complexity of the search domain and decrease the performances of all optimizers.

As discussed in Section 6.6 as far as the needle tips are placed inside the tumor, Pattern_search proved to have better results and was able to find a good minimum for most of the tested tumor sizes and insertion zone shapes. It was shown in Sections 6.4.1 and 6.4.2 that the surrogate optimization method had interesting results for the tumor coverage. Comparing to other successful methods it was fast, accurate and robust due to initial point changes while it failed after introducing the rest of the constraints or by adding non-linear constraints.

The response of the surrogate modeling method to the complexity of the objective function depends on its interpolation method. Some methods like low order polynomials and radial basis are only accurate in a small region when the objective function is highly nonlinear [82] and it was shown in the literature that Kriging interpolation method was more appropriate for such an objective function and could lead to a better convergence [83, 84]. We also tried different interpolation methods in our preliminary tests and finally chosen Kriging interpolator as the most accurate while it is the main reason for computational cost of the surrogate modeling optimization.

The internal computations for all the optimization methods are negligible except for the surrogate based optimization method. With this method, at each iteration a low-fidelity model should be generated using a specific interpolation. The time required for the interpolation is related to the number of variables. An average computational time for internal operations is presented in Table 16. As opposed to local surrogate method used in the previous chapter, global surrogate optimization updates its low fidelity model each time a true function is evaluated. In a preliminary study the performance of global and local surrogate methods were compared which convinced us to omit the global method due to its similar performance and long computational time.

In order to deal with computation time related considerations, three different modes of automatic planning were introduced. In the fastest way, simplified ellipsoids are used to completely cover the tumor while avoiding the hard constraints like the obstacles, needle crossing and tangency. If such a solution exists, the optimizer starts to minimize the volume of damaged healthy tissue and make sure that trajectories are far enough from the ribs and vessels. This method is fast, but the accuracy

of the tumor coverage with a complex vascular system in its proximity is not ensured but it is too beneficial when the tumor is located far from the vessels. Integrating simulated iceballs in the optimization process solved this problem at the cost of huge computational time. Therefore in a third approach, we introduced a two-phase method benefiting from fast ellipsoids and accurate simulated iceballs methods, able to be used in complex vascularized environments.

Table 16 Average time required for the computation of interpolations in each iteration of local surrogate modeling depending on the number of variables

# of variables	3 needles/ 18 var	4 needles/ 24 var	7 needles/ 42 var
Average time (s)	5.31	7.48	13.35

The hybrid optimization we propose to combine the benefits of global and local optimization in a reasonable time could converge to a lower minimum and also permitted us to present up to 6 different possible strategies to the surgeon, all 6 having an interesting quality. We think that the possibility for the surgeon to have not only one proposed solution but a set of alternatives is particularly important, as surgeons can have different skills and concerns, or some other factors might not have been taken into account in the solver yet, and could prevent the surgeon from executing one specific strategy.

The last experiment in Section 6.4.1 demonstrated that the selection of the type of cryoprobe depended on the tumor size and its position related to the other organs. In all of the experiments the smallest type of cryoprobe was selected in order to compare the performance of optimizers in a particularly difficult situation. Moreover, comparing to cryoprobes with larger ablation effects, the smaller ones are associated with a lower risk of bleeding and other complications [85]. When choosing small cryoprobes, multiple needles are required to ablate the tumor completely, which increases the efficiency of freezing by enlarging the surface of the coldest isotherm [86].

Finally based on the observation of the results, we estimate that it would be very difficult to treat tumors larger than 5 cm^3 due to the growing number of needles which is compatible with other clinical studies in this field [85, 87]. Practical feasibility of operations and increasing complexity of the planning for a large number of needles are among these reasons. Moreover, using very large needles are not recommended and can cause post-operative complications [87].

7.3 Future works

There exists several short term and long term perspectives in this work. As mentioned before, for a planning problem if we propose several distinct solutions, then visualizing all these possible sets of needles at once remains a challenge. A simple way would be to show them sequentially. Another idea could be to navigate within solutions guided by a user interaction. In this method all needles would be labeled and one of them chosen as the pivot needle. In the visualization step only pivot needles would be shown and the other needles appear only if their corresponding pivot is selected. Another visualization technique can be proposed for a semi-automatic planning of multiple needles. In this method after a first automatic proposition of needle placements, trajectories are displaced or rotated one by one in an interactive manner. In this step a color map would be sketched around the

selected needle to show the value of objective function for its neighborhood points on the skin.

In this manuscript the results of the automatic trajectory planning was compared with the intra-operative images of one patient but it would be very interesting to continue this retrospective validation in order to compare the results in different conditions and validate the robustness of the method more thoroughly. It would also be interesting to compare the outcome of surgeries from surgeons with different levels of expertise or clinical sites. This would result in a better assessment of automatic planning improvement compared to manual planning, and reveal how beneficial it would be in practice.

In this thesis, we used an aggregative approach based on several objective functions combined with a weighting criterion that allow producing simplified results. A different problem formulation based on a multiple-objective optimization and the computation of the whole set of Pareto-optimal solutions would be interesting in the future, as it could propose at once all solutions that can be considered as optimal regardless of the weighting. Therefore it would not be required to choose predefined weights for risk functions in Equation (6-4). However, the possibly large number of sets of trajectories that would have to be visualized would induce some visual overload issues and a study of an ergonomic presentation of the possible solutions would have to be carried out.

During the intervention, patients are positioned on their back or stomach which leads to an extra constraint on the placement of multiple needles that has not been taken into account so far. Solutions including trajectories that should be inserted through the back while others should be inserted from the front would have to be rejected. This constraint was not considered yet in our solver but a solution for this problem would be to constrain all needles to be in within a maximum angle under a threshold. This angle could be quite large, like 90 degrees for instance in the case of a manual insertion of the needles, for which we can imagine that some needles could be inserted through the side of the patient while others are inserted through the front or back. However we can also have in sight a coupling of our planning software with a robotic system in the future, which would probably be more constrained in the positioning of multiple needles and require a smaller angle.

Next, for improving the performance of surrogate based algorithm in presence of all constraints, a method proposed by Villanueva et al. can be implemented in our solver. They utilized multi-agent surrogates to handle nonlinear constraints as described in [88].

Apart from the coupling with a robotic system as we already mentioned, some other long term perspectives of our work can be proposed: coupling with an AR system for needle guidance; using intra-operative ultrasound images for a realtime registration of the liver to pre-operative high resolution MRI images and planning based on new deformed organs; integration of deformable needles for the multiple trajectory planning.

References

1. Rohen, J.W., C. Yokochi, and E. Lütjen-Drecoll, *Color atlas of anatomy: a photographic study of the human body*. 2006: Schattauer Verlag.
2. Yaniv, Z., et al., *Needle-based interventions with the image-guided surgery toolkit (IGSTK): from phantoms to clinical trials.* Biomedical Engineering, IEEE Transactions on, 2010. **57**(4): p. 922-933.
3. Fedorov, A., et al., *3D Slicer as an image computing platform for the Quantitative Imaging Network.* Magnetic resonance imaging, 2012. **30**(9): p. 1323-1341.
4. Gage, A.A. and J. Baust, *Mechanisms of tissue injury in cryosurgery.* Cryobiology, 1998. **37**(3): p. 171-186.
5. Acker, J.P., J.A. Elliott, and L.E. McGann, *Intercellular ice propagation: experimental evidence for ice growth through membrane pores.* Biophysical journal, 2001. **81**(3): p. 1389-1397.
6. Muldrew, K. and L.E. McGann, *The osmotic rupture hypothesis of intracellular freezing injury.* Biophysical journal, 1994. **66**(2): p. 532-541.
7. Karlsson, J.O., E.G. Cravalho, and M. Toner, *Intracellular ice formation: causes and consequences.* Cryo-Letters, 1993. **14**: p. 323-334.
8. Toner, M., E.G. Cravalho, and M. Karel, *Thermodynamics and kinetics of intracellular ice formation during freezing of biological cells.* Journal of Applied Physics, 1990. **67**(3): p. 1582-1593.
9. Seitel, A., et al., *Computer-assisted trajectory planning for percutaneous needle insertions.* Medical physics, 2011. **38**(6): p. 3246-3259.
10. Baegert, C., et al., *Trajectory optimization for the planning of percutaneous radiofrequency ablation of hepatic tumors.* Computer Aided Surgery, 2007. **12**(2): p. 82-90.
11. Young, J.L., et al., *Are multiple cryoprobes additive or synergistic in renal cryotherapy?* Urology, 2012. **79**(2): p. 484. e1-484. e6.
12. TERRY, S., A.T. ILCHIK, and P.A.G. KENNETH. *Complications of hepatic cryosurgery*. in *Seminars in surgical oncology*. 1998.
13. Rieder, C., et al., *GPU-based real-time approximation of the ablation zone for radiofrequency ablation.* Visualization and Computer Graphics, IEEE Transactions on, 2011. **17**(12): p. 1812-1821.
14. Schumann, C., et al., *State of the art in computer-assisted planning, intervention, and assessment of liver-tumor ablation.* Critical Reviews™ in Biomedical Engineering, 2010. **38**(1).
15. Butz, T., et al. *Pre-and intra-operative planning and simulation of percutaneous tumor ablation*. in *Medical Image Computing and Computer-Assisted Intervention–MICCAI 2000*. 2000. Springer.
16. Villard, C., L. Soler, and A. Gangi, *Radiofrequency ablation of hepatic tumors: simulation, planning, and contribution of virtual reality and haptics.* Computer Methods in Biomechanics and Biomedical Engineering, 2005. **8**(4): p. 215-227.
17. Rieder, C., et al. *Visualization of risk structures for interactive planning of image guided radiofrequency ablation of liver tumors*. in *SPIE Medical Imaging*. 2009. International Society for Optics and Photonics.
18. Mulier, S., et al., *Experimental and clinical radiofrequency ablation: proposal for standardized description of coagulation size and geometry.* Annals of surgical oncology, 2007. **14**(4): p. 1381-1396.
19. http://www.med.unc.edu/. *Deep-brain-stimulation*. 2014.
20. Weinbaum, S. and L. Jiji, *A new simplified bioheat equation for the effect of blood flow on local average tissue temperature.* Journal of biomechanical engineering, 1985. **107**(2): p. 131-139.
21. Nakayama, A. and F. Kuwahara, *A general bioheat transfer model based on the theory of porous media.* International Journal of Heat and Mass Transfer, 2008. **51**(11): p. 3190-3199.
22. Bischof, J.C., et al., *Cryosurgery of dunning AT-1 rat prostate tumor: thermal, biophysical, and viability response at the cellular and tissue level.* Cryobiology, 1997. **34**(1): p. 42-69.
23. Deng, Z.-S. and J. Liu, *Modeling of multidimensional freezing problem during cryosurgery by the dual reciprocity boundary element method.* Engineering Analysis with Boundary Elements, 2004. **28**(2): p. 97-108.
24. Weill, A., A. Shitzer, and P. Bar-Yoseph, *Finite element analysis of the temperature field around two adjacent cryo-probes.* Journal of biomechanical engineering, 1993. **115**(4A): p. 374-379.
25. Rabin, Y. and A. Shitzer, *Numerical solution of the multidimensional freezing problem during cryosurgery.* Journal of biomechanical engineering, 1998. **120**(1): p. 32-37.
26. Rewcastle, J.C., et al., *A model for the time dependent three-dimensional thermal distribution within iceballs surrounding multiple cryoprobes.* Medical Physics, 2001. **28**(6): p. 1125-1137.
27. Zhang, Y.-T. and J. Liu, *Numerical study on three-region thawing problem during cryosurgical re-warming.* Medical engineering & physics, 2002. **24**(4): p. 265-277.

28. Wan, R., et al., *A finite element model for ice ball evolution in a multi-probe cryosurgery.* Computer methods in biomechanics and biomedical engineering, 2003. **6**(3): p. 197-208.
29. Baissalov, R., et al., *Simultaneous optimization of cryoprobe placement and thermal protocol for cryosurgery.* Physics in medicine and biology, 2001. **46**(7): p. 1799.
30. Deng, Z.-S. and J. Liu, *Numerical simulation of 3-D freezing and heating problems for combined cryosurgery and hyperthermia therapy.* Numerical Heat Transfer, Part A: Applications, 2004. **46**(6): p. 587-611.
31. Kolios, M., M. Sherar, and J. Hunt, *Large blood vessel cooling in heated tissues: a numerical study.* Physics in Medicine and Biology, 1995. **40**(4): p. 477.
32. Blanchard, C., et al., *Hybrid finite element-finite difference method for thermal analysis of blood vessels.* International journal of hyperthermia, 2000. **16**(4): p. 341-353.
33. Talbot, H., et al. *Interactive Planning of Cryotherapy Using Physically-Based Simulation*. in *MMVR 21-Medicine Meets Virtual Reality-2014*. 2014.
34. Ahuja, A. and W. Hendee, *Thermal design of a heat exchanger for heating or cooling blood.* Physics in medicine and biology, 1978. **23**(5): p. 937.
35. Keanini, R. and B. Rubinsky, *Optimization of multiprobe cryosurgery.* Journal of heat transfer, 1992. **114**(4): p. 796-801.
36. Bonacina, C., et al., *Numerical solution of phase-change problems.* International Journal of Heat and Mass Transfer, 1973. **16**(10): p. 1825-1832.
37. Baissalov, R., et al., *A semi-empirical treatment planning model for optimization of multiprobe cryosurgery.* Physics in Medicine and Biology, 2000. **45**(5): p. 1085.
38. Lung, D.C., T.F. Stahovich, and Y. Rabin, *Computerized planning for multiprobe cryosurgery using a force-field analogy.* Computer Methods in Biomechanics and Biomedical Engineering, 2004. **7**(2): p. 101-110.
39. Lung, D.C. and T.F. Stahovich, *Computerized planning of cryosurgery using cryoprobes and cryoheaters.* Technology in cancer research & treatment, 2004. **3**(3).
40. Tanaka, D., K. Shimada, and Y. Rabin, *Two-phase computerized planning of cryosurgery using bubble-packing and force-field analogy.* Journal of biomechanical engineering, 2006. **128**(1): p. 49-58.
41. Tanaka, D., et al., *Cryosurgery planning using bubble packing in 3D.* Computer methods in biomechanics and biomedical engineering, 2008. **11**(2): p. 113-121.
42. Rossi, M.R., et al., *Computerized planning of cryosurgery using bubble packing: An experimental validation on a phantom material.* International journal of heat and mass transfer, 2008. **51**(23): p. 5671-5678.
43. Rossi, M.R., et al., *Computerized planning of prostate cryosurgery using variable cryoprobe insertion depth.* Cryobiology, 2010. **60**(1): p. 71-79.
44. Giorgi, G., et al., *An optimization approach to multiprobe cryosurgery planning.* Cryobiology, 2011. **63**(3): p. 315.
45. Socha, K. and M. Dorigo, *Ant colony optimization for continuous domains.* European journal of operational research, 2008. **185**(3): p. 1155-1173.
46. Littmann, A., et al. *Planning of anatomical resections and in situ ablations in oncologic liver surgery*. in *International Congress Series*. 2003. Elsevier.
47. Villard, C., et al., *Virtual radiofrequency ablation of liver tumors*, in *Surgery Simulation and Soft Tissue Modeling*. 2003, Springer. p. 366-374.
48. Villard, C., et al. *Toward realistic radiofrequency ablation of hepatic tumors 3D simulation and planning*. in *Medical Imaging 2004*. 2004. International Society for Optics and Photonics.
49. Villard, C., et al., *Optimal trajectories computation within regions of interest for hepatic RFA planning*, in *Medical Image Computing and Computer-Assisted Intervention–MICCAI 2005*. 2005, Springer. p. 49-56.
50. Baegert, C., et al., *Multi-criteria trajectory planning for hepatic radiofrequency ablation*, in *Medical Image Computing and Computer-Assisted Intervention–MICCAI 2007*. 2007, Springer. p. 676-684.
51. Baegert, C., et al. *Precise determination of regions of interest for hepatic rfa planning*. in *Medical Imaging*. 2007. International Society for Optics and Photonics.
52. Wolf, I., et al., *The medical imaging interaction toolkit.* Medical image analysis, 2005. **9**(6): p. 594-604.
53. Schumann, C., et al. *Fast automatic path proposal computation for hepatic needle placement*. in *Proceedings of SPIE*. 2007.
54. Kröger, T., et al., *Fast estimation of the vascular cooling in RFA based on numerical simulation.* The open biomedical engineering journal, 2010. **4**: p. 16.
55. Rieder[1], C., et al., *Interactive Approximation of the Ablation Zone incorporating Heatsink Effects for Radiofrequency Ablation.* 2010.

56. Trovato, K., et al. *Automated RFA planning for complete coverage of large tumors*. in *SPIE Medical Imaging*. 2009. International Society for Optics and Photonics.
57. Ren, H., et al., *Coverage planning in computer-assisted ablation based on Genetic Algorithm.* Computers in biology and medicine, 2014. **49**: p. 36-45.
58. Brunenberg, E.J., et al., *Automatic trajectory planning for deep brain stimulation: a feasibility study*, in *Medical Image Computing and Computer-Assisted Intervention–MICCAI 2007*. 2007, Springer. p. 584-592.
59. Essert, C., et al., *Automatic computation of electrode trajectories for Deep Brain Stimulation: a hybrid symbolic and numerical approach.* International journal of computer assisted radiology and surgery, 2012. **7**(4): p. 517-532.
60. Pennes, H.H., *Analysis of tissue and arterial blood temperatures in the resting human forearm.* Journal of applied physiology, 1948. **1**(2): p. 93-122.
61. Rubinshteĭn, L., *The stefan problem*. Vol. 27. 1971: American Mathematical Soc.
62. Rote, G., *Computing the minimum Hausdorff distance between two point sets on a line under translation.* Information Processing Letters, 1991. **38**(3): p. 123-127.
63. Dice, L.R., *Measures of the amount of ecologic association between species.* Ecology, 1945. **26**(3): p. 297-302.
64. Yang, X.-S., *Introduction to computational mathematics*. 2008: World Scientific.
65. Yang, X.-S., *Engineering optimization: an introduction with metaheuristic applications*. 2010: John Wiley & Sons.
66. Wolpert, D.H. and W.G. Macready, *No free lunch theorems for optimization.* Evolutionary Computation, IEEE Transactions on, 1997. **1**(1): p. 67-82.
67. Nelder, J.A. and R. Mead, *A simplex method for function minimization.* The computer journal, 1965. **7**(4): p. 308-313.
68. Kirkpatrick, S., C.D. Gelatt, and M.P. Vecchi, *Optimization by simmulated annealing.* science, 1983. **220**(4598): p. 671-680.
69. Kennedy, J. and R. Eberhart, *particle swarm optimization, proceedings of IEEE International Conference on neural networks (ICNN'95)*. 1995.
70. Goldberg, D.E. and J. Richardson. *Genetic algorithms with sharing for multimodal function optimization*. in *Genetic algorithms and their applications: Proceedings of the Second International Conference on Genetic Algorithms*. 1987. Hillsdale, NJ: Lawrence Erlbaum.
71. Holand, J.H., *Adaptation in natural and artificial systems.* Ann Arbor: The University of Michigan Press, 1975.
72. Yang, X.-S., *Nature-inspired metaheuristic algorithms*. 2010: Luniver press.
73. Talbi, E.-G., *Metaheuristics: from design to implementation*. Vol. 74. 2009: John Wiley & Sons.
74. Forrester, A.I. and A.J. Keane, *Recent advances in surrogate-based optimization.* Progress in Aerospace Sciences, 2009. **45**(1): p. 50-79.
75. Deb, K., *Optimization for engineering design: Algorithms and examples*. 2012: PHI Learning Pvt. Ltd.
76. Reklaitis, G., A. Ravindran, and K. Ragsdell, *Engineering Optimization Methods and Applications. 1983*. Wiley, New York.
77. Nocedal, J. and S.J. Wright, *Numerical Optimization 2nd.* 2006.
78. Avriel, M., *Nonlinear programming: analysis and methods*. 2003: Courier Dover Publications.
79. Rios, L.M. and N.V. Sahinidis, *Derivative-free optimization: A review of algorithms and comparison of software implementations.* Journal of Global Optimization, 2013. **56**(3): p. 1247-1293.
80. Sen, S.K. and G.A. Shaykhian, *Exhaustive versus randomized searches for nonlinear optimization in 21st century computing: solar application.* Neural, Parallel and Scientific Computations, 2010. **18**(3): p. 487.
81. Jaberzadeh, A. and C. Essert, *Multi-probe three-dimensional placement planning for liver cryosurgery: comparison of different optimization methods.* proceedings of 14th International Conference Computational and Mathematical Methods in Science and Engineering, 2014. **III**: p. 743-754.
82. Meckesheimer, M., et al., *Metamodeling of combined discrete/continuous responses.* AIAA journal, 2001. **39**(10): p. 1950-1959.
83. Simpson, T.W., et al., *Kriging models for global approximation in simulation-based multidisciplinary design optimization.* AIAA journal, 2001. **39**(12): p. 2233-2241.
84. Simpson, T.W., *Comparison of response surface and kriging models in the multidisciplinary design of an aerospike nozzle.* 1998.
85. CESTARI, A., et al., *Laparoscopic cryoablation of solid renal masses: intermediate term followup.* The Journal of urology, 2004. **172**(4): p. 1267-1270.
86. Park, M.G., S.H. Kang, and J. Cheon, *The initial experience with 3rd generation nephron-sparing cryoablation for renal tumor.* Korean Journal of Urology, 2007. **48**(4): p. 363-370.

87. Ham, B.K., et al., *The impact of renal tumor size on the efficacy of laparoscopic renal cryoablation.* Korean journal of urology, 2010. **51**(3): p. 171-177.
88. Villanueva, D., et al. *Surrogate-based agents for constrained optimization*. in *14th AIAA Non-Deterministic Approaches Conference, Honolulu, AIAA Paper*. 2012.

Appendix 1

In the following pages, paper referenced in [81] is reproduced.

- Jaberzadeh, A. and C. Essert, *Multi-probe three-dimensional placement planning for liver cryosurgery: comparison of different optimization methods.* proceedings of 14th International Conference Computational and Mathematical Methods in Science and Engineering, 2014. **III**: p. 743-754.

Multi-probe three-dimensional placement planning for liver cryosurgery: comparison of different optimization methods

Amir Jaberzadeh[1] **and Caroline Essert**[1]

[1] *ICUBE, Université de Strasbourg, CNRS, France*

emails: ahjaberzadeh@unistra.fr, essert@unistra.fr

Abstract

Pre-operative planning of percutaneous thermal ablations is a difficult but decisive task for a safe and successful intervention. The purpose of our research is to assist surgeons in preparing cryoablations with an automatic pre-operative path planning algorithm able to propose a placement for multiple needles in 3D. The aim is to optimize several surgical constraints while taking into account a precise computation of the frozen area. Using an implementation of the precise estimation of the iceballs, this study focuses on the optimization in an acceptable time of multiple probes positions with 6 degrees of freedom, regarding the constraint of optimal volumetric coverage of the tumor by the combined necrosis. Pennes equation was used to solve the propagation of cold within the tissues, and included in an objective function of the optimization process. The propagation computation being time-consuming, six optimization algorithms from the literature were experimented under different conditions and compared, in order to reduce overall computation time while preserving precision. Some of them were found suitable for the conditions of our cryosurgery planning. We conclude that this combination of bioheat simulation and optimization can be appropriate for a use by practitionners in acceptable conditions of time and precision.

Key words: Surgery planning, Derivative free optimization, Bioheat simulation

1 Introduction

Minimally invasive surgery has known an increasing interest in the past decades. The small size of incisions is beneficial to patients by decreasing the discomfort as well as the time required for recovery compared to conventional surgery, all with the same benefits. Percutaneous cryoablation is a good example, in which the cancerous tissue is frozen using one or multiple needles. During this procedure, tissue temperature drops to -40℃ around needle tip, which is lethal for cells included in the iceball volume. The final goal of cryotherapy is the necrosis of cancerous cells while preserving surrounding healthy tissue and avoiding

damages to vital anatomical structures. For this purpose, an accurate surgical planning needs to be done beforehand by surgeons.

However, the non-invasive, real-time monitoring of three-dimensional isotherm surface of this critical temperature within the tissue during cryosurgical procedures has remained a challenge. Since temperature can be measured only at discrete points in the target region, simulation of heat transfer is an extremely useful tool to estimate the real coverage for a candidate probe placement. A number of models has been proposed to solve the bioheat propagation equation in two and three dimensions.

An important parameter in cryosurgery planning is the optimal choice of cryoprobes locations with specific shapes and dimensions. It is typically done in a trial-and-error task to find the best configuration. Since the manufactured cryoprobes have been produced with a limited set of active lengths and diameters, and freezing protocol is commonly fixed, other cryosurgical parameters such as number of cryoprobes and cryoprobe placement are good candidates for optimization and planning during the procedure.

The overall objective of our research is to provide the surgeon with an automatic pre-operative path planning algorithm able to propose a placement for multiple needles in 3D, taking into account several surgical constraints as well as a precise computation of the frozen area. In this paper, we focus on the optimization of the tridimensionnal placement of multiple iceballs around the tumor to cover it at best. We first explain the implementation of the accurate simulation of the propagation of cold within the tissues. This simulation being a time-consuming process, we compare several optimization approaches under different conditions, to find the most suitable in terms of compromise between speed and accuracy, to be able to propose to the surgeon a good positionning strategy in a reasonable time.

2 Context

2.1 Related works

The problem of cryosurgery optimization was first addressed by Keanini and Rubinsky [1] using simplex method. The heat transfer equation was solved for a 3D domain with finite-difference method. Authors optimized only the number of cryoprobes and their geometrical dimensions (diameter and active length), but optimization of other parameters, such as cryoprobe placement in the target tissue and their thermal protocol, seems to be more practical. They used an idealized model and geometry for urethral warmer, prostate, bladder and rectum. In 2001 Baissalov et al. [2] studied simultaneous optimization of cryoprobe placement and thermal simulation using a gradient descent algorithm called L-BFGS-B method. They described a 3D solution based on the cumulative 2D transverse planes, but the shown results were only for 2D state in a prostate model.

Tanaka and Rubin [3] used a mechanical based method to solve the problem of cryoprobe optimization in two phases. Phase I called bubble-packing starts with generating ellipsoidal

elements (or bubbles) inside planning domain, then van der Waals'-like forces are simulated to move these bubbles until a minimum-force configuration is found. A single bioheat simulation is executed at the end of Phase I. The simulation is terminated at the point at which a minimum defect region is found for that particular layout. In phase II, a bioheat equation is solved and a new set of forces on the cryoprobes are computed based on the defect region and one or more cryoprobes are moved accordingly. This survey was done in 2D for the prostate while in 2008, the same team extended their work to 3D [4] but just for bubble packing method.

Giovanni et al. [5] used Ants Colony (ACO) to choose the optimal parameter configurations. Computation of the cost function is based on the numerical solution of several direct Stefan problems solved by a Euler-Galerkin approach. This method combines a finite difference approximation of the time-derivative and a finite element approach solving the space-dependent part of the differential problem. This study was done on a 2D standard prostate phantom.

2.2 Problem statement

As mentioned above all previous studies were done for prostate cryosurgery in which needles are placed in the same direction and consequently number of optimization variables is reduced. In this paper the first goal is to deal with a general case in which planning domain could be 3D and needles have 6 degrees of freedom: 3 translations for position and 3 rotations for orientation.

Previous studies have computed bioheat propagation in order to have a more realistic simulation of cryosurgery procedure. Bioheat propagation in the tissue is affected by needle parameters, time and surrounding tissues. An interesting source of bioheat is the flowing blood within large adjacent vessels which can cause a "heat sink" effect and may prevent temperature from decreasing to lethal levels. This may result in inadequate ablation, thus increasing the risk of tumor recurrence in this region. Our second objective is to consider surrounding tissues which have an important role in forming the final frozen region inside the bioheat equation computation.

Our problem of simultaneous optimization of thermal protocol and cryoprobe placement requires handling a large number of bound constrained optimization variables and ability to minimize an objective function that cannot be expressed analytically in terms of the optimization variables.

High computational cost of bioheat equation in each iteration requires a fast converging optimization method for real time purposes. Optimization algorithms have been studied in the literature to find the most suitable ones in terms of convergence and computational time while avoiding local minima. Among the optimization techniques, we experimented various techniques in order to compare them in the conditions of our problem: local optimization methods such as Generating Set Search(GSS), and global optimization methods such as

Genetic Algorithm(GA), Simulated Annealing(SA), Multilevel Coordinate Search (MCS), Surrogate Modeling (SM) and evolutionary strategy (ES) were tested. Our final goal is to optimize trajectories positions quickly and precisely, while taking into account a realistic simulation of the formation of iceballs.

3 Material and Method

3.1 Numerical computation of the bioheat transfer within the tissues

The thermal distribution outcome of the cryosurgical procedure is predicted using multi-probe thermal simulations. Results of the simulations are quantified in terms of isotherm locations at any given time with respect to anatomy and the value of the objective function in the optimization scheme. These tools provide a means of assessing effectiveness of the treatment. Our method consists of a time-dependent model of iceball formation based on bioheat transfer equation around the needle tip, taking into account major vessels surrounding the frozen area that influence the freezing process. Most of the theoretical analysis on heat transfer in living tissue are originated from the Pennes equation [6], which describes the influence of blood flow on the temperature distribution in the tissue in terms of volumetrically distributed heat sinks or sources.

This uniform energy equation for biological tissue which can be applied to frozen, partially frozen and unfrozen tissue regions, can be written as:

$$\tilde{C}\frac{\partial T(X,t)}{\partial t} = \nabla.\tilde{k}\nabla[T(X,t)] - \tilde{\omega}_b C_b T(X,t) + \tilde{Q}_m + C_b\tilde{\omega}_b T_a \quad X \in \Omega(t) \tag{1}$$

where $\tilde{C}$ is the effective heat capacity; $\tilde{k}(T)$ is the effective thermal conductivity; $\tilde{Q}_m$ is the effective metabolic heat generation; $\tilde{w}_b(T)$ is the effective blood perfusion; T_a is the arterial temperature; C_b is the heat capacity of blood; X contains the Cartesian coordinates x, y , and z; $T(X,t)$ is the temperature of tissue; $\Omega(t)$ denotes the domain at time t. The description and derivation of this coefficients in different states are omitted here for brevity. A finite difference algorithm is applied to solve this complex problem with phase change heat transfer in biological tissues. Applying this formulation to Eq 1 and using the following relation to express the linear term $T(X,t)$ on the right side of Eq 1,

$$T(X,t) = \beta T(X,t+\Delta t) + (1-\beta)T(X,t) \tag{2}$$

where β is a relaxation factor, and $0 \leq \beta \leq 1$, Eq 1 can be discretized as follows:

$$\begin{aligned} T(X,t+\Delta t) =& \frac{1-W(1-\beta)\Delta t - m.Fo}{1+W\beta\Delta t}T(X,t) + \Sigma_{i=1}^{\frac{m}{2}}\frac{Fo}{1+W\beta\Delta t}T(X+\Delta x_i,t) \\ &+ \Sigma_{i=1}^{\frac{m}{2}}\frac{Fo}{1+W\beta\Delta t}T(X-\Delta x_i,t) + \frac{(\tilde{Q}_m+\tilde{\omega}_b C_b T_a)\Delta t}{1+W\beta\Delta t} \end{aligned} \tag{3}$$

where Δt is the time increment; $W = \tilde{\omega}_b C_b / \tilde{C}$, and $Fo = \tilde{k}.\Delta t / \tilde{C}.\Delta x^2$ is the Fourier number; $m = 2, 4, 6$ correspond to the cases of one, two and three dimensions respectively, and in order to avoid numerical instability, the space and time steps are limited by $1 - W(1-\beta)\Delta t - m.Fo \geqslant 0$. Applying the boundary conditions at time $t + \Delta t$ and substituting the calculated results at the previous time t, the unknown T at time $t + \Delta t$ can be solved from the above equation.

The tissue domain is prescribed in a rectangular geometry with $7 \times 7 \times 7$ cm in the x, y and z directions respectively, in which x denotes the tissue depth from the skin surface while y and z are along the surface. The boundary conditions at the probe surface are prescribed respectively according to probe tip and probe shank as: $T = -196$℃ at probe tip; $\partial T / \partial n = 0$ at probe shank. The initial temperature in tissue is simplified as $T0 = 37$℃. In calculations, the grid resolution is $\Delta x = \Delta y = \Delta z = 1$mm and $\Delta t = 0.1$s. $\tilde{Q}_m = 0$ in a highly vascularized tissue like liver and $\tilde{w}_b = 0.005$.

Our routine is described as below:

1. The location of liver, tumor, skin and vessels are determined thanks to a segmentation process performed on the images. In this step, a 3D mesh for each anatomical structure are reconstructed. All vessels are considered as fixed sources of heat at 37℃

2. The shape of needle tip has been designed to fit real cryoprobes

3. Needle tip is placed at an initial position and orientation inside the tumor manually or by the optimization method

4. The simulation procedure imitates a standard cryoablation pattern that consists of two 10 minutes freezing intervals and one 5 minutes thawing step in between, which is congruent with needle manufacturer calibration data in a tissue-like gel, which from now on we call reference data

5. The iceballs are obtained by a 3D reconstruction of the -40℃ isotherm surfaces. The selected value was chosen according to surgeons needs, as this temperature is used as a threshold to determine the resulting necrosis volume

3.2 Optimization of the probes placement in 3D

The optimization process allows to refine the number and placement of the needles (3 translations and 3 rotations for each) to minimize a defect function. It is based on an iterative procedure including the bioheat equation resolution at each step. Every resolution begins with the assumption that the placement of cryoprobes is given with a fixed tip temperature of -196℃ while the initial temperature of tumor and background tissue is 37℃. Then, the bioheat equation can be solved. The resulting temperature field is processed

to evaluate the defect function providing a quantitative estimate of the mismatch between the frozen tissue and the target tissue. Eq.4 shows the definition of the cost function.

More formally, a specific configuration of the cryosurgery design is represented by a state variable U, which is a list of N operating parameters (position of cryoprobes) whose admissible values are contained in $S \subset R^N$. The cost function is the defect weighting function $F : S \to \mathbb{N}$ such that:

$$F(\theta_U) = \int_V \mu(\theta_U(x))dx, \tag{4}$$

where θ_U is the temperature distribution associated to U and

$$\mu(\theta(x)) = \begin{cases} 0 & \text{if } \theta(x) < \tilde{\theta} \text{ and } x \text{ is diseased,} \\ 1 & \text{if } \theta(x) < \tilde{\theta} \text{ and } x \text{ is healthy,} \\ 1 & \text{if } \theta(x) \geq \tilde{\theta} \text{ and } x \text{ is diseased,} \\ 0 & \text{if } \theta(x) \geq \tilde{\theta} \text{ and } x \text{ is healthy,} \end{cases} \tag{5}$$

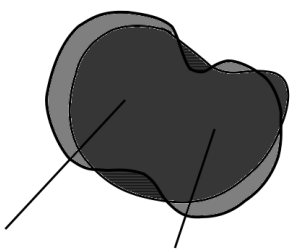

Figure 1: Schematic representation of the defect region. Tumor is in dark grey, and interacting iceballs is in light grey. Not damaged tumor parts are striped and damaged healthy tissue is in very light grey.

A schematic view of this function is demonstrated in Fig.1. Optimization algorithms use this objective function and yield the new positions of cryoprobes in order that the next step can begin. The procedure stops when further correction of the position of cryoprobes becomes negligible or the predefined maximum number of iterations is reached.

Conventional optimization techniques typically require multiple evaluations of the cost function for each iteration. For example, gradient based algorithms would require multiple function evaluations to compute the gradients [7]. Keanini and Rubinsky [1] stated that methods which compute explicit derivatives are likely to be inefficient. Our work employs techniques that avoid calculating derivatives so as to minimize the number of simulations.

As mentioned above our optimization algorithm should be capable of handling a large number of bound constrained optimization variables and be able to minimize an objective function that cannot be expressed analytically in terms of the optimization variables. Keeping these parameters in mind, a bound constrained derivative free optimization method which do not stuck in local minima (global optimization) with low number of iterations would be suitable. Our problem is a convex optimization problem because of cubic search domain surrounding the target region.

Derivative free optimization methods are classified to local and global optimization methods as well as as deterministic, model based and stochastic methods[8]. Six optimization methods were selected based on the parameters just mentioned in order to compare their strengths and weaknesses to our problem.

- Local methods:
  - Deterministic:

    Pattern search: Generating Set Search (GSS) method was selected between different pattern search methods. Each iteration of GSS method consists of two basic steps. The search step is performed first over a finite set of search directions H_K generated by some, possibly heuristic, strategy that aims to improve the current iterate but may not guarantee convergence. If the search step fails to produce a better point, GSS method continues with the poll step, which is associated with a generating set that spans positively R^{n} Generating sets are usually positive bases, with a cardinality between n+1 to 2n [9].

- Global methods:
  - Deterministic:

    Multilevel coordinate search (MCS): It partitions the search space into boxes and in each iteration a label is assigned to each box based on the number of times it has been splitted. MCS selects boxes with the lowest objective value for each level value and marks them as candidates for splitting and will converge when the maximum number of s is reached [10].
  - Model based:

    Surrogate Modelling (SM): Building a model of objective functions in our search domain allows us to optimize a function with less number of iterations. In order to build such a model, one should starts with sampling the search domain and construct an initial surrogate model. Then optimizers are used to converge the model, evaluate the best point and update the surrogate model. For this purpose we have employed a mixture of radial basis functions [11] and kriging [12] interpolations for our surrogate model. Radial basis functions approximate

f by considering an interpolating model based on radial functions and kriging models a deterministic response as the realization of a stochastic process by means of a kriging basis function.

– Stochastic:

Simulated Annealing (SA): At iteration k, simulated annealing generates a new trial point $\hat{x}$ that is compared to the incumbent x^k and accepted with a probability function [13].

$$P(\hat{x}|x_k) = \begin{cases} \exp[\frac{f(\hat{x})-f(x_k)}{T_k}] & \text{if } f(\hat{x}) < f(x_k) \\ 1 & \text{if } f(\hat{x}) < f(x_k) \end{cases} \tag{6}$$

Genetic algorithms (GA): This method introduced by Holland [14] resembles natural selection and reproduction processes governed by rules that assure the survival of the fittest in large populations. Individuals (points) are associated with identity genes that define a fitness measure (objective function value). A set of individuals form a population, which adapts and mutates following probabilistic rules that utilize the fitness function.

Evolution Strategies (ES): This method belongs to the class of Evolutionary Algorithms (EAs) which use mutation, recombination, and selection applied to a population of individuals containing candidate solutions in order to evolve iteratively better and better solutions.

3.3 Experiment design

Our experiments were done on two patient models from the 3D-IRCADb database. They are reconstructed images of liver tumors surrounded by vessels and normal liver tissue. To test different conditions, we chose a case with a small tumor and another with a large one.

For the tests we experimented several parameters, each time changing one parameter while others were fixed. Optimization methods, number of needles and size of the tumors were selected as different experimental designs. Six optimization methods were considered as mentioned in the previous section. In order to compute defect volume, the bioheat equation was solved in each iteration and then objective function value was computed by comparing temperature of each point in the tissue domain.

Comparisons for speed and convergence of the optimization methods are based on the solution profile of each optimizer for few iterations to large ones. We tried to check the sensitivity of each optimizer to other parameters like tumor size and number of electrodes. Tumor size will affect complexity of the problem by extending or shrinking the search domain and number of needles will modify the optimization input variables. In order to have a fair comparison, four different experimental designs are selected, two for small tumor and two

for large ones. In each state there are two possibilities of choosing 3 or 5 needles. All solvers had a maximum of 500 iterations.

The type of croyprobe we modeled was a PERC-24 from Endocare. The theoretical volume of iceball (-40℃ isotherm surface) of this cryoprobe type, given by the manufacturer, is 2.4x2.4x4cm. Ratio between theoretical single iceball volume and tumor volume allows to select the right initial number of needles. We experimented our optimizations on two tumor sizes, small and large. This ratio is 0.7 for small and 0.2 for large tumor, with the chosen cryoprobe type. In order to destroy tumors, it is intuitive to start with a number of needles providing a total iceballs volume at least equal to the tumor volume.

4 Results and discussion

An example of the computation of an iceball produced by 3 needles around the small tumor is shown on Fig.2. Fig.3 shows the trends of defect volume versus iteration number in different conditions: small / large tumors and 3 / 5 needles. Optimization time lapse is directly related to the number of iterations for all optimizers except surrogate modeling. The most time consuming part of optimization process is the solution of bioheat equation which is computed once per iteration. It takes 5 seconds with spatial dimensions mentioned above on a machine using Intel core i7 3.4 to simulate a 10 minutes cryoablation treatment.

Covering the whole tumor with a minimum number of needles demands a lot of iterations for the optimizer to reach a global minimum. Moreover, adding extra needles will increase the number of optimization variables and consequently the risks of increasing healthy tissue region which is damaged, but an optimum number of needles for any size of tumor should be found. This trend is visible in the results shown in Fig.3 top for a small tumor in which the total percentage of defect volume increased by growing the number of needles. Also in Fig.3 bottom, total defect volume for a large tumor decreased by an increase in number

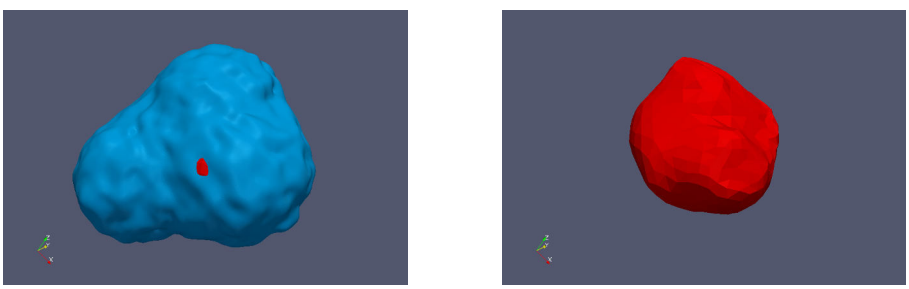

Figure 2: Example of aggregated iceball (left) after a heat propagation simulation for the small tumor (right) and 3 needles. This configuration is not completely optimal as a part of the tumor is outside the iceball.

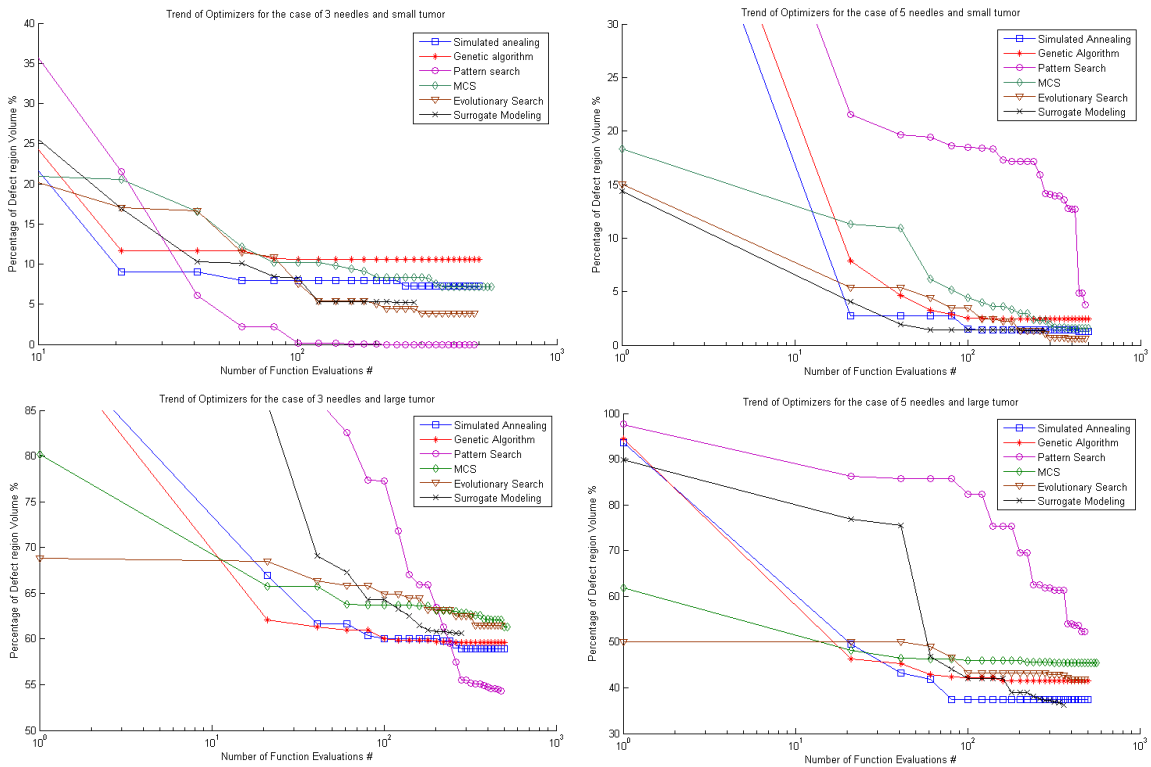

Figure 3: Trend of 6 optimizers for the case of small (top) and large (bottom) tumor are shown above for 3 and 5 needles. Vertical axis shows percentage of defect volume while horizontal axis shows number of iteration for a maximum of 500 iterations

of cryoprobes. Due to the low ratio of iceball volume to tumor volume and large size of the tumor, even with 5 needles we did not find a global minimum within 500 iterations. Increasing number of iterations or number of needles seems to be the first intuitive solutions but due to the computational time for bioheat equation we did not consider them, pursuing our goal to integrate selected methods in our existing planning tool which should converge in the order of minutes for real-time applications.

In speed comparison of each experimental design we are interested to see which method had the minimum of defect volume in its first one hundred iterations. By choosing this criteria and looking into Fig.3 top left graph, GSS local method is prior to others. In this design, thanks to large ratio of iceball volume to tumor volume and less low number of needles, we are facing a simple problem which can be solved easily by a local deterministic solver. Other solvers had more or less the same speed in this scenario. On the right graph, by increasing tumor size both deterministic methods decrease their performance especially

for the GSS method but for other solvers speed of optimization was not affected by changing the search domain. The same characteristic is shown in Fig.3 bottom for large tumor.

For the accuracy comparison we looked for the method which finds the lowest defect volume regardless of number of iterations. In general evolutionary methods had better flexibility than heuristic methods like MCS and GSS. Simulated annealing did rapid convergence among global methods but it is dependent on its initial point therefore the results are not always good with different initial point and tumor shapes. MCS had more or less good results in long iterations regardless of problem complexity due to its global design. SM had the same performance of speed and accuracy comparing to simulated annealing but it was more robust due to changing conditions and tumor shapes. Surrogate modeling also demonstrated better results for complex problems as Fig.3 on the right which is the most complicated among our designs. The strength of this approach lies in the generality of its formulation since SM is independent of the physical interpretation and from the number of the parameters subjected to optimization. In other words, through SM, one is able to set different kinds of free planning parameters without changing the optimization technique.

5 Conclusion and future works

In this study, we compared six derivative free optimization methods. The speed and accuracy of each method was investigated due to number of needles and tumor size. Generating Set Search was selected as fastest for simple problems and Surrogate Modeling as the most robust in complex ones. We have demonstrated our tests by solving bioheat equation inside the optimization process for a 3D cryosurgical planning of two tumor sets of small and large size. Objective function was defined based on the defect volume value and did not consider its shape. We believe that taking into account the shape of objective function will lead to higher precision and lower number of iterations in future works. In order to solve the mentioned convergence problem for large tumors in an acceptable time we are thinking about experimenting smarter routines like supervised methods or multi stage optimization.

Acknowledgments

Authors would like to thank CNRS and Region Alsace for funding this work.

References

[1] Keanini, R., Rubinsky, B.: Optimization of multiprobe cryosurgery. Heat Transfer **114**(4) (1992) 796–801

[2] Baissalov, R., Sandison, G., Reynolds, D., Muldrew, K.: Simultaneous optimization of cryoprobe placement and thermal protocol for cryosurgery. Physics in medicine and biology **46**(7) (2001) 1799

[3] Tanaka, D., Shimada, K., Rabin, Y.: Two-phase computerized planning of cryosurgery using bubble-packing and force-field analogy. Journal of biomechanical engineering **128**(1) (2006) 49

[4] Tanaka, D., Shimada, K., Rossi, M.R., Rabin, Y.: Cryosurgery planning using bubble packing in 3d. Computer methods in biomechanics and biomedical engineering **11**(2) (2008) 113–121

[5] Giorgi, G., Avalle, L., Brignone, M., Piana, M., Caviglia, G.: An optimisation approach to multiprobe cryosurgery planning. Computer Methods in Biomechanics and Biomedical Engineering (ahead-of-print) (2011) 1–11

[6] Pennes, H.H.: Analysis of tissue and arterial blood temperatures in the resting human forearm. Journal of applied physiology **1**(2) (1948) 93–122

[7] Vanderplaats, G.N.: Numerical optimization techniques for engineering design: with applications. Volume 32. McGraw-Hill New York (1984)

[8] Rios, L.M., Sahinidis, N.V.: Derivative-free optimization: A review of algorithms and comparison of software implementations. Journal of Global Optimization (2012) 1–47

[9] Kolda, T.G., Lewis, R.M., Torczon, V.: Optimization by direct search: New perspectives on some classical and modern methods. SIAM review **45**(3) (2003) 385–482

[10] Huyer, W., Neumaier, A.: Global optimization by multilevel coordinate search. Journal of Global Optimization **14**(4) (1999) 331–355

[11] Powell, M.J.: Recent research at Cambridge on radial basis functions. Springer (1999)

[12] Sacks, J., Welch, W.J., Mitchell, T.J., Wynn, H.P.: Design and analysis of computer experiments. Statistical science **4**(4) (1989) 409–423

[13] Powell, M.J.: Uobyqa: unconstrained optimization by quadratic approximation. Mathematical Programming **92**(3) (2002) 555–582

[14] Holland, J.H.: Adaptation in natural and artificial systems: An introductory analysis with applications to biology, control, and artificial intelligence. U Michigan Press (1975)

Résumé

Introduction

Le cancer est une des causes principales de la mort dans la majorité des pays du monde. Parmi les types de cancer prédominants, cancer du foie se situe au quatrième rang due à la prévalence élevée de l'hépatite B. Près de 500,000 personnes sont diagnostiquées chaque année dans le monde. Afin de traiter cancer du foie plusieurs types des interventions chirurgicales sont émergées. Les traitements fondés sur chirurgie mini-invasive ont montré d`avoir des avantages à long terme et temps de repos rapide. Différentes techniques de chirurgie mini-invasive permettent aujourd'hui d'effectuer les procédures d'ablation de tumeurs. Dans le manuscrit présent nous nous concentrons sur l'hyperthermie percutanée, qui est la plus fréquemment choisie par des chirurgiens. Il s'agit de la destruction de la tumeur par la chaleur ou le froid extrême.

La cryochirurgie (également appelée cryoablation ou cryothérapie) est une de ces techniques. Elle a été mise en place au début des années 1960 pour traiter les cancers de la prostate. Elle fonctionne grâce à une technique de décompression très rapide du gaz (généralement de l'argon) à l'extrémité d'une sonde en forme d'aiguille. Lorsque l'argon s'écoule à travers l'aiguille, une boule de cristaux de glace se forme autour du bout de la sonde, ce qui conduit immédiatement à la mort cellulaire des tissus environnants. Selon l'emplacement de la tumeur et la taille de la tumeur, plusieurs aiguilles, éventuellement de types différents, peuvent être utilisées simultanément afin de couvrir la totalité de la tumeur.

La planification pré-opératoire de ce type d'intervention est très difficile pour le chirurgien, qui doit se représenter mentalement la disposition finale des aiguilles par rapport à la position des structures anatomiques environnantes, ainsi que la forme finale du glaçon formé autour des pointes des aiguilles, afin de choisir une stratégie de placement dans un environnement anatomique complexe. Une sur-ablation ou une sous-ablation peuvent entraîner des complications au cours du traitement. De même, un mauvais placement peut également entraîner des complications, notamment des hémorragies. Ainsi, le système de planification d'ablation joue un rôle important dans les procédures d'ablation de la tumeur car il fournit une simulation virtuelle pour guider les chirurgiens.

Une bonne planification inclut une estimation réaliste de la zone d'ablation et une détermination d'emplacement optimal des plusieurs aiguilles afin de couvrir la tumeur complètement en conservant des tissus sains intacte. Dans la plupart des applications de planification existantes les zones d'ablation sont typiquement décrites comme des ellipsoïdes simples non-réalistes autour des cryosondes. Pourtant, en raison de la présence de vaisseaux sanguins dans le voisinage des aiguilles pouvant provoquer un effet de réchauffement, le volume de nécrose peut être déformé, sa taille peut être diminuée, et la tumeur peut n'être que partiellement soumise à une ablation. Pour remédier à ces problèmes, des simulations numériques basées sur l'équation de transfert de chaleur ont été utilisées pour permettre une estimation précise de la zone d'ablation intégrant les effets de dissipation de chaleur des gros vaisseaux sanguins.

Un autre grand défi est l'automatisation du choix de placement tridimensionnel de plusieurs aiguilles simultanément, qui adoptent les contraintes habituelles sur des aiguilles individuelles (par exemple des règles de sécurité comme l'évitement des organes vitaux et les éléments anatomiques, des règles techniques comme la longueur maximale d'aiguille limitant la longueur de la trajectoire, ou encore des règles relatives à la cautérisation), ainsi que des contraintes supplémentaires liées à l'interaction entre les différentes aiguilles (non intersection, interaction des effets).

Ainsi, aucun outil ne permettant à l'heure actuelle d'aborder tous ces points, et devant le besoin crucial d'une telle planification, dans cette thèse nous nous sommes concentrés sur la planification pré-opératoire automatisée de la cryo-chirurgie, avec deux objectifs principaux : 1) assister le chirurgien grâce à une prédiction plus réaliste des zones d'ablation et 2) proposer automatiquement un placement d'aiguille avec un risque minimal pour le patient et une couverture optimale de la tumeur par la boule de glace, dans un délai acceptable pour une utilisation en salle d'opération.

Développement - Plan type

- **Simulation de la boule de glace**

Afin de rapprocher la formation de boule de glace, il est essentiel de calculer propagation de la chaleur à l'intérieur de tissu. Pour atteindre cet objectif une ou plusieurs aiguilles sont situées à l'intérieur de la tumeur et tous les calculs sont effectués dans un grand cube environnant qui centre l'emplacement de la tumeur comme on le voit sur la Figure 1.

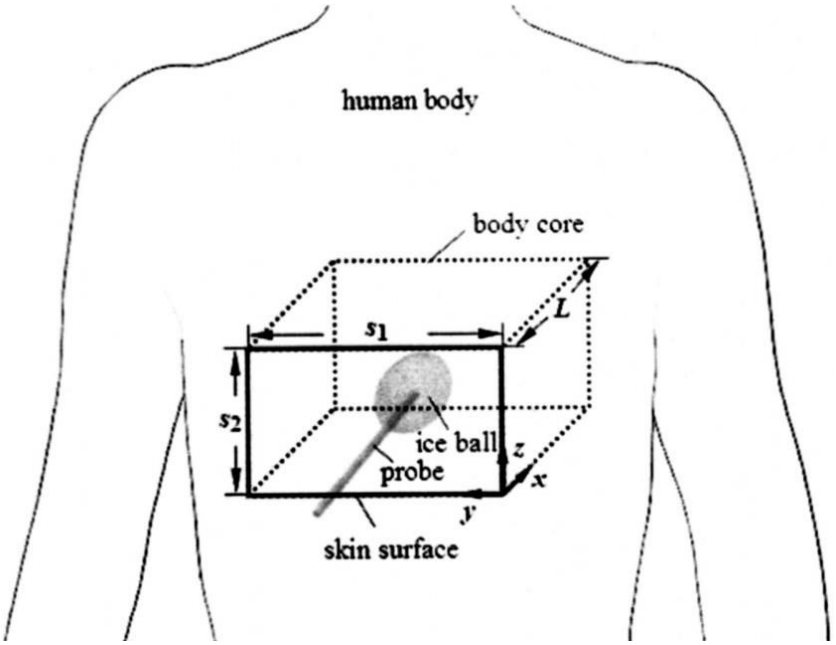

Figure 1: Schématique de la géométrie 3D pour une probe

Afin de modéliser la propagation thermique dans les tissus vivants, l'une des méthodes les plus couramment utilisées, l'équation de transfert de chaleur de Pennes, a été choisie.

$$C_u \frac{\partial T_u(X,t)}{\partial t} = \nabla . k_u \nabla [T_u(X,t)] - \omega_b C_b T_u(X,t) + Q_m + C_b \omega_b T_a \qquad X \in \Omega_u(t) \qquad (1)$$

Les autres modèles incluent ceux qui sont développés par Weinbaum et Nakayama. En mathématiques numériques, le problème de la résolution d'équation de biochaleur peut être défini comme la prédiction de la position évoluant dans le temps de congélation ou de décongélation des fronts où le changement de phase se produit. Ce qu'on appelle communément le problème de Stefan et qui nécessite la résolution de l'équation de conduction de chaleur pour la température dans un domaine qui se compose de parties gelées et non gelées qui se sont séparées par une interface mobile (le front de congélation ou de décongélation).

L'endroit et la forme précises sont critiques et sont déterminés par la température de fusion à laquelle le changement de phase se produit et la condition de Stefan est souvent imposée comme la condition d'équilibre thermique. Dès que les positions du front de gel dépendent de plusieurs facteurs inconnus, un tel problème est généralement fortement non linéaire et la solution précise de ce problème complexe est extrêmement difficile, et parfois il est même impossible de calculer si aucune simplification substantielle pourrait être introduite.

Pour résoudre les problèmes de changement de phase dans les tissus biologiques plusieurs groupes ont proposé des modèles numériques. Afin de garder la généricité de notre outil de planification pour la cryo-chirurgie combinée et l'hyperthermie, la méthode efficace de la capacité thermique est utilisée pour résoudre numériquement le problème de changement de phase avec des frontières mobiles multiples. Bien que cette approche présente plusieurs avantages, il nécessite encore que le maillage soit raffiné à proximité de l'interface. Sur la base de cette solution qui satisfait automatiquement les conditions de changement de phase, une équation unifiée, qui peut être appliquée aux régions de tissus gelées, partiellement gelées et non-gelées est crée. Dans cette équation les tissus sont traités pour le gel ou le dégel avec plusieurs aiguilles sur une gamme de température, et les influences de la perfusion sanguine et de la production de chaleur métabolique ont été prises en compte pour la région non-gelée. Pour la discrétisation nous avons utilisé une méthode de différenciation arrière explicite. Donc, la solution finale de l'équation de propagation de la chaleur de Pennes, après avoir résolu le problème de changement de phase numérique et discrétisation, ressemble à ci-dessous.

$$T(X,t+\Delta t)=\frac{1-W(1-\beta)\Delta t-m.Fo}{1+W\beta\Delta t}T(X,t)+\sum_{i=1}^{m/2}\frac{Fo}{1+W\beta\Delta t}T(X+\Delta X_i,t)+\sum_{i=1}^{m/2}\frac{Fo}{1+W\beta\Delta t}T(X-\Delta X_i,t)+\frac{(\tilde{Q}_m+\tilde{\omega}_b C_b T_a)\Delta t}{1+W\beta\Delta t} \quad (2)$$

Où β est un facteur de relaxation avec $0 \leq \beta \leq 1$ et Δt est l'incrément de temps, Fo $=\widetilde{k}\,.\,\Delta t/\widetilde{C}\,\Delta x^2$ est le nombre de Fourier et W est défini comme W $=\widetilde{\omega}_b C_b/\widetilde{C}$. Enfin, m peut recevoir les valeurs 2, 4 ou 6 correspondant respectivement aux cas de l'une, deux et trois dimensions et ΔX est défini comme ceci:

$$\Delta X_1=(\Delta x,0,0) \quad \Delta X_2=(0,\Delta y,0) \quad \Delta X_3=(0,0,\Delta z)$$

$\widetilde{C}\,(T)$ est la capacité de chaleur efficace; $\tilde{k}(T)$ est la conductivité thermique efficace; $\tilde{Q}_m$ est la production de chaleur métabolique efficace; $\tilde{\omega}_b(T)$ est la perfusion sanguine efficace et elles sont formulées dans les différentes limites de température comme suit:

$$\widetilde{C}(T) = \begin{cases} C_f & T < T_{ml} \\ \frac{Q_l}{(T_{mu}-T_{ml})} + \frac{C_f+C_u}{2} & T_{ml} \le T \le T_{mu} \\ C_u & T > T_{mu} \end{cases} \quad (3)$$

$$\widetilde{k}(T) = \begin{cases} k_f & T < T_{ml} \\ \frac{k_f+k_u}{2} & T_{ml} \le T \le T_{mu} \\ C_u & T > T_{mu} \end{cases} \quad (4)$$

$$\tilde{Q}_m(T) = \begin{cases} 0 & T < T_{ml} \\ 0 & T_{ml} \le T \le T_{mu} \\ Q_u & T > T_{mu} \end{cases} \quad (5)$$

$$\widetilde{\omega}_b(T) = \begin{cases} 0 & T < T_{ml} \\ 0 & T_{ml} \le T \le T_{mu} \\ \omega_b & T > T_{mu} \end{cases} \quad (6)$$

Nous avons utilisé plusieurs méthodes de visualisation, y compris les tranches 2D, les mailles 3D et le rendu volumique pour superposer la zone d'ablation sur les images anatomiques. Afin de valider la méthode d'approximation, la zone d'ablation calculée a été superposée sur sa région segmentée correspondante sur des images post-opératoires, dans des cas d'ablation à une et deux aiguilles. Pour le cas de deux aiguilles comme représente à la Figure 2, la boule de glace simulée est mieux adaptée à la boule de glace segmentée qu'aux ellipsoïdes simplifiés. Afin de montrer l'effet de dissipation de chaleur des vaisseaux sur la déformation des boules de glace, nous avons comparé la zone d'ablation avec les boules de glace ellipsoïdales simplifiées indiquées par les fabricants, dans les situations vasculaires complexes extraites de données réelles (voir la Figure 3).

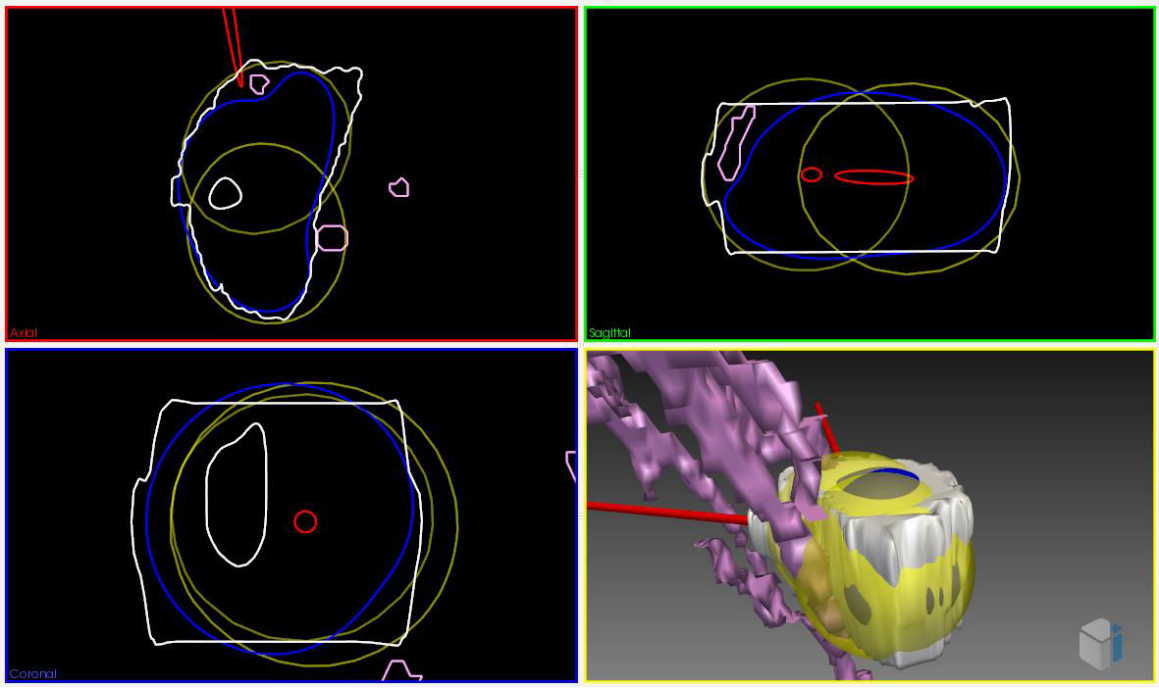

Figure 2 : La boule de glace simulée en bleu contre la boule de glace segmentée en blanche pour dix minutes de congélation. Les ellipsoïdes simplifiés sont en jaune et les vaisseaux en rose.

Distance de Hausdorff, coefficient de Dice et chevauchement de volume booléen ont été utilisés pour la comparaison. La distance de Hausdorff est calculée pour les ellipsoïdes simplifiés et les boules de glace simulées par rapport aux boules de glace segmentées des images post-opératoires et a montré une amélioration de 15%. Entre les opérateurs booléens, l'opérateur de différence de volume démontre mieux l'amélioration réalisée grâce à l'utilisation de la simulation. La différence de volume de boule de glace simulée par rapport à la boule de glace segmentée est six fois inférieure que la différence de volume provenant des ellipsoïdes simplifiés qui correspond mieux aux véritables boules de glace.

Notre contribution pour cette partie comprend l'étude de l'effet dissipateur de chaleur des gros vaisseaux dans le calcul de la zone d'ablation qui n'a encore jamais été pris en compte dans un contexte de planification de cryo-chirurgie dans la littérature. Un cadre interactif a été conçu pour modifier manuellement les positions et les orientations de plusieurs aiguilles et pour visualiser la zone d'ablation calculée, à des fins d'assistance ou de formation chirurgicale. Enfin, de façon à prendre en compte la simulation de différents types de thermo-ablation et de conserver l'aspect générique de l'outil de planification, nous avons utilisé des approches gérant aussi bien les ablations par hypo- (cryoablation) que par hyper-thermie (radiofréquence).

- **Planification de trajectoire multiple**

Le problème de planification automatique d'ablation de tumeur est un problème multi-objectif, qui consiste à trouver le meilleur compromis satisfaisant au mieux les multiples contraintes qui s'appliquent. C'est un problème compliqué, dans lequel la nature multi-objectif du problème est

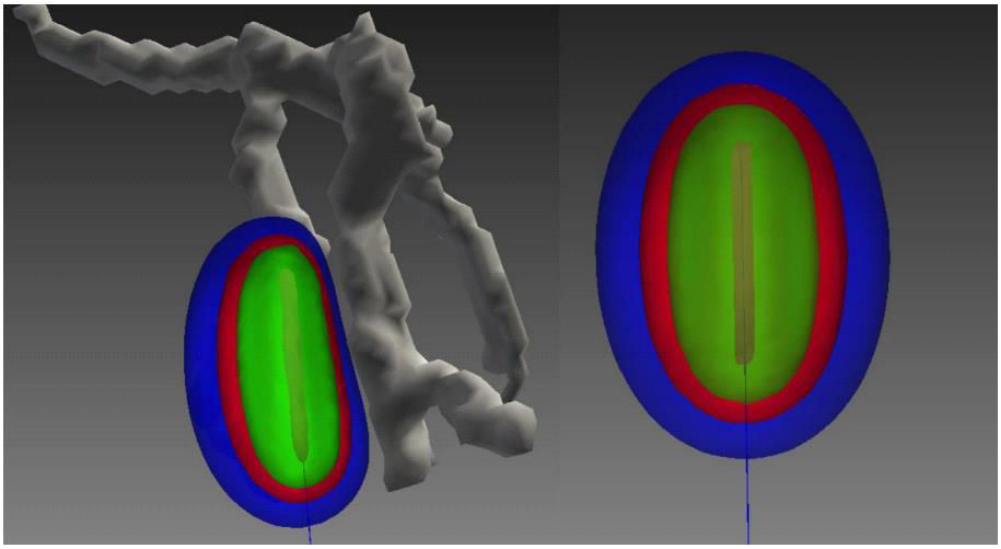

Figure 3 : La boule de glace déformation dû à le vaisseau proximité contre a sans déformation.

difficile à résoudre, mais également chaque contrainte séparément peut être complexe. En particulier, le recouvrement de la totalité de la tumeur par un volume de glace minimal est mathématiquement proche de problèmes classiques de couverture minimale d'un objet avec plusieurs autres formes géométriques, ici des ellipsoïdes (version simplifiée) ou des surfaces isothermes simulées par l'équation de transfert de chaleur depuis les aiguilles. Ce problème de recouvrement peut être classé dans les problèmes polynomiaux non-déterministes en termes de calcul.

Un certain nombre de contraintes a été appliqué à ce problème. Ces contraintes représentent : 1) la création d'une zone délimitant les points d'insertion possible, permettant par exemple d'éviter différents organes tels que les os et la moelle épinière, les gros vaisseaux, ou permettant de ne pas entrer de façon trop tangente par rapport à la surface du foie : ces contraintes sont satisfaites dans une étape de pré-traitement créant une "zone d'insertion", projection sur la peau des trajectoires faisables;

2) la minimisation de valeurs numériques représentant par exemple des règles de non intersection des aiguilles, ou la couverture complète de la tumeur : ces valeurs doivent être calculées à chaque itération d'un processus d'optimisation. Ces contraintes sont fortement non-linéaires, et ont donc été résolues par le développement de fonctions de pénalité appropriées. Equation 7 montre la fonction de pénalisation de solutions qui sont situées à l'extérieur de la zone d'insertion relatives à ses distances. De façon similaire, l'équation 8 est définie pour restreindre le solveur de placer les aiguilles très près l'une de l'autre. Les équations 9, 10 vérifient le volume de la tumeur non couvert et finalement la fonction de pénalité cumulative $h(T)$ est la somme de toutes les fonctions précédentes (l'équation 11).

$$\text{Constraint}_{IZ}(T) = \sum_{i=1}^{N} w_{IZ} * |dist_{IZ}(t_i)| + \text{bias}_{IZ} \quad (7)$$

$$\text{Constraint}_{Cross}(T) = \sum_{i=1}^{N-1} \sum_{j=i+1}^{N} w_{Cross} * max\left(\tilde{d} - dist\left(t_i, t_j\right), 0\right) + \text{bias}_{Cross} \quad (8)$$

$$\text{Constraint}_{coverage} = w_{Coverage} * \int \mu_{tumor}\left(\theta_T(x)\right)dx + \text{bias}_{coverage} \quad (9)$$

$$\mu_{\text{tumor}}\left(\theta_T(x)\right) = \begin{cases} 0 & \text{if } \theta_T(x) \le \tilde{\theta} \text{ et x est dans la tumeur} \\ 1 & \text{if } \theta_T(x) > \tilde{\theta} \text{ et x est dans la tumeur} \end{cases} \quad (10)$$

$$h(T) = \text{Constraint}_{IZ}(T) + \text{Constraint}_{Cross}(T) + \text{Constraint}_{Coverage}(T) \quad (11)$$

où w_* et $bias_*$ sont la pondération et valeur du biais pour chaque contrainte. Elles peuvent être contrôlées par l'opérateur sur la base de l'importance de cette contrainte. $\theta_T(x)$ est le champ de température de chaque voxel dans l'espace de et $\tilde{\theta}$ est le seuil de température de la mort cellulaire.

Plusieurs fonctions objectif ont été introduites dans notre outil de planification afin de minimiser le volume de nécrose des tissus sains et de maximiser la distance des trajectoires multiples des aiguilles aux vaisseaux et aux organes vitaux. Les équations 12 et 13 calculent le volume de nécrose des tissus sains où $\theta_T(x)$ est l'indice de température au point x et $\tilde{\theta}$ est le seuil de température de la mort cellulaire. Puis la distance des trajectoires multiples des aiguilles aux vaisseaux et aux organes vitaux est présentée dans les équations 14 et 15. Pour transformer cette fonction multi-objectif en une unique fonction mono-objectif à minimiser, une somme pondérée est utilisée et formulée par l'équation 16. Chaque fonction objectif est normalisée à l'avance à une valeur comprise entre 0 et 1. En définitive, la somme des fonctions objectives ensemble et des fonctions de pénalité sont utilisées pour minimisation comme on le montre dans l'équation 17.

$$f_{volume} = \int_V \mu_{\text{healthy}}\left(\theta_T(x)\right) dx \quad (12)$$

$$\mu_{\text{healthy}}\big(\theta_T(x)\big) = \begin{cases} 1 & \text{if } \theta_T(x) \le \tilde{\theta} \text{ et } x \text{ est dans les tissus sains} \\ 0 & \text{if } \theta_T(x) > \tilde{\theta} \text{ et } x \text{ est dans les tissus sains} \end{cases} \quad (13)$$

$$f_{\text{risk\_vessel}}(T) = \max\left(\frac{5 - \min_{i=1:N} dist_{\text{vessels}}(t_i)}{5}, 0\right) \quad (14)$$

$$f_{\text{risk\_ribs}}(T) = \max\left(\frac{5 - \min_{i=1:N} dist_{\text{ribs}}(t_i)}{5}, 0\right) \quad (15)$$

$$f(T) = w_{\text{volume}} * f_{volume} + w_{\text{risk\_vessel}} * f_{\text{risk\_vessels}}(T) + w_{\text{risk\_ribs}} * f_{\text{risk\_ribs}}(T) \quad (16)$$

$$\min_{T \in R^{5*N}} f(T) + h(T) \quad (17)$$

Puisque ce problème d'optimisation est extrêmement non linéaire et il est impossible de calculer son dérivative direct, différentes méthodes d'optimisation sans dérivée ont été utilisées: déterministes ou stochastiques, heuristiques ou basées modèle et locale ou global. Ces méthodes avec ses propriétés sont présentées dans Table 1. La vitesse, la précision et la robustesse de certains de ces procédés ont été comparés dans un domaine de recherche avec les différentes complexités. Six cas ont été choisis avec différents tailles de tumeurs et complexité de la zone d'insertion. Les expériences sont répétés pour plusieurs nombres et types des aiguilles fondé sur taille de tumeur. Elles sont également répétées 5 fois pour les méthodes stochastiques et ensuite la valeur moyenne est utilisée. La première étude est effectuée pour tester la possibilité de couverture de la tumeur au minimum nombre des aiguilles sans tenir compte d'autres contraintes.

Dans cette première étude, toutes les méthodes stochastiques sont capables de couvrir la tumeur cependant la modélisation porteuse et modèle de recherche étaient plus rapides. Dans la deuxième étude y compris toutes les contraintes, modèle de recherche, solis wets et d'algorithme évolutionnaire sont capables de couvrir dans le cas de la zone d'insertion simple. Pour une zone d'insertion complexe et discontinue, seulement la modèle de recherche est capable de converger vers une bonne précision en évitant toutes les contraintes.

À toutes les expériences précédemment, le solveur comporte plus de mille itérations pour obtenir un minimum. Puisque le placement des aiguilles est modifié à chaque itération d'optimisation, l'équation de propagation de la chaleur devrait être calculée séparément. Cette procédure est longue durée et elle a besoin de plusieurs heures des calculs. Pour résoudre ce problème, la planification est effectuée en deux phases. Dans la première phase l'ellipsoïde simplifié est utilisé à sa place de la boule de glace simulée pour une planification rapide. Dans un deuxième temps, la position et de l'orientation des aiguilles sont légèrement modifié dans une nouvelle phase d'optimalisation. Cette fois la boule de glace simulée est utilisée à chaque itération d'optimisation. Le résultat de cette perspective est illustré dans Figure 4 démontrant la boule de glace simulée, l'ellipsoïde simplifié, les aiguilles et les autres organes. L'effet de vaisseau dans la déformation d'une boule de glace est visible la zone zoomée à proximité d'un vaisseau.

La Figure 5 illustre la tendance de l'optimisation pour planification automatique pour la cryo-chirurgie y compris toutes les contraintes pour une phase et deux phases méthodes. Chaque itération prend 50 secondes sur une machine avec cœur i7-3.4 de bien calculer les simulations. Dans l'une phase

planification, il a besoin de 700 itérations pour converger a la minimum ou 9 heures et 43 minutes. Planification avec l'ellipsoïde simplifié prend quelques secondes pour les calculs et ce temps est négligeable en comparaison avec la simulation de transfert de chaleur. Donc pour l'optimisation deux phases en Figure 5, la tendance de deuxième phase est seulement illustrée. Dans cette figure, la tendance de plusieurs optimiseurs a été comparée et les solveurs comme la modèle de recherche, la modélisation porteuse et l'algorithme évolutionnaire sont supérieurs aux autres. Cette fois l'algorithme a besoin de 30 itérations à trouver le minimum et la planification a été terminée en 25 minutes qui est faible à faire en salle d'opération.

À des fins de validation, des expérimentations ont été menées en définissant une configuration a priori de la zone d'ablation et les résultats ont été comparés avec les résultats obtenus en utilisant une méthode de recherche exhaustive. En outre, ils sont comparés aux images post-opératoires des patients pour le cas d'un et de deux aiguilles.

Table 1 : Classification des méthodes choisis fondé sur ses propriétés

Methode	✓	locale	déterministe	sans contraintes	direct	différentiable
	×	global	stochastique	sous contraintes	basées modèle	sans dérivée
Simplexe		✓	✓	×	✓	×
Recherche direct		✓	✓	×	✓	×
Modèle de recherche		✓	×	×	✓	×
Solis wets		✓	×	×	✓	×
Algorithme évolutionnaire		×	×	×	✓	×
Modélisation porteuse		✓	×	×	×	×

Notre contribution dans cette partie comprend l'élaboration d'un outil de planification automatique pour la cryo-chirurgie, pour l'optimisation 3D de plusieurs aiguilles à tous degrés de liberté tout en évitant les organes obstructifs et vitaux, un outil générique qui accepte des nouvelles contraintes chirurgicales et anatomiques basées sur l'organe opéré, en tenant compte de l'intégration des mesures de simulation et de planification, et un approche d'optimisation en deux phases pour combiner ellipsoïdes simplifiés et la simulation de transfert de chaleur afin d'obtenir les résultats rapides.

Conclusion et perspectives

Dans cette thèse, un outil de planification pour la cryo-chirurgie avec aiguilles multiples a été élaboré en tenant compte de l'intégration de simulations de transfert de chaleur dans le processus d'optimisation. Les contraintes non-linéaires ont été résolues en utilisant une étape unique de pré-traitement et en introduisant plusieurs fonctions de pénalité. Un processus d'optimisation en deux phases a été utilisé, qui permet d'obtenir un résultat plus précis en un temps de calcul acceptable et applicable en salle d'opération. L'étude de l'influence des vaisseaux a démontré le rôle important des vaisseaux dans formation de la boule de glace, souvent surestimée par les méthodes habituelles, et donc dans les risques de récidive de la tumeur.

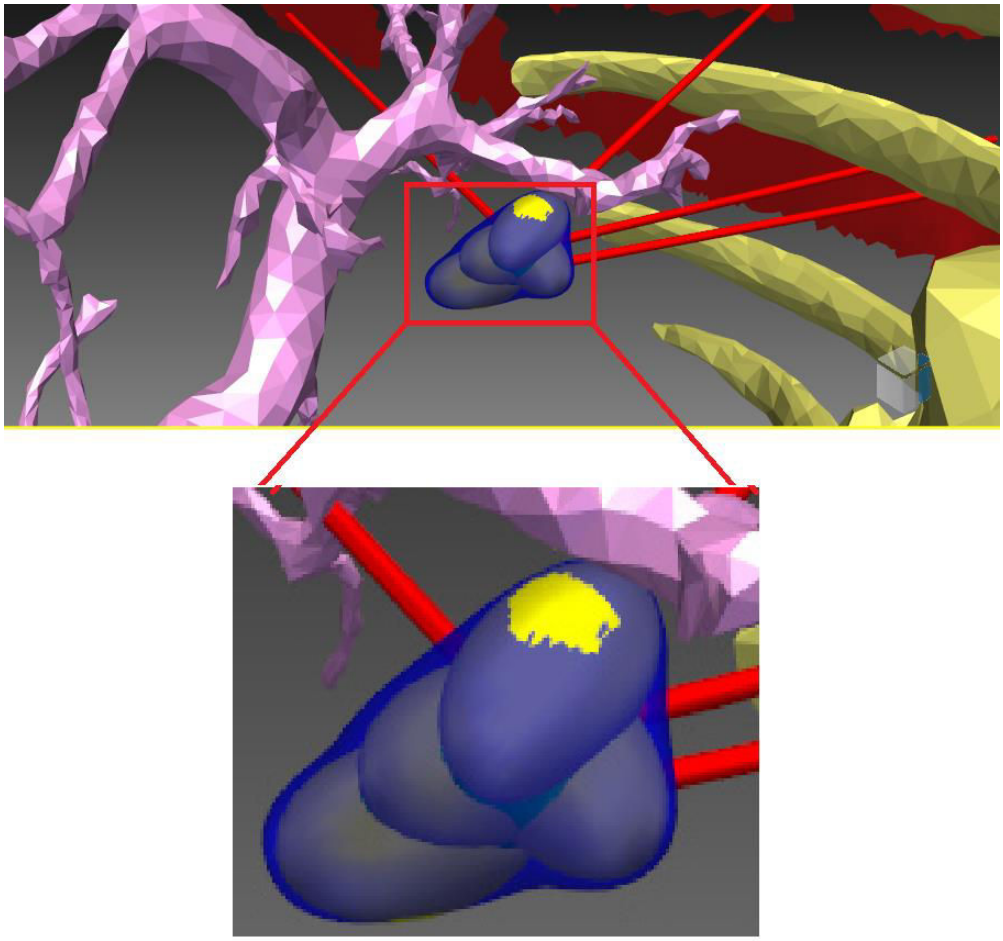

Figure 4 : Le résultat de planification. Les ellipsoïdes sont en jaune, la boule de glace simulée en bleu.

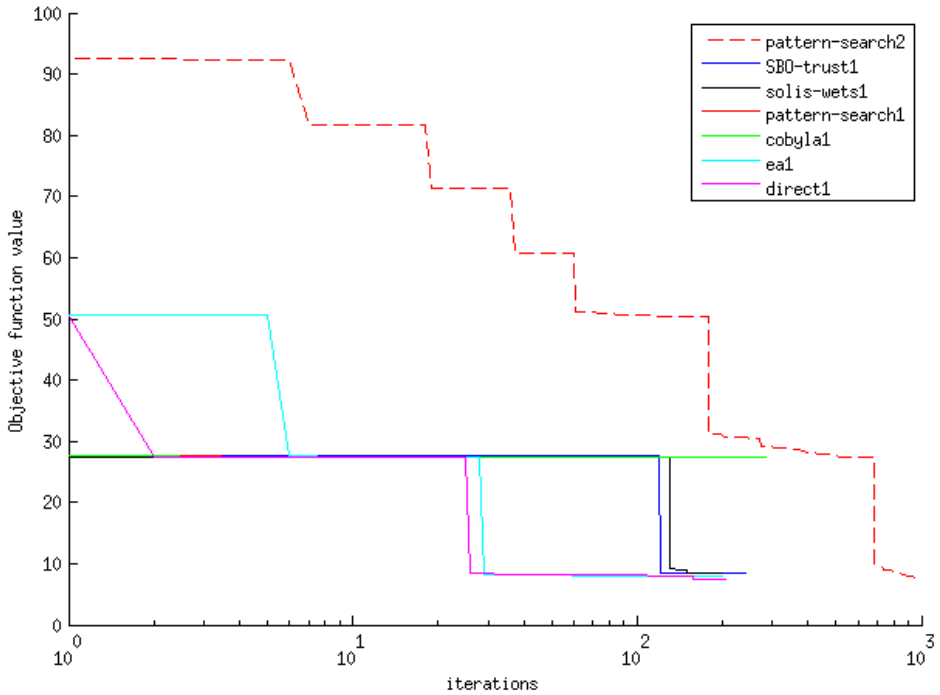

Figure 5 : Une comparaison d'optimisation monophasé par la ligne tiretée et plusieurs méthodes d'optimisation deux phases par les lignes solides.

Dans de futur travaux, l’utilisation d’algorithmes de traitement parallèle pourra être proposée pour le calcul rapide et plus fin de l'équation de transfert de chaleur, en gardant la solution numérique plus stable pour les paramètres d'entrée. L’introduction de modèles d’aiguilles déformables dans notre outil de planification pourrait également augmenter l’éventail d'applications et produire des résultats plus réalistes.